UNIVERSITY OF OKLAHOMA

GRADUATE COLLEGE

RECONFIGURABLE FILTER DESIGN USING LIQUID METAL ACTUATION

A THESIS

SUBMITTED TO THE GRADUATE FACULTY

in partial fulfillment of the requirements for the

Degree of

MASTER OF SCIENCE

By

ALEX PHAM
Norman, Oklahoma
2021

RECONFIGURABLE FILTER DESIGN USING LIQUID METAL ACTUATION

A THESIS APPROVED FOR THE
SCHOOL OF ELECTRICAL AND COMPUTER ENGINEERING

BY THE COMMITTEE CONSISTING OF

Dr. Hjalti Sigmarsson, Chair

Dr. Jessica Ruyle

Dr. Jay McDaniel

Acknowledgments

I would like to deeply thank my advisor and chair, Dr. Hjalti Sigmarsson, for his incredible mentorship throughout my undergraduate and graduate studies. His support, encouragement, insights, constructive criticism, and many thought-provoking or amusing conversations have helped me grow both personally and professionally. I would not be the engineer I am today without his inspiring passion for research and the opportunity he gave me in the middle of my undergraduate career with this liquid metal filter project. I am also indebted to Shahrokh Saeedi for his endless support, intellectual enthusiasm, and readiness to enlighten me on any topic. His attention to detail and thorough explanations of all the fabrication processes at the Advanced Radar Research Center (ARRC) were what allowed me to adapt and develop techniques to realize all the designs throughout this work. The extraordinary guidance from both drove me to achieve incredible results in only my first year of research and to present my first conference paper at the 2019 International Microwave Symposium. I cannot thank both enough for the opportunities, knowledge, skills, and experience that I have gained under them, which I will continue to develop throughout the rest of my engineering career.

During my time at the ARRC, I met many incredible colleagues who have helped with my research and studies and many of whom I have developed long-lasting friendships. I want to thank Russell Kenney, Kurt Konyalioglu, Paul Hartline, Chris Walker, Adrian Bauer, Grant Karber, Cal Schone, Marc Thibodeau, Eivy

Arroy Diaz, Stephen Bass, Gokhan Ariturk, Kyle Kanaly, and many others at the ARRC that I have had the pleasure of working with, teaching, and learning from. All the people I have met are intellectually curious, thoughtful, and incredible engineers that have made an unforgettable impact on my life. I wish all of them the best of luck in their future careers and academic studies.

I want to thank both my parents, David and Kristen Pham, and my brother, Andrew Pham. Their support and love throughout the many years have helped me develop into the kind and curious person that I am today.

I would also like to thank several close friends that have encouraged and supported me throughout the COVID-19 pandemic. I am thankful to Fiona Hu for her advice and help on the development of the interfacing and mounting structure for the fully reconfigurable filter design. She as well as my many other friends in the Somni House community have listened to me talk for hours about my research, RF engineering, science, the universe, and many other intellectual, frivolous, or personal topics. Their endless encouragement and support throughout such a difficult time was what gave me the drive and motivation to complete my thesis. Lastly, I want to thank my best friend, Erica Luong, for always being there to celebrate my achievements and reassure me throughout all the hard times. Her constant friendship and compassion have been invaluable throughout my studies, and my gratitude for her is more than can be expressed in words.

Table of Contents

List of Figures

List of Tables

Abstract

The emergence of technologies such as 5G, IoT, automotive radar, wireless power transfer, broadband satellite internet, and more has increased the number of devices operating and transmitting in the radio frequency (RF) spectrum. Future systems will need to more efficiently use the spectrum without interference, which requires highly reconfigurable filter designs capable of frequency, bandwidth, and shape control. Research has explored filter tuning mechanisms such as tuning screws, piezoelectric actuators, microelectromechanical systems (MEMS), varactors, and PIN diodes. Liquid metal has been a recent growing area of research because of its potential for higher power, linearity, repeatability, and flexibility.

This work presents and validates a novel continuously tunable liquid metal mechanism. A tunable substrate-integrated-waveguide resonator with a 3.8 GHz to 5.9 GHz tuning range is presented. The resonator is then used as the building block for a frequency-tunable second-order filter with measured tuning of 3.4 GHz to 5.7 GHz. This is finally developed into a fully reconfigurable second-order design with wide bandwidth, center frequency, and response shape tuning. It can realize a Butterworth response from 3.8 GHz to 5.6 GHz with either a constant absolute bandwidth from 100 MHz to 200 MHz or a constant fractional bandwidth from 2% to 7% over the entire frequency range. All designs show promising results and demonstrate the capabilities of this liquid metal tuning mechanism for future applications requiring advanced reconfigurability.

Chapter 1

Introduction and Background

1.1 Motivation

There is a fast growing reliance on wireless data, power transfer, and sensing with the emergence of technologies such as 5G, IoT, autonomous vehicles, advanced biomedical sensing, wireless charging, and more. All these technologies rely on efficient transmission and reception of electromagnetic radiation in the microwave frequency spectrum ($1\,\mathrm{GHz}$ to $1\,\mathrm{THz}$). With more devices and technologies needing access to the spectrum, it becomes an increasing problem to maintain effective use of the spectrum without interference between different technologies and devices. There has been growing interest in the field of mm-wave ($24\,\mathrm{GHz}$ to $100\,\mathrm{GHz}$) and terahertz frequency technologies ($100\,\mathrm{GHz}$ to $10\,\mathrm{THz}$) to open up new parts of the spectrum that were not easily accessible in the past due to technological limitations of generating such high frequencies [1, 2]. This new part of the spectrum opens up possibilities for many future applications to move into this range.

This expansion of available spectrum does not entirely solve the issue of spectral crowding since higher frequency microwave signals suffer from disadvantages such as short range, power inefficiencies, susceptibility to obstructions and weather,

manufacturing complexity, and cost. As a result, not all applications are well suited for these higher mm-wave and terahertz frequencies. The most desirable frequency band that avoids those listed disadvantages lies within the range of 2 GHz to 4 GHz, referred to as S-band, and the smaller ISM band of 2.4 GHz to 2.5 GHz is where the majority of consumer wireless devices operate such as Wi-Fi and Bluetooth. The spectrum allocation of just 2 GHz to 3 GHz shown in Fig. 1.1 reveals how crowded this part of the spectrum has become. The crowding becomes even more apparent when viewing how closely spaced the operating channel band allocations of Wi-Fi and Bluetooth within the ISM band in Fig. 1.2. This makes it important to more effectively maintain this part of the spectrum to minimize interference and unnecessary spectral clutter. With the exponential growth of devices, the same spectral crowding issues will also eventually occur in mm-wave and terahertz devices unless an effective solution such as dynamic spectrum access is developed.

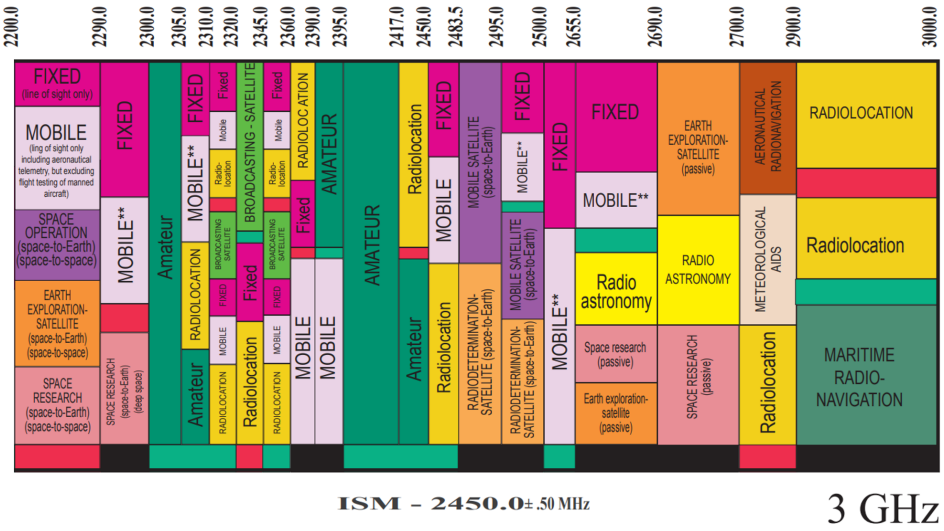

Figure 1.1: United States spectrum allocation of the 2 GHz to 3 GHz band illustrating the close overlap of bands. The labeled ISM band of just 2.4 GHz to 2.5 GHz is where most consumer Wi-Fi and Bluetooth devices operate. Adapted from [3].

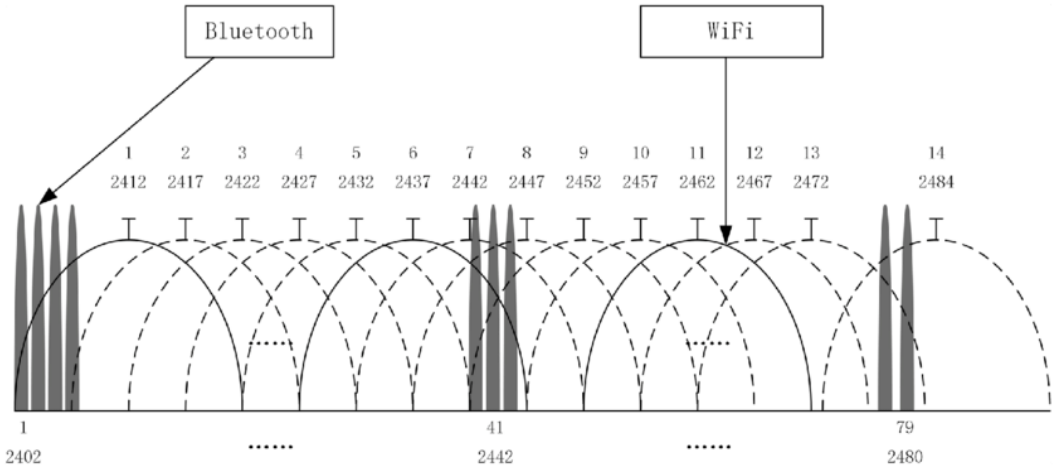

Figure 1.2: Wi-Fi frequency allocated channel bands which lie within the ISM band of 2.400 GHz to 2.5000 GHz (from [4]).

In order for each device to operate in its designated frequency band, every wireless device relies on components called filters. Filters are electric circuits that have frequency-dependent characteristics that allow a certain band of frequencies to pass through while rejecting other parts of the frequency band from affecting the system. The majority of modern systems rely on static filters, low tunability filters, or filter banks (a device that can switch between multiple fixed filters) in order to properly remain in its spectral limits. This allows for devices to not interfere with each other, but the more stringent the spectral limit demands of the filter are the greater the size, complexity, and loss of the device.

Dynamic spectrum access is a paradigm for future microwave systems to intelligently change their operating band and rejection of interference sources depending on the surrounding spectral needs. As interference sources emerge or disappear, such systems will adapt by shifting to less crowded frequencies or applying rejection filtering at interference frequencies. Frequency-agile devices capable of advanced reconfigurability are necessary and has led to growing research into the field of highly tunable and reconfigurable filter designs [5–10].

1.2 Microwave Filters

Microwave filters are characterized by their S-parameter response which describes the relation between the voltage wave at one port of the device given an excitation at the same or different port. The transmission response of a filter is the measure of how much power passes through the device and is denoted as S_{21} or S_{12}. The reflection response of a filter is the measure of how much power gets reflected back to the same exciting port of the filter and is denoted as S_{11} for the power reflected back to port 1 or S_{22} for the power reflected back to port 2. When designing a filter, the typical transmission and reflection response will resemble that shown in Fig. 1.3 which depicts a 5th-order Chebyshev filter response designed for $10\,\mathrm{dB}$ of return loss ripple with resonators with a quality factor of 300.

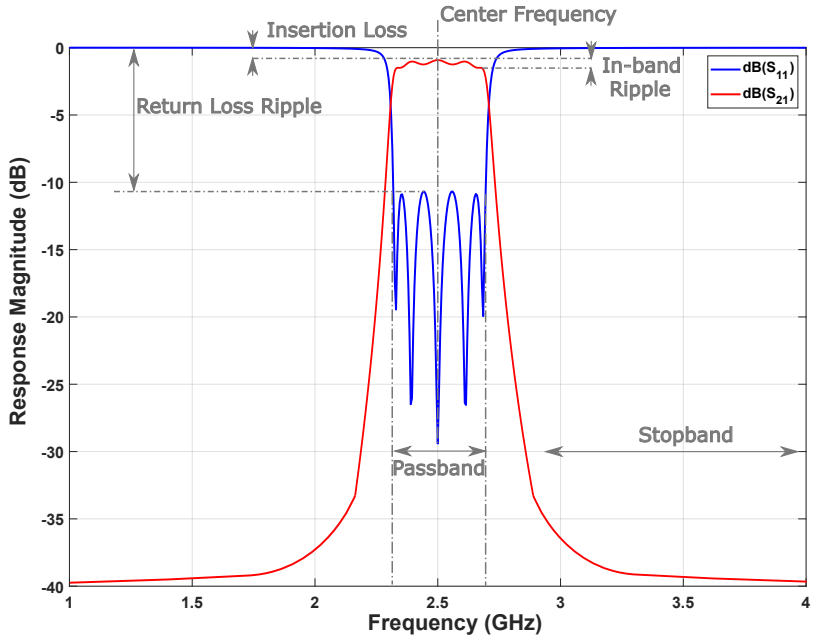

Figure 1.3: Typical bandpass filter response with labeled design performance parameters that are considered. The response is a 5th-order Chebyshev response designed for $10\,\mathrm{dB}$ of return loss ripple with resonators with $Q = 300$. The red trace is the transmission response (S_{21}) and the blue trace is the reflection response (S_{11}).

The passband is the band of frequencies over which the majority of the signal power is allowed to pass through the filter while the stopband is the frequency band over which the signal power is strongly attenuated. The insertion loss of a filter is the measure of how much power is lost in the device within the passband which should be minimized for maximum system sensitivity. This loss is influenced by the quality factor of the resonators, which is ideally would be infinite but is limited by the resonator technology and materials. The steepness of transition between the passband and the stopband is dependent on the number of resonators (or filter order) and other mechanisms such as cross coupling and higher-order resonances. The more stringent the demands of rejection roll-off, high stopband attenuation, low passband insertion loss, and minimal in-band ripple, then the more difficult the filter will be to design and implement.

Complicating the design further, there are considerations such as manufacturability, size, weight, cost, maximum power-handling, temperature sensitivity, shock or vibrational sensitivity, reliability, and phase performance. Filter design and choice is then heavily application and specification dependent, and various filter technologies to meet different trade-offs have been developed, which are illustrated in Fig. 1.4.

At microwave frequencies, lumped element filter designs, like those in low frequency electrical systems such as power or audio filters, become difficult to realize. This is due to the fact that at higher frequencies the parasitic effects of capacitors and inductors begin to dominate and cause the components to deviate from their desired component value. Even when lumped element designs can be realized, they suffer significantly in performance compared to what are called distributed element designs. Since higher frequency electromagnetic waves have shorter wavelengths that are close to the relative size of components and circuit board traces, different

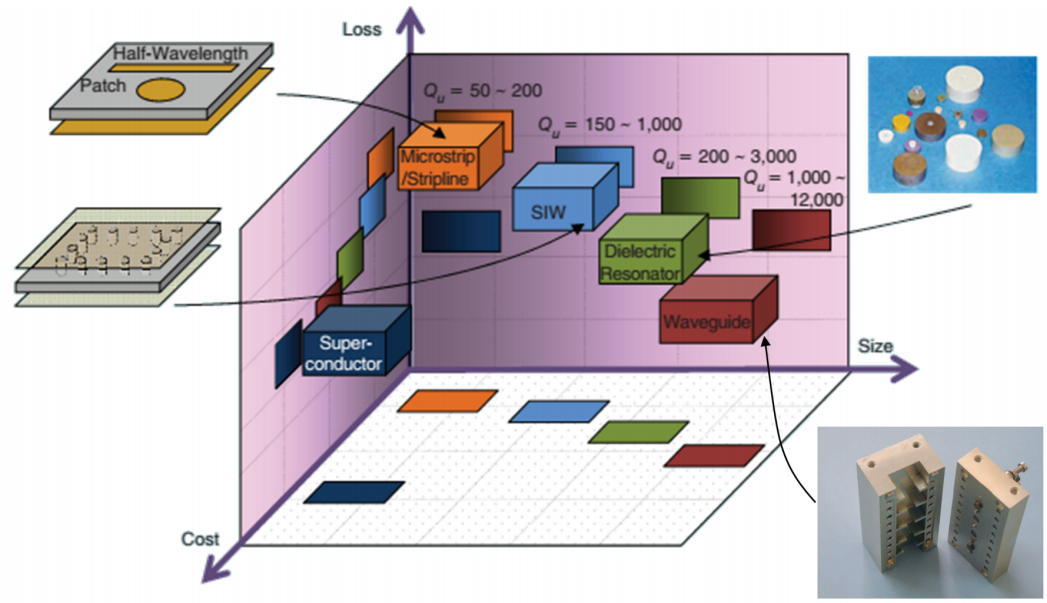

Figure 1.4: Comparison of various microwave filter technologies in terms of loss, cost, size, and quality factor (from [11]).

geometric structures can be designed that allow for these waves to reflect or resonate in desirable ways. These structures act as a distributed inductor and capacitor network rather than the typical lumped element designs and include technologies such as microstrip, stripline, substrate integrated waveguides, dielectric resonators, waveguides, and superconductors.

Microstrip filters are a relatively inexpensive and compact distributed filter technology that consists of conductive trace designs on the top of a printed circuit board (PCB). Microstrip filters have the disadvantages though of being radiative and highly lossy, but are low cost, small form factor, and are easily manufacturable with planar printed circuit board technology (top left of Fig. 1.4). These are ideal for applications that do not require high selectivity and filter performance such as many small consumer electronics.

At the opposite end are waveguide filters, which are large metallic blocks that have cavities and cutouts precision machined into them, and dielectric resonators,

which are pieces of usually ceramic or another nonconductive material that has precise electrical properties at microwave frequencies (bottom right and top right of Fig. 1.4 respectively). The two are large and more expensive to manufacture but are necessary for applications requiring high selectivity and sensitivity in systems such as cellphone tower base stations, advanced radars, space imaging systems, and satellites due to their low loss, high power-handling, and non-radiation.

A trade-off between loss and cost are substrate integrated waveguides (SIW), which are created by integrating cavities, similar to the large machined metallic waveguides, inside a PCB material with many conductive vias outlining the outer walls of the shape (depicted on left of Fig. 1.4). Since PCB technology and plated via technology are well-developed manufacturing technologies used for many other electronics applications, they are cost-effective and mass-manufacturable while performing better than microstrip filters.

This makes SIW filters a desirable option for the implementation of low loss highly reconfigurable filter designs. Research has been done on the integration of various tuning mechanisms such as tuning screws [12], piezoelectric actuators [6, 7, 9], microelectromechanical systems (MEMS) [13], varactors [6, 14, 15], and PIN diodes [16] into SIW filter technology. Each of these different mechanisms have trade-offs in tunability, repeatability, reliability, flexibility, or power-handling. A promising new mechanism in tunable microwave designs are nontoxic room-temperature liquid metals such as Galinstan (GaInSn) and eutectic gallium indium (EGaIn).

1.3 Room Temperature Liquid Metals

Gallium-based liquid metals such as Galinstan and eutectic gallium indium have grown in interest for tunable microwave component applications. Liquid metals have been used in the design of filters [17–23], switches [24–26], antennas [27–32], a phase shifter [33], and impedance tuners [34, 35].

One reason is the high power-handling capabilities of liquid metals over varactors and PIN diode mechanisms, which have semiconductors that will breakdown under high-voltage conditions. A coplanar waveguide filter tuned by Galinstan capacitive loading channels and found that it was capable of $\sim 20\,\mathrm{W}$ short-duration excitations and $10\,\mathrm{W}$ high-average-power excitations was tested in [23]. Thermal images of the liquid metal filter at different input power levels can be seen in Fig. 1.5. The limiting factor of the power was observed to be physical deformation due to heating of the Galinstan, which can be resolved through better heat-sink design. A reconfigurable liquid metal monopole design capable of handling higher power (31 dBm) before failure than the same design using active varactor tuning (24 dBm) was demonstrated in [31]. In the same paper, a two-tone distortion test, in which two fundamental tones close in frequency result in third-order intermodulation tones, found that the liquid metal tuned monopole had $40\,\mathrm{dB}$ higher linearity than the varactor monopole.

Liquid metal has also found application in flexible and stretchable designs [32, 36, 37] which have promising applications in medical and wearable consumer technologies. In [37], a microstrip design that can maintain performance even during heavy stretching, bending, and twisting (shown in Fig. 1.6) was presented. A stretchable liquid metal antenna design that was still able to maintain its performance after 100 stretch iterations was tested in [32]. This is due to the self-healing

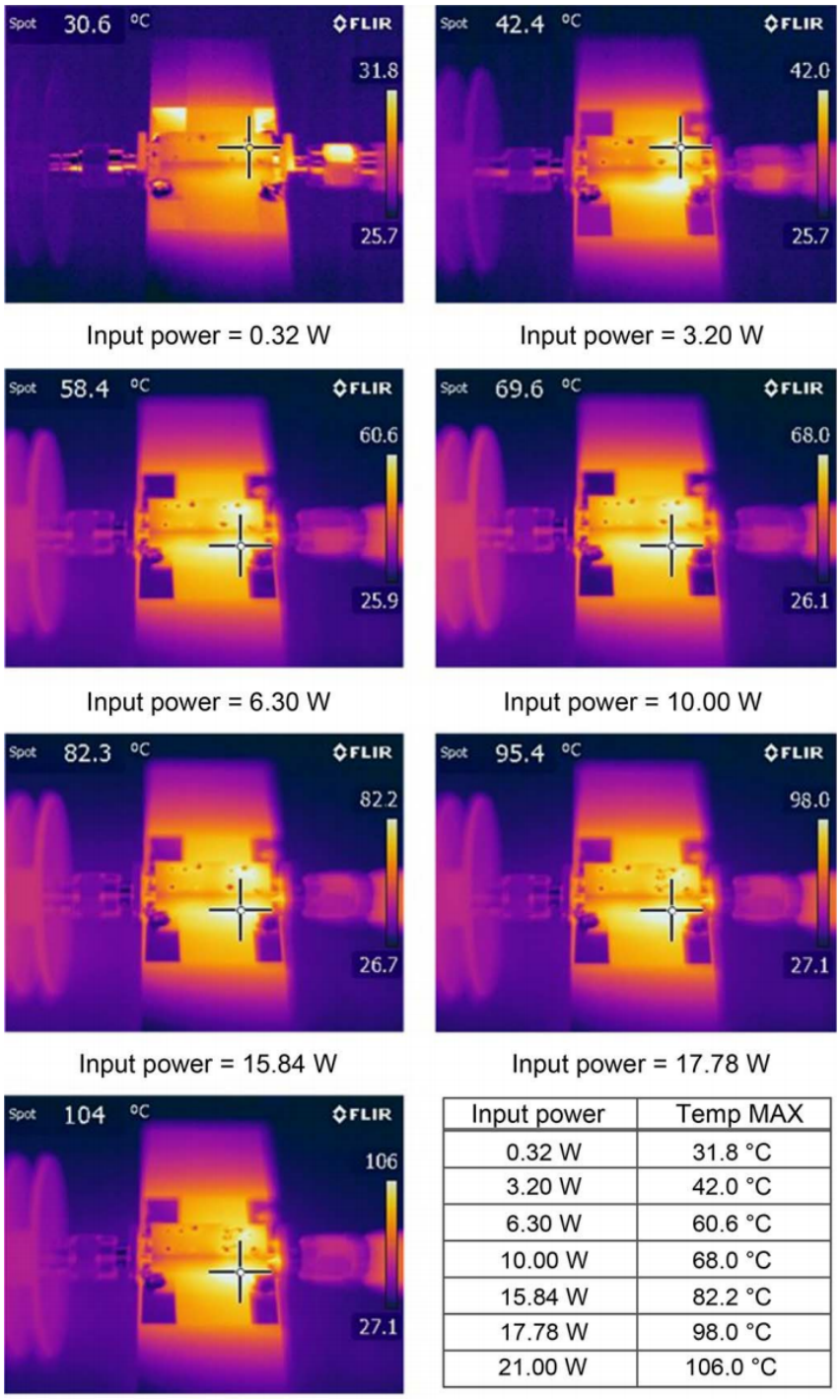

Input power	Temp MAX
0.32 W	31.8 °C
3.20 W	42.0 °C
6.30 W	60.6 °C
10.00 W	68.0 °C
15.84 W	82.2 °C
17.78 W	98.0 °C
21.00 W	106.0 °C

Figure 1.5: Thermal images of a coplanar waveguide filter using liquid metal capacitive tuning channels at different input powers from [23].

properties of liquid metals and the reversibility and repeatability of electrical connections without the stress or wear from solid mechanical connections. This is especially desirable for switches since typical mechanical switches wear down over time and eventually no longer can create strong enough connections. In [24], a unique design of microfluidic Laplace barriers that utilizes the high surface tension of gallium liquid metals so that the liquid metal switch can only be closed when pressure is applied onto both sides (shown in Fig. 1.7) was demonstrated. When this pressure is removed, the surface tension of the liquid metal will cause the connection to cleave and separate the two parts of the switches.

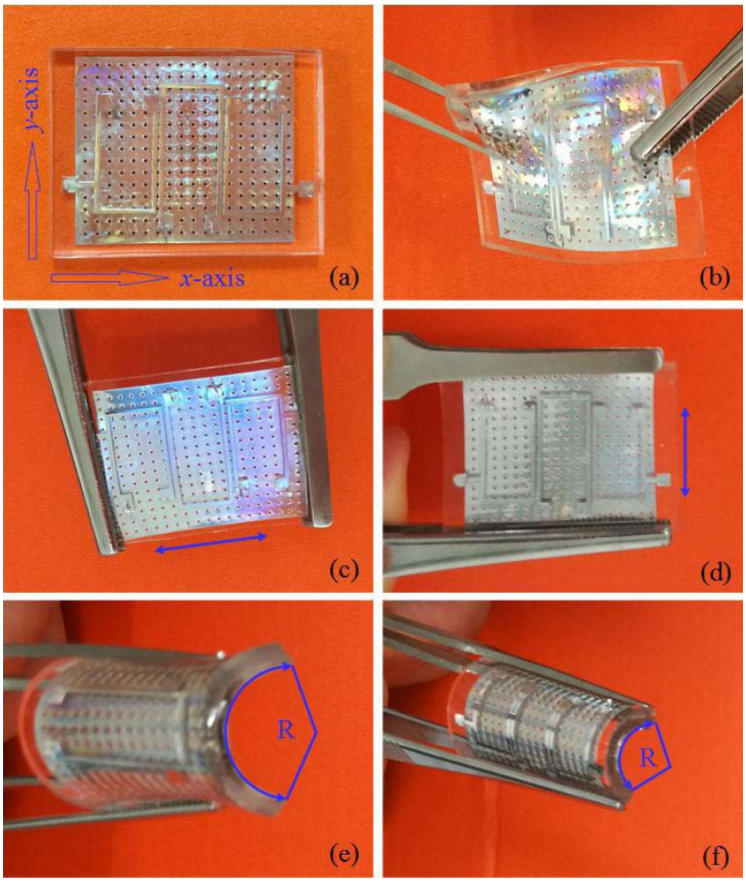

Figure 1.6: Liquid metal microstrip filter design capable of maintaining performance at different stretching, bending, and twisting states from [37].

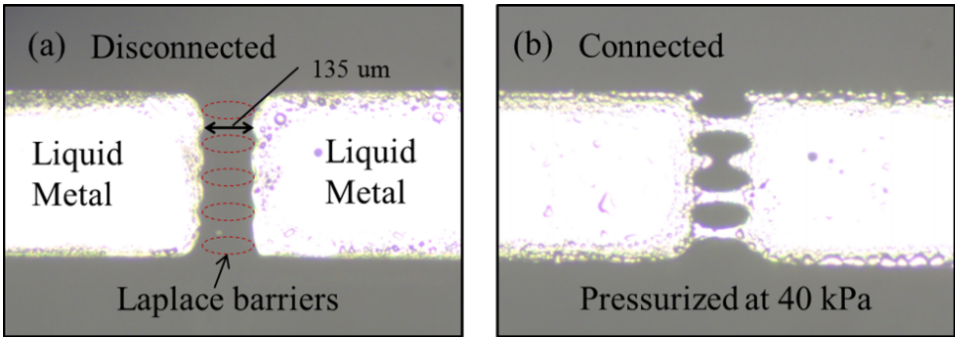

Figure 1.7: Liquid metal RF switch using Laplace barriers utilizing the high surface tension of gallium-based liquid metals as a separation mechanism and high pressure for a connecting mechanism from [24].

Although room-temperature liquid metals have these advantages of high-power handling capabilities, linearity, reversibility, repeatability, and smooth continuous change, they present new challenges of controlling oxidation and corrosion.

Gallium alloy metals will oxidize almost instantaneously when they are exposed to air creating a gallium oxide (Ga_2O_3 and Ga_2O) skin with a significantly reduced conductivity [38–40]. In [41], it was found that fully oxidized Galinstan has approximately 1% of the conductivity of pure Galinstan. In addition, when Galinstan becomes oxidized it will become more viscous and gel-like which will cause it to stick to different surfaces.

This has led to research into different methods of reducing the oxidation of the gallium alloy materials by either keeping it in a low oxygen environment or through different solutions that react with and remove the oxide layer. In [42], it was studied the effects of polyethylene glycol (PEG) and deoxygenated silicone oil for oxidation prevention. In [43], HCl vapor deposition was used on different surfaces to prevent surface wetting. For microwave tunable devices, NaOH solutions have also been used as a co-fluid to prevent oxidation [18, 24] for both filters and switches. These co-fluids have the disadvantage though of reducing the contact area or preventing

electrical connection between the liquid metal and other metals and can decrease the performance of different microwave devices due to their dielectric losses or low conductivity.

Gallium-based metals can also corrode other metals such as copper or stainless steel when exposed for long periods of time, but this corrosion rate is very low and allows for operation of devices for many years [44]. There are surface coatings to prevent corrosion of metals, but more work still needs to be done on conductive coatings that will protect specifically against gallium-based liquid metals.

With the growing evidence of the advantages of liquid metals in microwave devices and expanding research on prevention of oxidation, liquid metal filters have especially been gaining attention. In [19], liquid metal was utilized to tune the coupled split ring resonators in a planar bandpass filter. Band-reconfigurable SIW bandpass filters using liquid metal were demonstrated in [21] which is depicted in Fig. 1.8. An RF MEMS implementation of an evanescent-mode cavity, using a liquid metal droplet in the high electric field region, was demonstrated [20]. In [18], it was shown a SIW bandpass filter with discrete tuning states, enabled using four liquid-metal perturbing posts. Until recently, much of these liquid metal designs have been limited designs by discrete tuning states or planar microstrip designs for any continuously tunable designs. In [17], the coaxial waveguide resonator design in Fig. 1.9 was presented using continuous liquid metal tuning, but this design relies on large CNC metallic cavities which are not practical in all applications. The first demonstration of a design of a continuously tunable design using SIW technology was in [45] and is part of the research work done for this thesis that is detailed in Chapters 2 and 3.

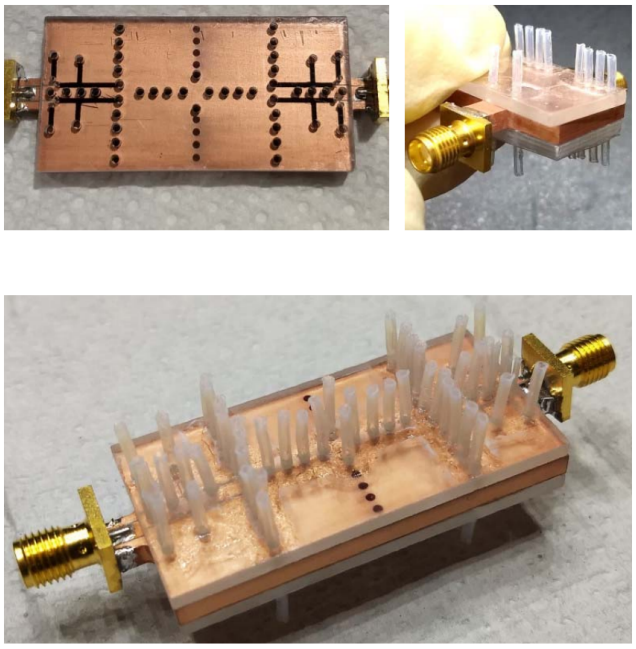

Figure 1.8: Mode-reconfigurable SIW bandpass filter using liquid metal barriers from [21].

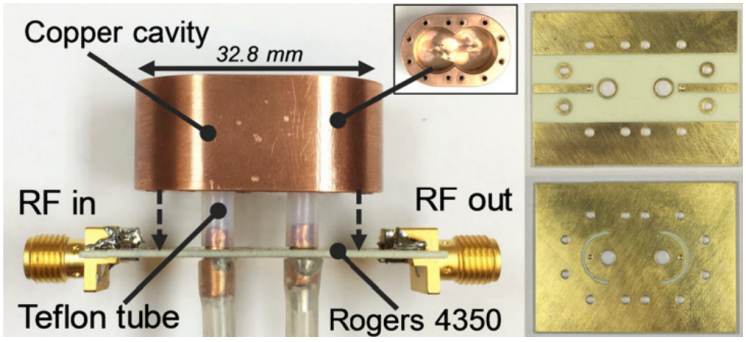

Figure 1.9: Evanescent-mode coaxial waveguide filter using continuous liquid metal tuning from [17].

1.4 Research Objective and Significance

The high power-handling, relatively low loss, and mass manufacturability of substrate integrated waveguide filters have made them a promising technology for tunable filter design. The development of liquid metal actuation in microwave component design has also been growing due to its potential for high power-handling,

linearity, flexibility, self-healing properties, repeatability, and smooth continuous change. This research explores the concept of liquid metal for a continuously-tunable capacitive loading post in a substrate integrated filter design. This liquid metal tuning mechanism is developed to create a frequency-tunable filter design and a fully reconfigurable filter design. This is the first demonstration of this novel liquid metal tuning mechanism, which was presented at the 2019 IEEE MTT-S International Microwave Symposium in the conference paper "Continuously-Tunable Substrate Integrated Waveguide Bandpass Filter Actuated by Liquid Metal" [45]. The work of that conference paper has been expanded to form the contents of Chapters 2 and 3. The design has been further developed to a fully reconfigurable filter with a wide frequency, bandwidth, and shape tuning range. Both these designs expands the work into tunable SIW filter technology and provide promising avenues for highly reconfigurable filters in future adaptive systems.

1.5 Thesis Outline

In Chapter 2, the theory of cavity resonators and evanescent-mode loading will be presented. A square SIW resonator design with a center liquid metal tuning post will then be simulated, fabricated, and measured for its resonant frequency tunability and quality factor. The design and its performance will verify the continuous liquid metal tuning mechanism for more complex filter designs.

Chapter 3 will extend the same tuning mechanism to a second-order filter design. Two of the square SIW resonators with liquid metal tuning from Chapter 2 will be iris coupled into each other to create a second-order filter response that can be tuned across frequency. This design will have static coupling mechanism that will lead to different bandwidths across the frequency tuning range of the device.

Chapter 4 will then implement a fully-reconfigurable bandwidth and center-frequency tunable filter. It will be similar to the design of Chapter 3, but will now incorporate tunable capacitive loading posts in the iris between the two resonators and posts at the ends of the external feeding structures to the filter. These variable coupling mechanisms will allow for continuous reconfigurability of the full filter response.

Chapter 5 will provide a summary of the work and results found. It will also discuss design considerations and work to made in future research into continuously tunable liquid metal devices.

Chapter 2

Resonator and Tuning Mechanism Design

This chapter focuses on the design of a substrate integrated waveguide resonator and a liquid metal tuning mechanism for continuous frequency tuning. The theory of evanescent-mode cavity resonators and the design process of a tunable resonator will be developed. The liquid metal tuning mechanism will be proposed, and the fabrication process to realize the structure will be discussed. The tuning capabilities of the structure will be simulated and experimentally validated, and the quality factor of the liquid metal structure will be extracted. The validation of the liquid metal actuation mechanism for this resonator design lays the groundwork for the frequency-tunable filter of Chapter 3 and fully reconfigurable filter of Chapter 4.

2.1 Resonator Theory

Resonators are the primary building block of filters and are important in the design of oscillators, frequency meters, and tuned amplifiers [46]. The two primary defining parameters for a resonator are its unloaded quality factor Q and its resonant frequency f_r. If these parameters are known, higher-order filters can easily be designed and constructed from the resonator using coupled resonator theory. The response shape and bandwidth of a filter is characterized by the inter-resonator cou-

pling of the resonators and the external coupling of the first and last resonators to the rest of a system, both of which will be discussed further in Chapter 3.

This means that these response characteristics do not depend on the individual resonators as long as each is tuned to the correct resonant frequency (this may not be true though for more advanced filter synthesis responses that rely on asynchronous resonators and complex or active coupling) [47–49]. The quality factor of resonators has an effect on the insertion loss of the final filter response, described by Eq. 2.1 which states that the insertion loss in dB of a filter response is dependent on the fractional bandwidth of the filter Δ, the lowpass prototype coefficients (g-coefficients) of the response g_i, and the quality factor of the i-th resonator Q_i [50].

$$IL(\text{dB}) = \frac{4.343}{\Delta} \sum_{i=1}^{n} \frac{g_i}{Q_i} \tag{2.1}$$

The resonant frequency occurs when the average stored magnetic and stored electric energies are equal $W_m = W_e$. This resonant frequency f_r occurs at

$$f_r = \frac{1}{2\pi\sqrt{LC}}. \tag{2.2}$$

In order to shift the resonant frequency, either the capacitance C or the inductance L of the resonator must be changed. The capacitive loading of liquid metal tuning posts uses this fact to shift the resonant frequency of the resonator down through precise control of an air gap inside the cavity. The quality factor Q is defined as

$$Q = 2\pi f \frac{W_m + W_e}{P_{loss}} \tag{2.3}$$

where P_{loss} is the total loss from conductor, dielectric, and radiation loss. These losses are dependent on the geometry, materials, and manufacturing technology.

2.2 Resonator Design

At microwave frequencies, resonators can be created with waveguides, dielectric resonators, microstrip structures, stripline structures, superconductors, substrate integrated waveguides, and numerous other technologies. For this work, SIW is used for the advantages described in Chapter 1. An SIW cavity resonator can take different shapes, but the two most common and well characterized ones are cylindrical and rectangular waveguide resonators. An unloaded rectangular cavity resonator has a resonant frequency described by

$$f_{mnl} = \frac{c}{2\pi\sqrt{\mu_r \epsilon_r}} \sqrt{\left(\frac{m\pi}{a}\right)^2 + \left(\frac{n\pi}{b}\right)^2 + \left(\frac{l\pi}{d}\right)^2}, \tag{2.4}$$

where m, n, l are the mode numbers and a, b, and d are the cavity resonator dimensions in the x, y, and z direction respectively according to the convention in Fig. 2.1. μ_r is the relative permeability of the material, ϵ_r is the relative permittivity of the material, and c is the speed of light.

There are many possible field distributions that satisfy the electromagnetic boundary conditions of the conductor-surrounded cavity, which are called resonant modes of the cavity. It is desirable to limit the possible modes (especially degenerate modes that are distributed differently but occur at the same frequency) inside the cavity so that power is not taken away from the dominant mode that coupling and tuning structures are designed for. These other modes can be used to produce different desirable effects in applications such as dual-band filters [21] but are not beneficial for this type of tunable single-band design. By designing the thickness b of the cavity to be much thinner than the square wall dimensions a and d, degenerate and spurious modes will exist far away from the dominant TE_{101} mode. By

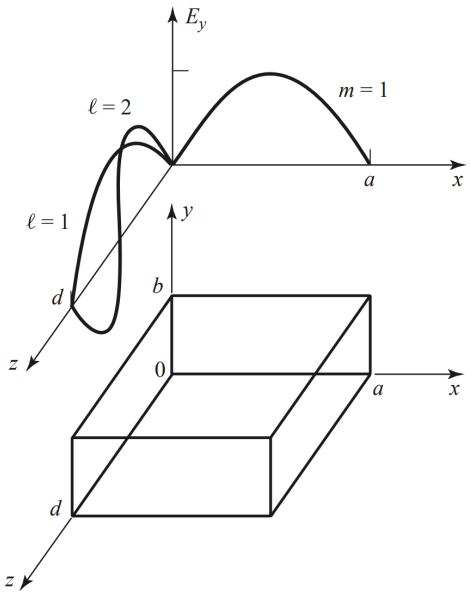

Figure 2.1: Cavity resonator coordinate system with dimension and mode number conventions (from [46]).

considering a square cavity, such that $a = d$, the wall dimensions for the dominant TE_{101} mode at a given frequency is

$$a = \frac{c}{f_{101}\sqrt{2\mu_r\epsilon_r}} \tag{2.5}$$

which is found from Eq. 2.4. This design equation then can calculate the necessary dimensions for the cavity given a selected resonant frequency and board material.

The substrate is selected to be 125 mil copper-clad Rogers TMM3 ($\varepsilon_r = 3.27$, $\tan(\delta) = 0.002$ at $10\,\mathrm{GHz}$) for its desirable material properties. The material has been used extensively for several other SIW filter designs [9, 21, 51]. The thickest available board that is within the capabilities of the available rapid printed circuit board prototyping machines is 125 mil. To have maximum tuning range without over-sensitivity to the liquid metal tuning post, the board must be as thick as possible since thinner boards will require even more precise control on the capacitive

loading height. This is because on a thinner board to achieve the same proportional amount of loading from a post requires smaller volumes and height control. For a resonant frequency of $6\,\mathrm{GHz}$ and $\varepsilon_r = 3.27$ for TMM3, the dimensions of the cavity can be solved to be $19.6\,\mathrm{mm}$ from Eq. 2.5. Since this is a tunable design without strict specifications, the cavity is set to $20\,\mathrm{mm}$ x $20\,\mathrm{mm}$ for simplicity. This larger cavity sets the resonant frequency to be $5.85\,\mathrm{GHz}$.

2.3 Tuning Design

In order to tune the resonant mode of the cavity, a tunable metallic post can be placed at the center of the cavity. This center post perturbs the field distribution inside the cavity by concentrating a stronger electric field in the center gap between the post and the cavity, as seen in Fig. 2.2. There is a lower effective change to the magnetic field distribution so the overall change to the field distribution will be primarily electrical. Perturbation theory states that

$$\frac{\omega - \omega_0}{\omega_0} \approx \frac{\iiint_{\Delta V}(\mu|\bar{H}_0|^2 - \varepsilon|\bar{E}_0|^2)dv}{\iiint_{V_0}(\mu|\bar{H}_0|^2 + \varepsilon|\bar{E}_0|^2)dv}, \tag{2.6}$$

where ω_0 is the resonant angular frequency of the original cavity, V_0 is the cavity volume original cavity, E_0 and H_0 are the electric and magnetic field of the original cavity, ω is the resonant frequency of the perturbed cavity, and ΔV is the change in volume. It can be seen that the change in the resonant frequency of the cavity $(\omega - \omega_0)/\omega_0$ must be negative and result in a frequency downshift whenever the change in volume of the perturbed cavity results in an increase of stored energy.

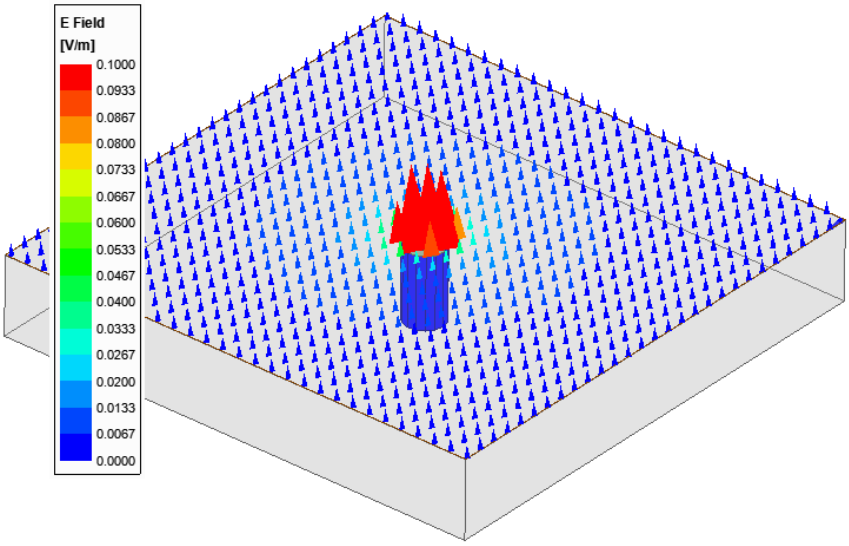

(a)

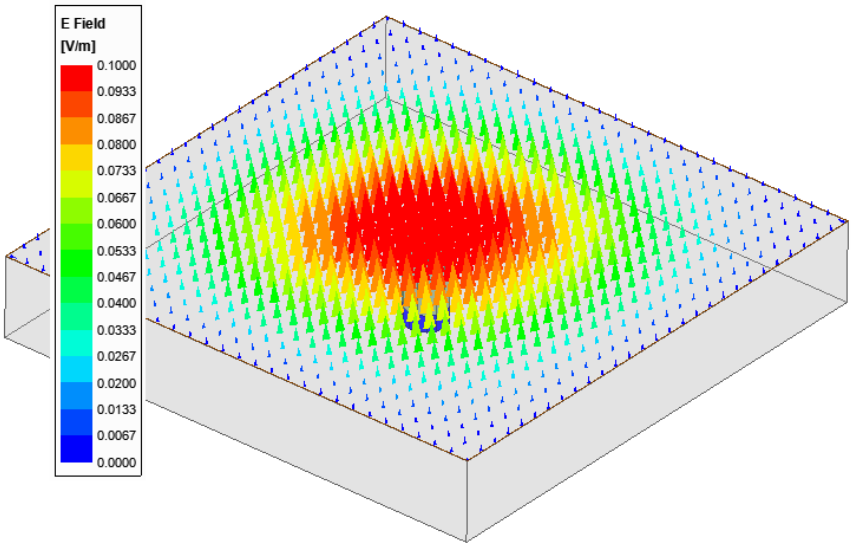

(b)

Figure 2.2: E-field comparison between a square cavity resonator with a capacitive loading post with a a) 10 mil air gap and b) 100 mil air gap. The two cavities resonate at $4.8\,\mathrm{GHz}$ and $5.9\,\mathrm{GHz}$ respectively. The E-field plots have the same magnitude scaling, and it can be seen that there is a stronger concentration of E-field at the center of the cavity for the 10 mil air gap.

The increase in stored electrical energy in the gap between the post and top of the cavity can also be understood as a capacitive increase since

$$C = \frac{2W_e}{V^2} \tag{2.7}$$

where C is capacitance, W_e is the stored electric field, and V is the voltage across the separated conductors which are the post and top of the cavity in this case. Eq. 2.2 predicts this increased capacitance must result in a decreased resonant frequency similar to the prediction from perturbation theory. This frequency downshifted resonant mode is referred to as an evanescent mode since it is at a frequency lower than the propagating cutoff frequency of an equivalent waveguide. Since the fields resonate rather than propagate within a cavity, it is possible for these evanescent modes to still exist in the rectangular waveguide cavity below the cutoff frequency.

The total quality factor of the resonator is described by

$$\frac{1}{Q_T} = \frac{1}{Q_c} + \frac{1}{Q_d} \tag{2.8}$$

where Q_T is the total quality factor, Q_c is the quality factor when considering only the conductor losses, and Q_d is the quality factor when considering only the dielectric losses. From the field plots of Fig. 2.2, it can be seen that when the cavity is more heavily capacitively loaded the fields will be concentrated more in the region above the post which for this case will an air region. At lower loaded states, the fields are distributed more through the dielectric cavity, which leads to lower dielectric losses and a higher Q_d for small capacitive air gaps. As this capacitive air gap becomes smaller, it also affects the surface current density along the conductors. In order to support the stronger E-fields at the center of the cavity near the

post, a higher surface current density must flow along the inner conductor rather than the outer conductor of the cavity walls. This surface current density creates conductor losses along the inner conductor, and there exists a ratio between the size of the inner conductor and the outer conductor that maximizes the total conductor quality factor. For a cylindrical coaxial resonator with the same material for both the inner and outer conductor, this ratio is known to be 1:3.6 for the inner and outer radii [52]. There is not a simple closed-form expression for this ratio for a square resonator when both conductors are different, but this state can be found through FEM solvers. For this design, the ideal ratio to maximize the conductor quality factor would require a large center tuning post, which is impractical for a liquid metal channel. The diameter of the liquid metal tuning post must be small so that the surface tension of Galinstan keeps the liquid metal slug intact from small vibrations or tilting. From best practice of previous projects [41] and simulations on the tunability of the post due to its diameter, the diameter of the tuning post was eventually chosen to be $1.6\,\mathrm{mm}$. The available Teflon tubing sizes and materials from previous work on liquid metal filters also influenced the final choice of the post radius.

Tunable metallic posts are well established and have been realized in the past with tunable screws and piezoelectric actuators [6, 7, 9, 12]. With the growing interest in liquid metal tunable RF devices as detailed in Section 1.3, this work presents a novel mechanism for continuous tuning of the resonant frequency through a Galinstan liquid metal post. The proposed mechanism is shown in Fig. 2.3. A drilled unplated via is made through the substrate which will be the channel that the liquid metal will flow through within the substrate. When this channel is partially filled, the slug of liquid metal within the substrate will act as a capacitive loading post as long as 1) it is electrically connected to the outside walls of the cavity and 2) the cavity copper on the top of the substrate remains mostly intact. This tunable post

has the benefit over piezoelectric actuator tuned cavity resonators because it has a much wider tuning range due to being able to fully unload and reload the post via rather than only relying on micron range deflection of a piezoelectric disk actuator.

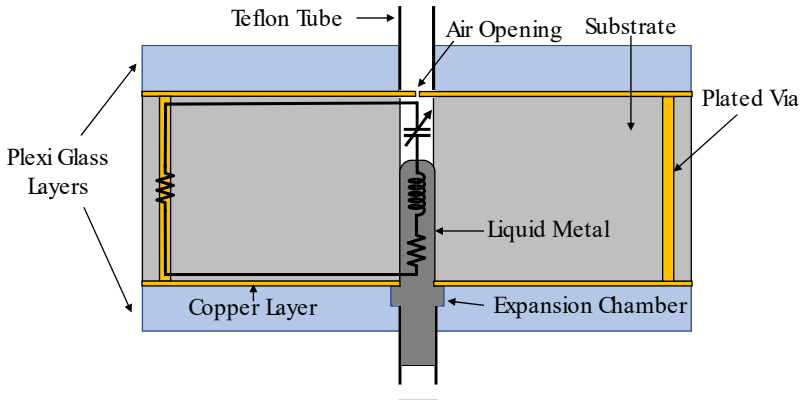

Figure 2.3: Cross-section of the liquid metal post tuning structure with equivalent circuit of the structure overlaid.

Teflon tubes are used to supply the liquid metal to the device and Plexiglass is placed on the top and bottom of the substrate to act as interfaces for the Teflon tubes. No Galinstan passes through the top Teflon tube, but it was included in the design for future implementations that may include a closed loop system or for any leaked Galinstan from the top to be contained. To create a strong electrical connection with the outer walls of the cavity, an expansion chamber in the Plexiglass is drilled so that there is a larger surface over which the Galinstan will make contact with the bottom of the cavity. To create an intact top copper diaphragm, the drilled unplated via is only partially drilled through the substrate with a small opening created in the diaphragm to allow for air to pass through. If this air opening is not included, the air in gap between the liquid metal slug and the top of the cavity will become compressed as the liquid metal is injected. This will create higher pressures than the supporting structures and top copper diaphragm can withstand.

The equivalent electrical circuit of the tuning mechanism is also included in

Fig. 2.3 with the air gap between the liquid metal post and top diaphragm being an equivalent tunable capacitance. The center liquid metal post acts as an equivalent inductance, and there exist resistive losses in the Galinstan and the copper of the cavity walls. There exist approximate closed form expressions for these equivalent inductance and capacitance of evanescent-mode cavity resonators [53].

2.4 Simulation of Resonator Tuning and Quality Factor

Knowing the size of the cavity and the tuning post radius, an electromagnetic finite element modeling software such as ANSYS HFSS can be used to find more realistic predictions of the behavior of the resonator before it is fully fabricated. This is achieved by solving for the electromagnetic fields of the material while accounting for material effects and geometries that are difficult to solve analytically. There are two primary solution types in ANSYS HFSS for these types of filter designs: Eigenmode and Driven Modal solutions. Eigenmode simulations solve for the fundamental modes of a given geometry and are useful especially for cavity resonators design. They have the benefit of being fast but do not show the behavior of the structure at non-resonant frequencies. Driven Modal solutions allow for solving over frequency sweeps rather than only the fundamental modes and will be used to find the simulated frequency response of the structure to be later compare with measured results. These solutions are slower than Eigenmode solutions and are typically saved for later iterations of the design after the groundwork of the design has been fully established.

Taking the given parameters of a $20\,\mathrm{mm}$ x $20\,\mathrm{mm}$ square cavity on 125-mil TMM3 with a $1.6\,\mathrm{mm}$ tuning post in the center, Fig. 2.4 is the resulting Eigenmode HFSS model of the tunable cavity resonator. For realistic quality factor results,

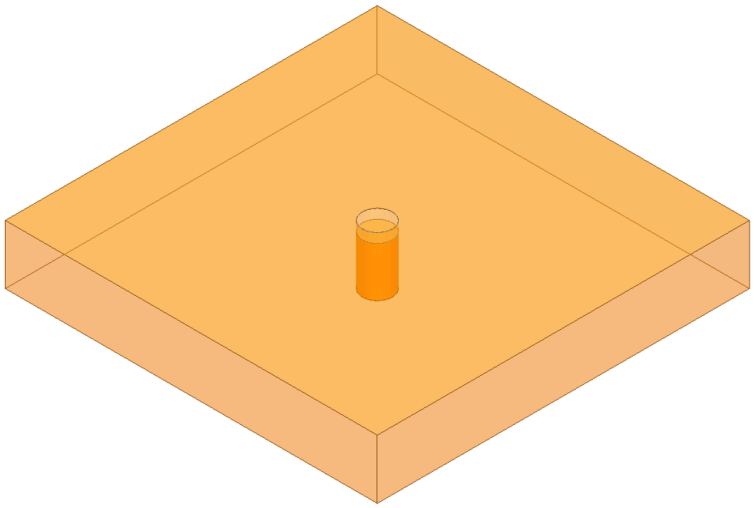

Figure 2.4: Eigenmode HFSS model of the tunable cavity resonator.

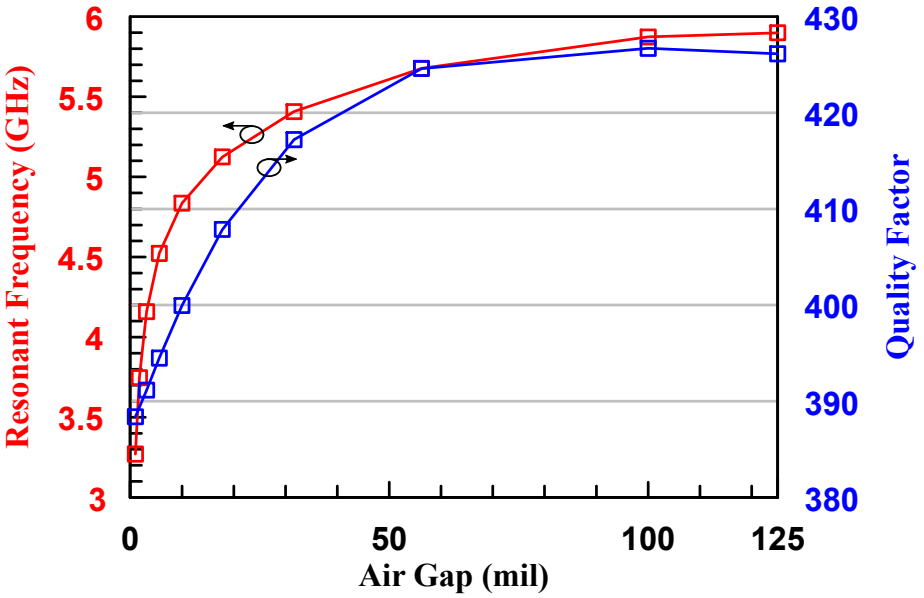

Figure 2.5: Simulated resonant frequency (red trace) and quality factor (blue trace) of the cavity at different capacitive air gap heights between the cavity diaphragm and the top of the Galinstan post.

the conductivity of the cavity walls were set to copper ($\rho = 5.8 \times 10^7\,\mathrm{S\,m^{-1}}$), the conductivity of the center post was set to Galinstan ($\rho = 3.46 \times 10^6\,\mathrm{S\,m^{-1}}$).

The model was simulated for different air gap heights, and the resulting simulated resonant frequency of the cavity is recorded in Fig. 2.5. For smaller air gap heights, the resonant frequency decreases logarithmically due to the evanescent modes predicted from both field and circuit theory. It should be noted that the theoretical $5.85\,\mathrm{GHz}$ resonant frequency of the empty unloaded filter has instead been shifted to $5.9\,\mathrm{GHz}$. This small shift is due to the unplated air via at the center of the resonator, which decreases the effective permittivity of the cavity by adding a mall volume of air $\varepsilon_r = 1$ to that of the original TMM3 permittivity of $\varepsilon_r = 3.27$. From Eq. 2.4, this decrease in the effective permittivity will result in a slight increase in the resonant frequency of the cavity. The unloaded quality factor of the cavity as a function of different air gaps is also depicted on the right y-axis in Fig. 2.5. As the air gap becomes more heavily loaded, stronger surface currents will flow through center liquid metal post causing increased conductor loss. This results in a quality factor ranging from 388 at $3.3\,\mathrm{GHz}$ to 426 at $5.9\,\mathrm{GHz}$, which is about the expected value for this type of SIW resonator design.

With the preliminary Eigenmode simulations verifying the expected behavior of the cavity resonator from the theoretical calculations and the frequency tunability of the center Galinstan post, the Driven Modal model in Fig. 2.6 was created in HFSS. On two opposite ends of the resonator are grounded coplanar waveguide (GCPW) transmission lines. These act as the feed port into the cavity and are coupled to the transmission line by extending the GCPW gaps as feed lines into the cavity. This creates a magnetic coupling between the magnetic fields of the cavity and the GCPW transmission line. The distance that the feed lines are inserted into the cavity has an effect on how strongly the fields will couple, but for detailed analysis of

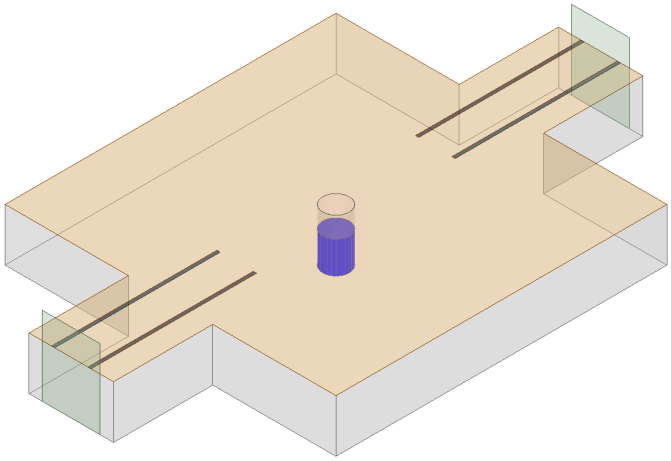

Figure 2.6: Driven Modal model of the final strongly coupled resonator design in ANSYS HFSS.

its effects refer to [53,54]. The feed lines were inserted $4\,\mathrm{mm}$ on both sides into the cavity resonator to provide coupling to see the behavior of the resonator across frequency and thereby further verify the tunability of the resonator. The Driven Modal model was swept across frequency and for different loading heights of the center tuning post, and the resulting simulated frequency response at different tuning states of the resonator is depicted in Fig. 2.7. It can be seen that the frequency response of the resonator tunes across the tuning band of $3.3\,\mathrm{GHz}$ to $5.8\,\mathrm{GHz}$ and confirms the frequency tunability of the devices. The unloaded frequency of $5.8\,\mathrm{GHz}$ is slightly lower in frequency than the Eigenmode simulation resonant frequency of $5.9\,\mathrm{GHz}$ due to the fact that the GCPW feed lines slightly expand the effective size of the cavity. The external coupling of the feed network is less strong at lower frequencies. This is due to the fact that at lower frequencies the wavelength of the fields becomes larger, which means that the relative size of the feed lines into the cavity compared to the wavelength of the fields decreases. This explains the increase in the insertion loss of the resonator at the lower frequencies.

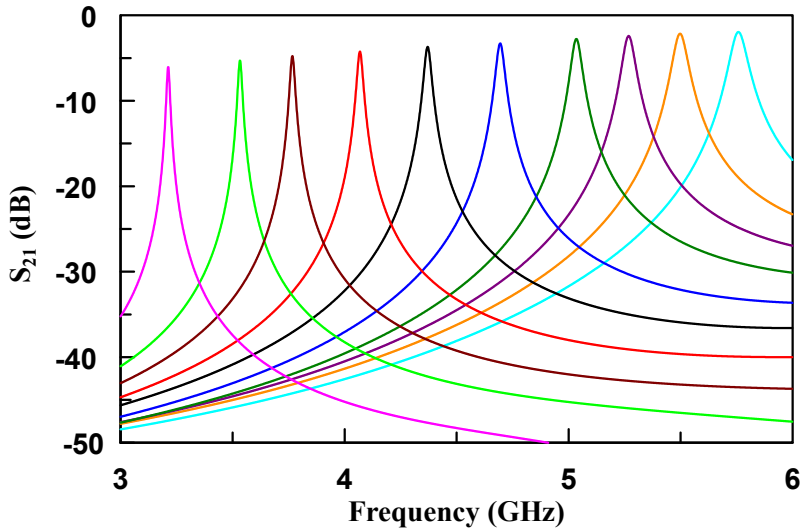

Figure 2.7: Frequency response of the resonator at different tuning gap heights

2.5 Practical Design Realization and Fabrication

In order to ease fabrication, it is better to replace the edge side walls of the resonator with a via cage. This is more realistic of how an SIW resonator or filter would be implemented in a system since it is easier with PCB fabrication technology to have plated via holes rather than full routed cutouts of the shape of the resonator. The diameter of vias d is recommended to be less than $\lambda_g/5$ where λ_g is the guided wavelength, and the pitch p spacing between vias is less than or equal to the diameter [55]. The effects of the via cage spacing was studied in [55], and the region of interest for the via diameter and pitch are plotted in Fig. 2.8. Each gap between the vias can be thought of as an open waveguide, and as long as the cutoff frequency of the waveguide is higher than the operating frequency of the resonator, there is no significant leakage of the fields. The inclusion of the via cage does slightly increase the effective size of the cavity since the fields will extend outwards further, but this effect is small enough that it can be ignored since there

are no strict frequency specifications for this design. The final dimensions of the different features in the resonator design are recorded in Fig. 2.9.

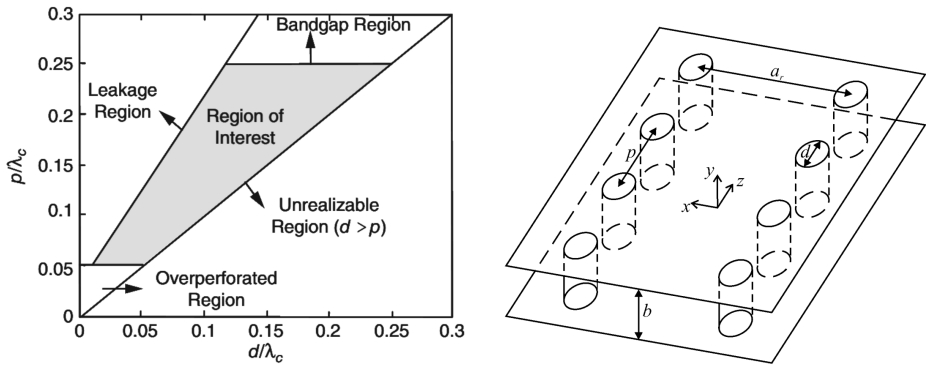

Figure 2.8: a) Relationship between the via diameter d and pitch p with respect to the guided wavelength λ_c for an SIW via cage and b) three-dimensional view of an SIW with labelled physical parameters (from [55]).

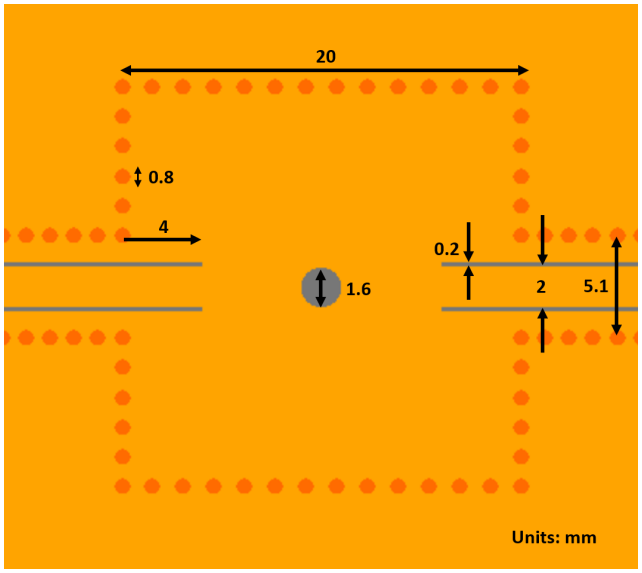

Figure 2.9: Dimensions of the final evanescent-mode liquid metal tunable resonator.

With the design of the resonator and tuning mechanism established and simulated, the resonator needs to be fabricated and tested. This is to verify that the results from simulation match with realistic fabrication and material tolerances and

that the tuning mechanism is practical in real applications.

The via cage holes of the board were first drilled using an LPKF ProtoMat S103 circuit board plotter along with four fiducial vias at the corners of the board, which will be used for alignment of the design for later drilling steps. The board is then electroless plated, allowing for the chemical deposition of trace amounts of copper onto the surface of the board and inside each of the vias. This is done by cleaning the board and then placing it in a catalyst solution that deposits a monolayer of palladium, to which copper ions can bond onto the substrate material. This lines the inside of the vias with trace amounts of copper, but it is not a thick enough layer of copper since typical electroless copper plating deposits about 0.7 to $2\,\mu\mathrm{m}$ of copper thickness [56].

At radio frequencies, the currents in a piece of conductor flow only on the surface of the conductor rather than throughout the entirety of the conductor at lower frequencies and DC. This is known as the skin effect, and the skin depth that the current penetrates into the conductor is frequency dependent and described by

$$\delta = \sqrt{\frac{1}{\pi f \mu \sigma}} \tag{2.9}$$

where f is the operating frequency, μ is the permeability of the material, and σ is the conductivity of the material. For copper ($\sigma = 5.8 \times 10^7\,\mathrm{S\,m^{-1}}$) and lowest operating frequency being $3\,\mathrm{GHz}$, the maximum operating skin depth can be found to be $1.2\,\mu\mathrm{m}$. This is close to the copper thickness layer from electroless plating, and if the layer of copper is too thin then the current paths of the cavity will experience greater resistances that decrease the overall quality factor of the resonator. As a rule of thumb, the conductor thickness should be at least five skin depths which for this application is $6\,\mu\mathrm{m}$ [52].

In order to deposit a thicker layer of copper, an electroplating process can be done. The board is placed between two copper plates inside a copper ion carrier solution, and a voltage is applied onto the two outer copper plates compared to the center plating board. This electrical potential causes copper ions to carry charge from the outer copper plates and deposit onto the plating board. This process allows for thicker deposition of copper onto a PCB, but it is only able to deposit copper onto conductive surfaces that can accept the charged copper ions. This is why the board must be electroless plated first in order to deposit a thin layer of copper so that the electroplating process can apply a thicker layer. With the electroplating process, about $15\,\mu\mathrm{m}$ of additional copper is plated onto the board which exceeds the minimum recommended requirement of $6\,\mu\mathrm{m}$.

The next step is to create the air openings on the top of the resonator which allow for pressure release from the air gap. In early designs, this was done by bringing the board back to the LPKF ProtoMat S103 and using a $0.2\,\mathrm{mm}$ microcutter to tap a small air opening in the design (the results of which can be seen in Fig. 2.10). In the later designs, an LPKF ProtoLaser U4 became available and was used since it is able to pattern designs onto PCBs with a laser, which allows for smaller and more precise patterning. The change in the air opening fabrication step and its results are discussed further in Chapter 4. The air opening was not accounted for in simulation since it is small relative to the radius of the tuning post and should not significantly impact the tuning performance of the resonator.

To remove copper and substrate from the bottom of the tuning post without breaking the copper on the top of the resonator requires precise depth control milling. Unfortunately, the LPKF ProtoMat S103 is not accurate in its depth control and calibration since it uses a sled based calibration that calibrates the height of the drill bit according to a calibrated slope. This is only to calibrate the location of the drill

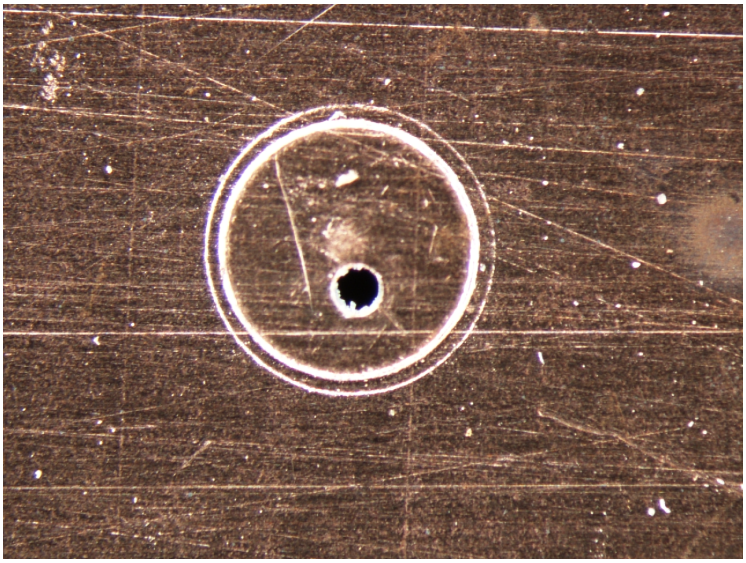

Figure 2.10: Microscope image of the air opening placed on the top of the board with bulges around the edges, which is the outline of the tuning post radius due to the pressure applied when drilling from the back.

bit relative to the head of the milling machine, but it has no way of measuring the height of the substrate it is milling into. For this, a second circuit board plotter (the T-Tech Quick Circuit J5) must be used since at the start of any milling process it has a substrate height calibration step. The T-Tech moves a conductive foot and places it onto the substrate, then it lowers any drill bit it is holding slowly and stops when it senses an electrical connection between the foot touching a copper substrate and the metal drill bit. This allows for precise depth control in the range of $20\,\mu\mathrm{m}$ which is necessary to prevent the copper diaphragm from being punctured. Using the T-Tech, it is possible to drill down and remove the majority of the substrate in the via without puncturing the copper diaphragm. This is a slow and careful process but when complete it is possible to see light reflect off the bottom of the via hole which indicates that copper was reached. From Fig. 2.10, a deformation can be seen on the opposite side from the pressure that the drill bit places onto the back of the copper diaphragm. As long as the diaphragm is not punctured and the majority of

the copper is removed, the imprint from the drill does not create significant issues for the design.

The disadvantage of using the T-Tech Quick Circuit J5 is that the software is not sophisticated, and it does not align to fiducial holes well. In order to align the design between the LPKF and the T-Tech, alignment set pins holes must be drilled in the PCB. The T-Tech has two $3.3\,\mathrm{mm}$ set pins that are placed $100\,\mathrm{mm}$ apart from each other which can be used to align the board onto the T-Tech. The LPKF ProtoMat S103 is used to drill the set pins into the PCB, and it is then moved to the T-Tech where the design is aligned and the tuning post vias can be drilled.

The board is then taken back to the LPKF ProtoMat S103, and any final unplated through-holes are drilled through the board. The entire device is then contour routed out of the board, and end launch SMA connectors are soldered to the ends of the GCPW lines of the device. The final fabricated resonator can be seen in Fig. 2.11.

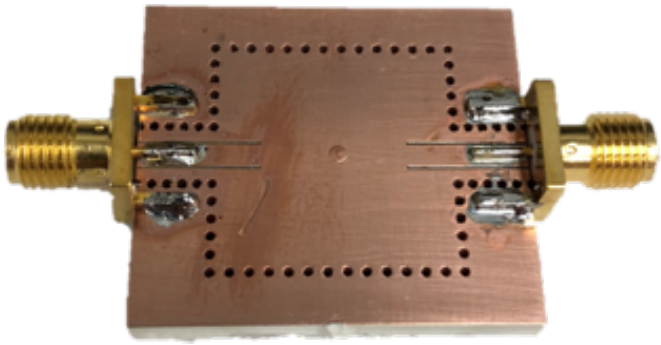

Figure 2.11: Top photograph of the fabricated SIW evanescent mode cavity resonator

A cross-sectional view of the fabrication process for the resonator structure is shown in Fig. 2.12. Unplated vias are drilled through the copper and substrate layers. The entire board is then copper plated. A microcutter is used to tap the top

of the structure to create a small air opening in only the top copper layer. The board is flipped over and the T-Tech is then used to drill a partial via through the bottom copper and substrate layer. The board is flipped over again and contour routed out to create the finished resonator structure.

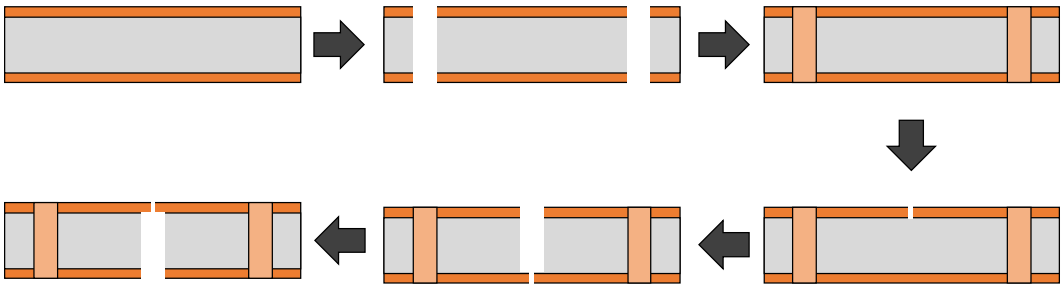

Figure 2.12: Fabrication process of the resonator structure with air opening and copper diaphragm.

Finally, Plexiglass pieces are cut out to same the size as the resonator with a hole at the location of the tuning via. Teflon tubes are epoxied into the holes in the Plexiglass and the entire interface is then clamped onto the top and bottom of the resonator. A syringe filled with liquid metal is then connected to the Teflon tube where Galinstan can be manually injected into the resonator.

2.6 Measurements and Results

The fabricated design is manually loaded with liquid metal and measured with the Keysight Technologies N5225A network analyzer. The simulated and measured results of the strongly coupled resonator are shown in Fig. 2.13. The continuous frequency tunability of the liquid metal post is confirmed by the measured results and line up with what is expected from simulation. This validates the potential of continuous liquid metal tuning for SIW cavity resonators in further filter designs.

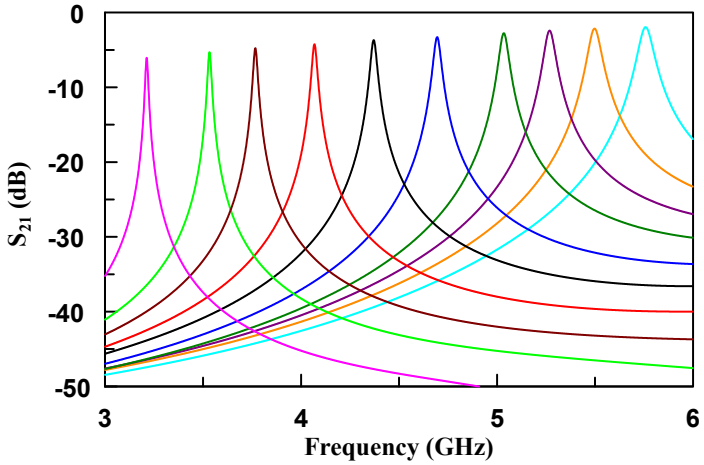

(a) Simulated response

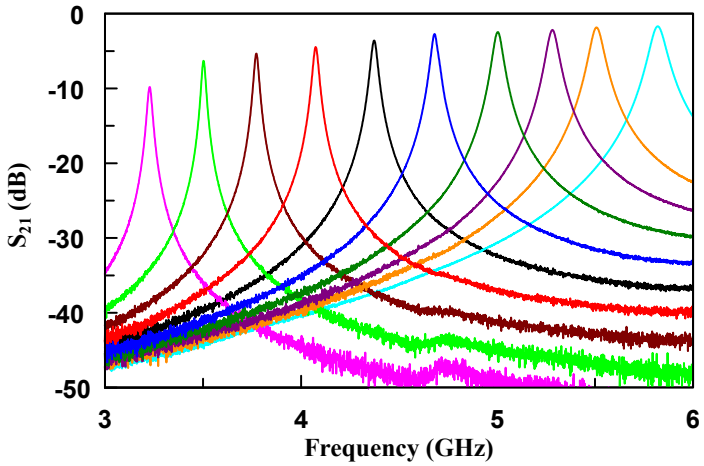

(b) Measured response

Figure 2.13: Simulated and measured S_{21} response of the resonator at different tuning states.

It is necessary to also measure the quality factor of the measured sample. When a resonator is loaded by a source and load circuit impedance, the unloaded quality factor Q_u of the resonator will be affected by the quality factor of the external loads Q_{ext} according to

$$\frac{1}{Q_L} = \frac{1}{Q_u} + \frac{1}{Q_{ext}}. \tag{2.10}$$

It is not possible in reality to measure the true unloaded quality factor Q_u of a resonator since it will always be connected to system impedance of the measurement equipment, but it can be approximated by allowing for a large Q_{ext} such that $Q_u \approxeq Q_L$, which is done by decreasing the input coupling to the resonator. This relation from a measured response can also be expressed as

$$Q_u = \frac{Q_L}{1 - |S_{21}|}. \tag{2.11}$$

For accurate measurement of Q_u, the forward transmission coefficient S_{21} at the resonant frequency should be below $-20\,\mathrm{dB}$ but not too low that the peak is buried in the noise. When measuring the response of a resonator, the unloaded quality factor Q_u will approximately equal the unloaded quality factor Q_L which is calculated by

$$Q_L = \frac{f_r}{\Delta f_{\text{3dB}}} \tag{2.12}$$

where f_{3dB} is the $3\,\mathrm{dB}$ bandwidth from the peak of the response. For this, a second weakly coupled resonator is fabricated with shortened feed lines that instead of extending $4\,\mathrm{mm}$ into the cavity, extend $0\,\mathrm{mm}$ and stop where the transmission line meets the edge of the square cavity. The bandwidth around the resonant frequency peak of the response is then taken, and the quality factor is found.

The measured quality factor extracted from the resonator is plotted in Fig. 2.14 along with the simulated Q of the cavity. The quality factor of the resonator drops significantly compared to simulation when the resonator is highly loaded at lower frequencies. This lower unloaded quality factor has been observed before in the literature and has been attributed to the decreased conductivity due to surface oxidation of Galinstan [41]. The oxide layer reduces the conductivity of the Galinstan

significantly which introduces more losses to the resonator and a lower quality factor. Mitigation effects of the oxide layer is possible through different co-fluids or low oxygen environments as detailed in Section 1.3. For now, the effective conductivity of the Galinstan is extracted by simulating the unloaded quality factor as a function of different center post conductivities. Using the data sample at $4.7\,\mathrm{GHz}$, the measured quality factor of the fabricated filter was 227.5. An Eigenmode simulation was done that varied the center post conductivity and a logarithmic relationship between the conductivity and quality factor as plotted in Fig. 2.15. Using this simulated data, an unloaded quality factor of 227.5 corresponds to an inner tuning post conductivity of $5.0 \times 10^4\,\mathrm{S\,m^{-1}}$ which is 1.4% of the conductivity of pure Galinstan. This is consistent with the results from [41] which extracted a value of 1% the conductivity of pure Galinstan through a similar unloaded quality factor calculation when the Galinstan is heavily oxidized.

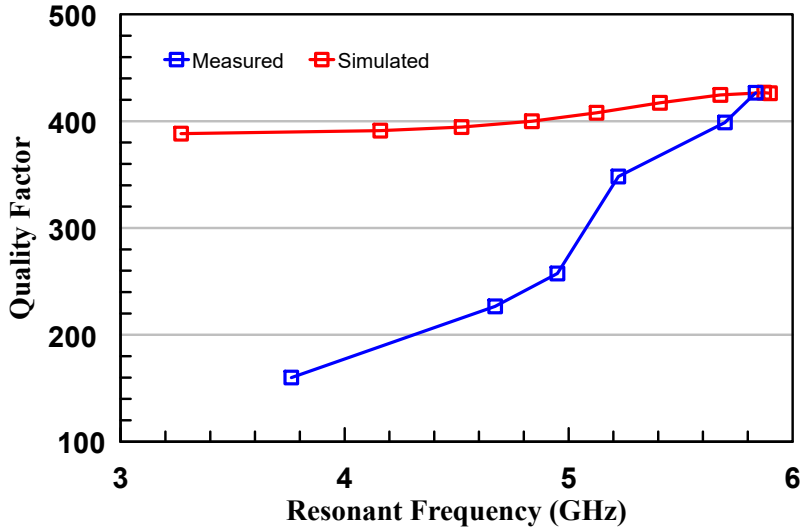

Figure 2.14: Measured and simulated unloaded quality factor of the loaded cavity resonator as a function of resonant frequency.

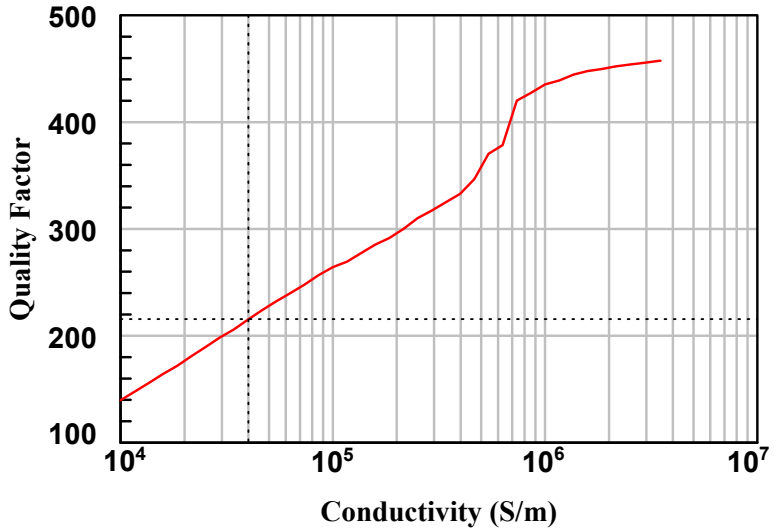

Figure 2.15: Simulated quality factor of the loaded cavity at $4.7\,\mathrm{GHz}$ as a function of different conductivities of the center Galinstan post.

2.7 Summary

A substrate-integrated-waveguide evanescent-mode resonator was designed with the inclusion of a continuously tunable capacitive post. This tuning post was implemented with a novel liquid metal tuning mechanism that allows greater range and flexibility for evanescent-mode resonators than piezoelectric actuators or tuning screws. The simulated and measured designs show good agreement of the resonators tuning capabilities from $3.3\,\mathrm{GHz}$ to $5.8\,\mathrm{GHz}$. The quality factor of the resonator was also extracted and found to range from 160 at $3.8\,\mathrm{GHz}$ to 530 at $5.8\,\mathrm{GHz}$. The resonator has been fully characterized, and the tuning mechanism verified to achieve the designed tuning range. This resonator can now be used as the building block for the synthesis and design of a frequency tunable second-order filter in Chapter 3 and a fully reconfigurable filter in Chapter 4.

Chapter 3

Frequency-Tunable Filter Design and Realization

This chapter uses the tunable resonator design from Chapter 2 as a building block for the design of a second-order frequency-tunable bandpass filter design. Coupled filter theory will be developed, which will be used to design the external coupling and inter-resonator coupling structures of the design. Methods for characterizing these coupling structures will be explained and used to finalize the dimensions of the design. The device will then be simulated, fabricated, and experimentally validated for its continuous frequency tunability using liquid metal actuation. The results of this design demonstrates the capabilities of continuous liquid metal tuning in filter design and the potential for future applications and more advanced reconfigurable designs like the one that will be presented in Chapter 4.

3.1 Filter Theory

Different filter polynomials types and synthesis techniques have been studied such as Butterworth, Chebyshev, Bessel, and Elliptical polynomials which have varying advantages and trade-offs in the response they generate [46, 57]. From each of these different polynomials, parameters called the g-coefficients can be extracted from successive polynomial division of the N-th order filter polynomial.

For a lumped element ladder lowpass prototype network, these g-coefficients directly correspond to the values of the lumped elements if the normalized network has an impedance of $1\,\Omega$ for g_0, as shown in Fig. 3.1. There are also known transformations (see [46]) to create lumped element ladder bandpass filters from these g-coefficients so that they can be realized in the form shown Fig. 3.2.

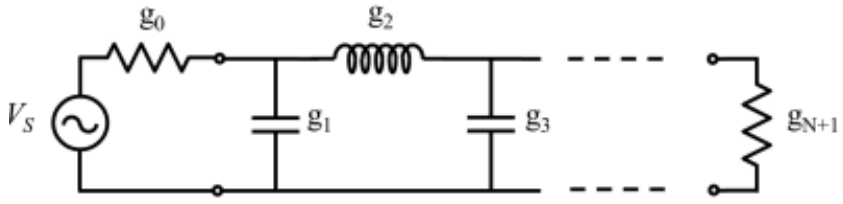

Figure 3.1: Lumped element ladder lowpass filter

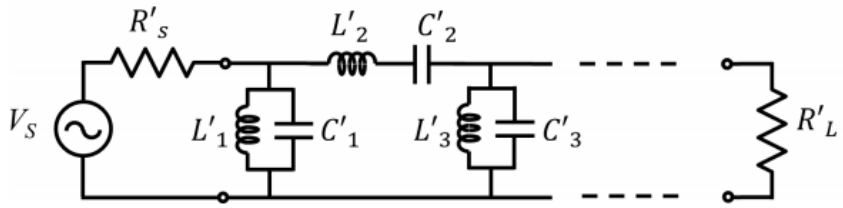

Figure 3.2: Lumped element ladder bandpass filter

In reality, such designs are difficult to implement since the inductor and capacitor values will vary greatly for different stages of the design. This problem is solved with impedance or admittance inverters (represented in Fig. 3.3) in the filter design which transform inverter input admittance or impedance from one port to the other. Due to the behavior of these inverters, it is possible to replace the lumped element ladder bandpass filter of Fig. 3.2 with the equivalent circuit shown in Fig. 3.4. The result is a network of J-inverters connecting together shunt resonators which will behave the same as the ladder bandpass filter in Fig. 3.2.

This makes the design of microwave filters simpler since each lumped element

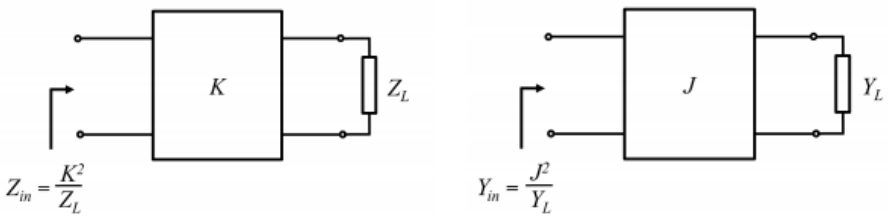

(a) (b)

Figure 3.3: Input impedance or admittance from (a) K-inverter and (b) J-inverter.

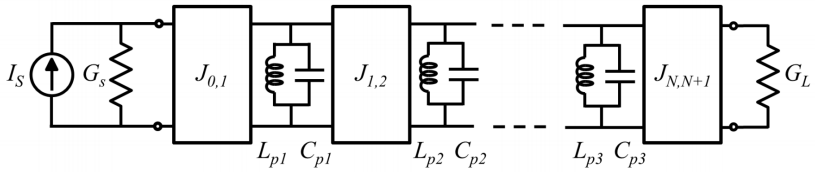

Figure 3.4: Bandpass filter realized with shunt LC tank resonators connected by J-inverters.

inductor and capacitor parallel tank circuit can easily be replaced with the same distributed element resonator, like the one designed and characterized in Chapter 2. The inverters can be realized with lumped elements, distributed structures such as a quarter-wavelength transmission line, or either inductive or capacitive coupling between adjacent resonators.

For the coupled SIW evanescent-mode resonators filter design of this work, each inverter in Fig. 3.4 can then be understood as different coupling mechanisms. In this context, the external coupling is represented by the first and last J-inverters, $J_{0,1}$ and $J_{N,N+1}$, that connect to the source or load impedance. The external coupling was discussed briefly in Chapter 2 for the weak or strong coupling from the GCPW line to the resonator. The inter-resonator coupling is represented by intermediary J-inverters, which either inductively or capacitively couple energy between the resonators. For SIW resonator designs, coupling typically is done with inductive irises that connect two different cylindrical or rectangular cavities together.

The advantage of admittance or impedance inverter models is that the relative values of the g-coefficients will not have an effect on the inductance or capacitance values of the individual resonators. Instead, the realization of the g-coefficients is done through varying of the inverter values. This allows for more flexibility in resonator design and tuning since the resonators can be cascaded to each other with only consideration for the coupling between them. The resonant frequency and quality factor of each resonator still needs to be considered, which is why they were extracted in Chapter 2, but the precise inductance or capacitance values become less important. From the g-coefficients of an N-th order filter, the J-inverter values can be calculated from the following equations with known source resistance R_s, load resistance R_L, and i-th resonator capacitance C_i

$$J_{0,1} = \sqrt{\frac{2\pi f \Delta C_1}{R_s g_0 g_1}} \tag{3.1a}$$

$$J_{i,i+1} = 2\pi f \Delta \sqrt{\frac{C_i C_{i+1}}{g_i g_{i+1}}} \tag{3.1b}$$

$$J_{N,N+1} = \sqrt{\frac{2\pi f \Delta C_N}{R_L g_N g_{N+1}}} \tag{3.1c}$$

$$L_i = \frac{1}{4\pi^2 f C_i} \tag{3.1d}$$

which gives the corresponding J-inverter values and resonator inductance, and Δ is the fractional bandwidth of the filter. These inverters are better for design and calculation but are difficult to measure and quantify for actual filters. Instead, it was shown by Dishal that the resonant frequency of each resonator f_0, the inter-resonator coupling coefficient $k_{i,i+1}$, and the external quality factor of the first or last resonator Q_{ext} can be used instead to fully characterize any narrowband filter

design [58]. The Q_{ext} and $k_{i,i+1}$ for an N-th order filter is calculated by

$$Q_{ext1} = \frac{g_0 g_1}{\Delta} \tag{3.2}$$

$$k_{i,i+1} = \frac{\Delta}{\sqrt{g_i g_{i+1}}} \tag{3.3}$$

$$Q_{extN} = \frac{g_N g_{N+1}}{\Delta}. \tag{3.4}$$

They can be related back to the J-inverters with the following equations:

$$J_{0,1} = \frac{1}{{Q_{ext1}}^2} \sqrt{\frac{2\pi f C_1}{R_s}} \tag{3.5a}$$

$$J_{i,i+1} = k_{i,i+1} \left(2\pi f \sqrt{C_i C_{i+1}}\right) \tag{3.5b}$$

$$J_{N,N+1} = \frac{1}{{Q_{ext2}}^2} \sqrt{\frac{2\pi f C_N}{R_s}}. \tag{3.5c}$$

Note that the new coupling parameters isolate out the effects of the resonator capacitance, system impedance, and resonant frequency from the J-inverter values. The coupling parameters of Q_{ext} and $k_{i,i+1}$ can then be easily extracted from the behavior of the device and can be correlated directly to changes in the physical dimensions of the coupling structure. The method of extracting these coupling parameters from different coupling geometries will be discussed in the next section.

3.2 Filter Design

From the resonator design in Chapter 2, it was found that a tuning range of $2.4\,\mathrm{GHz}$ is possible from $3.3\,\mathrm{GHz}$ to $9\,\mathrm{GHz}$. At the lower frequencies, the liquid metal post is heavily loaded, and a precise air gap is more difficult to achieve and maintain without an automated injection method. This is also the reason why

the measured quality factor of Fig. 2.14 only extends down to $3.8\,\mathrm{GHz}$ since the weakly coupled sample was difficult to tune and maintain at lower frequencies. For this design, manual injection of Galinstan through syringes is still used, so in order to allow for tuning tolerances, only the range of $3.8\,\mathrm{GHz}$ to $5.9\,\mathrm{GHz}$ is considered in the initial design. To demonstrate the capabilities of a continuously tunable Galinstan post in a filter, a $0.1\,\mathrm{dB}$-ripple Chebyshev second-order bandpass filter is designed. The design will be implemented with the same $20\,\mathrm{mm}$ x $20\,\mathrm{mm}$ square evanescent-mode SIW cavity resonator in a 125-mil-thick TMM3 board.

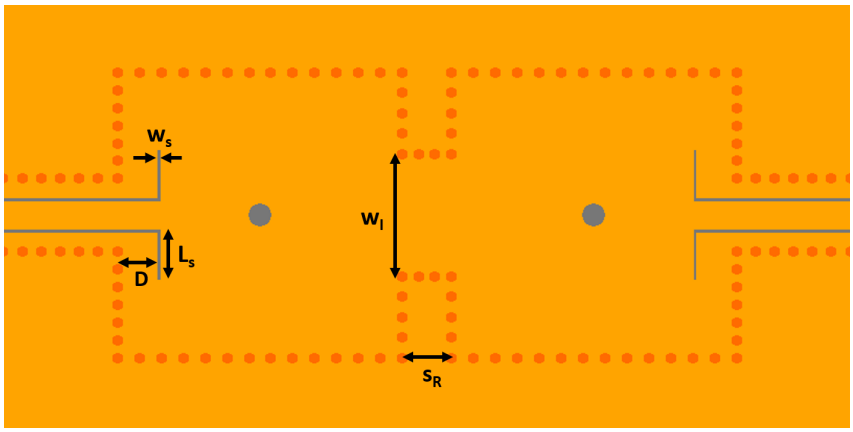

Figure 3.5: Proposed evanescent-mode SIW filter topology with coupling structures and labeled geometry parameter names.

The proposed geometry of the different coupling mechanisms for the design are shown in Fig. 3.5. The GCPW end slots that dictate the external coupling into the resonators is parameterized by the variables W_s, L_s, and D, and the inductive irises that dictate the inter-resonator coupling is parameterized by the variables W_I and S_R. In this design, static inter-resonator coupling and external coupling mechanisms are used. As a result, as the resonators are tuned to different frequencies, the effective electrical size of these physically static coupling structures will change relative to the wavelength of the fields. If the design is optimized for the center of the frequency tuning band, at lower frequencies, the larger wavelength will mean

the structures will appear smaller and become under-coupled. The inverse is true at higher frequencies where the smaller wavelength will mean the structure will appear larger and the external coupling will over-couple.

A fully reconfigurable design that is capable of variable inter-resonator and external coupling will be presented in Chapter 4. With the geometry established, a desired response must be selected to calculate the necessary coupling parameters. The coupling structures must then be characterized and tuned to the necessary parameters needed to achieve the desired filter response. A $0.1\,\mathrm{dB}$-ripple 1% fractional-bandwidth Chebyshev second-order response was selected for the design at $4.8\,\mathrm{GHz}$ at the center of the tuning band.

Using known Chebyshev synthesis methods [57], the g-coefficients for the specified response can be found to be

$$g_0 = 1 \quad g_1 = 0.8430 \quad g_2 = 0.6220 \quad g_3 = 1.3554. \tag{3.6}$$

From these g-coefficients the necessary coupling parameters to achieve this response can easily be calculated from Eq. 3.2, 3.3, and 3.4. The resulting values for Q_{ext} and k_{12} can then be found as

$$Q_{ext1} = 84.3 \quad k_{12} = 0.0138 \quad Q_{ext2} = 84.3 \tag{3.7}$$

for the specified second-order response.

3.3 External Coupling Design

In Section 2.6, the external coupling was set to be weakly coupled such that Q_{ext} would be sufficiently large for the extraction of the unloaded quality factor of

the resonator. For a filter design, the first and last resonators need to be externally coupled enough so that the fields from the GPCW lines strongly excite the resonator fields. This external coupling needs to be higher than the strongly coupled resonator design since enough energy must couple into the outer resonators so that it can propagate through the rest of the filter.

For the extraction of the external quality factor to a resonator, it has been demonstrated that it can be found from a singly loaded resonator with the other side of the resonator shorted. For a singly loaded resonator, the phase of the reflection S_{11} from the port is related to the external quality factor by

$$Q_{ext} = \frac{f_0}{f_b - f_a} \tag{3.8}$$

where f_0 is the center frequency of the resonator when the phase $\angle S_{11} = 0$, f_b is when $\angle S_{11} = +90°$, and f_a is when $\angle S_{11} = -90°$, which is illustrated in Fig. 3.6.

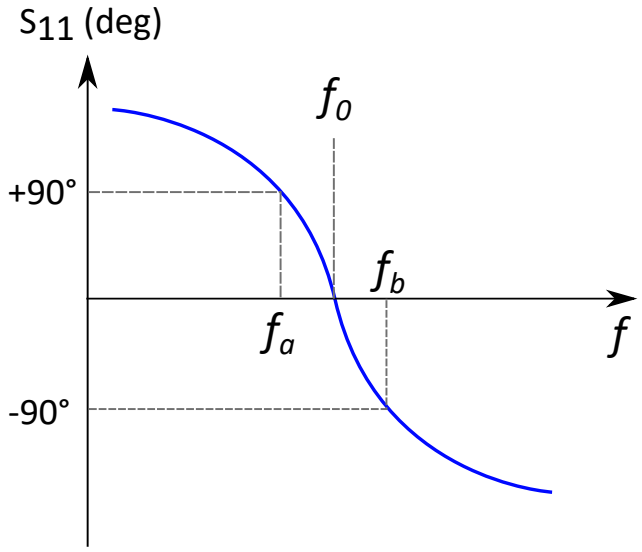

Figure 3.6: Extraction of external coupling from a single port shorted resonator through variation of the phase of the reflection S_{11}

An alternative approach to calculating the external quality factor is by using the

maximum of the group delay response from the reflection S_{11} [59] through

$$Q_{ext} = \frac{\pi f_0 \tau_{S_{11}}(f_0)}{2}, \tag{3.9}$$

where $\tau_{S_{11}}(f_0)$ is the maximum peak of the S_{11} group delay, and f_0 is the resonant frequency where this maximum occurs. The group delay is defined as

$$\tau_{S_{11}}(f_0) = -\frac{\partial(\angle S_{11})}{\partial f}\bigg|_{f=f_0}. \tag{3.10}$$

This second approach is illustrated in Fig. 3.7.

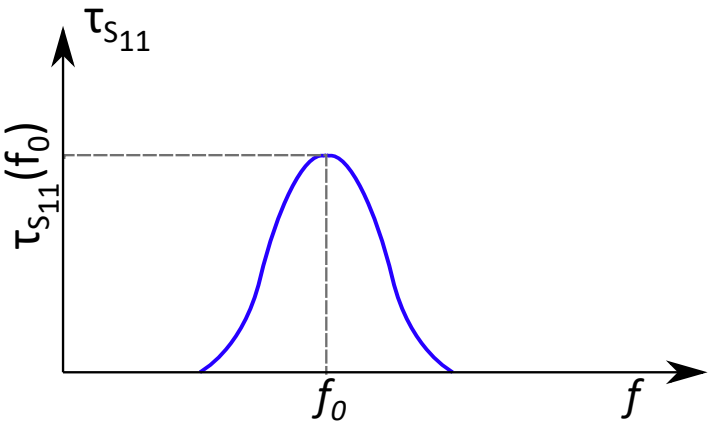

Figure 3.7: Extraction of external coupling from a single port shorted resonator from the peak of the group delay of the reflection S_{11}

In early microwave filter design, many variations of the design were fabricated and tested to extract the coupling parameters from the measured data. These parameters would then be plotted against design curves that would allow for more precise choice of the needed coupling and response specifications. With modern finite element solvers like ANSYS HFSS, this step can be done through simulation. Using the resonator from Chapter 2, a single port fed resonator is modeled as shown in Fig. 3.8. Note that instead of straight feed lines that extend into the cavity as was

used for the strongly coupled resonator in Chapter 2, the ends of the GCPW line are angled outward at a 90° angle to form coupling slots from the end of the GCPW line. This is to provide stronger magnetic coupling into the resonator fields since straight feed lines do not provide strong enough coupling needed for this design.

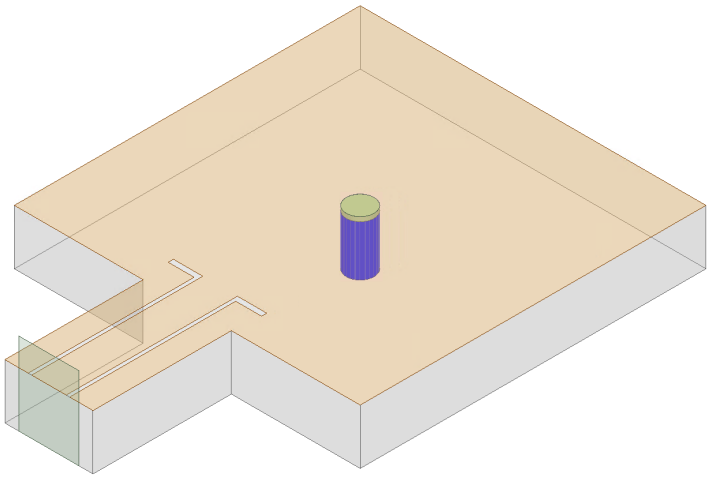

Figure 3.8: HFSS model of the singly loaded resonator design for Q_{ext} extraction of the GCPW wing coupling mechanism.

The Q_{ext} is determined by the width of the slots W_s, the length of the slots L_s, and the depth that the feed lines are inserted into the cavity D as described earlier in Fig. 3.5. These dimensions were varied and the Q_{ext} was extracted using the reflection phase and group delay methods. As mentioned earlier, since the coupling is frequency dependent, the coupling parameter will be different at resonant frequencies so all Q_{ext} extraction is done at $4.8\,\mathrm{GHz}$. The relationship between the external quality factor Q_{ext} as a function of the width of the slots W_s for different feed line insertions D and fixed L_s is plotted in Fig. 3.9. It can be seen that the length of the slots L_s decrease the Q_{ext}, indicating stronger coupling into the cavity. The length of the slots L_s has a greater nonlinear effect on the external coupling than W_s so most of the tuning was done through L_s. Setting the slot width W_s and slot insertion

into the cavity D early on in the design and using the slot length L_s for fine-tuning to the final Q_{ext} value resulted in the dimensions reported in Table 3.1. For a more detailed analysis of this iris coupling structure, refer to [54]. With the external coupling established, the inter-resonator coupling structure can be designed.

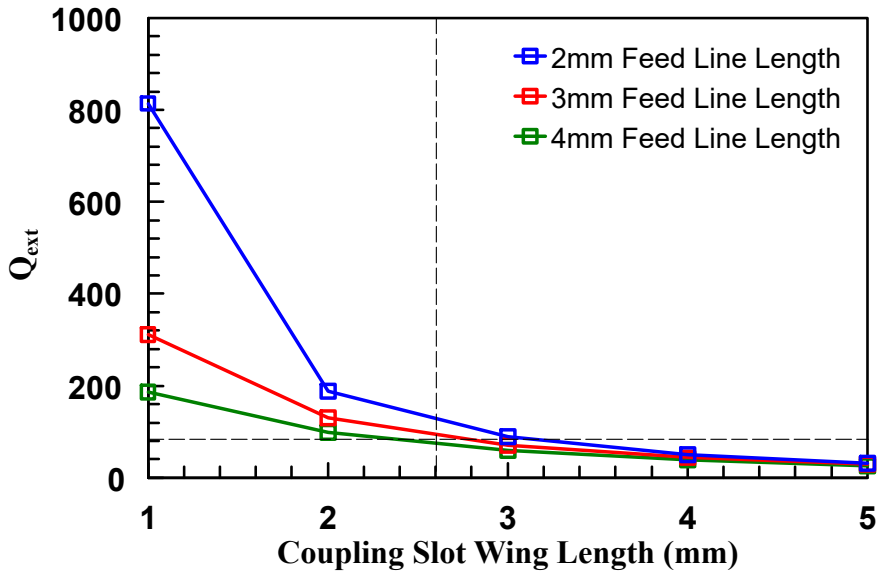

Figure 3.9: Q_{ext} as a function of different length of the coupling slots L_s for different feed line inserted length into the cavity D. Vertical and horizontal dotted lines are included on the figure to indicate the final Q_{ext} and L_s of the filter design.

Table 3.1: External coupling design parameters for the tunable second-order filter.

Design parameters	**Value**
Slot length (L_s)	$2.6\,\mathrm{mm}$
Slot width (W_s)	$0.3\,\mathrm{mm}$
Feed line depth (D)	$3\,\mathrm{mm}$

3.4 Inter-resonator Coupling Design

To extract the inter-resonator coupling between two synchronously tuned resonators, the even and odd modes of two coupled resonators can be used. When two

resonators are either electrically or magnetically coupled into each other, the stored energy in each resonator changes at two different even and odd mode frequencies resulting in a split-pole effect. The even mode occurs when two resonators are in phase, and the odd mode occurs when the resonance of the two are 180° out of phase. Field plots of the phase difference between the two modes can be seen in Fig. 3.10.

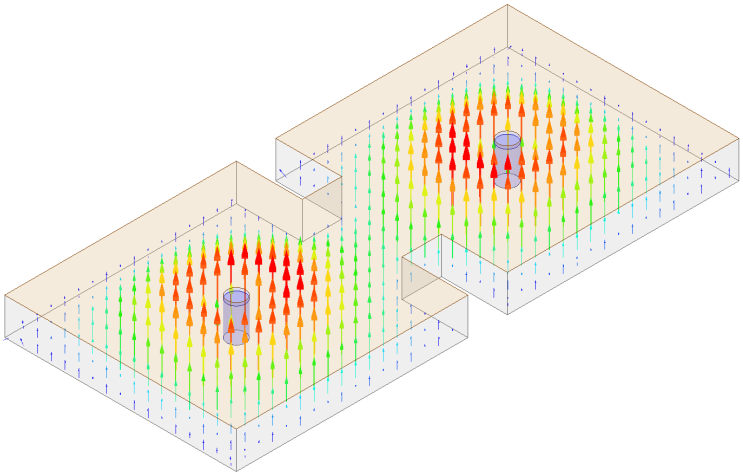

(a)

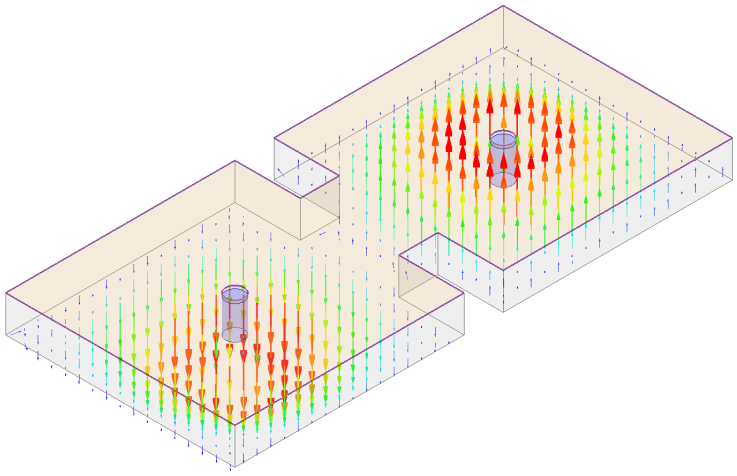

(b)

Figure 3.10: Vector E-field plots of the a) even mode and b) odd mode resonances of two coupled resonators.

For the case of inductive coupling, the resonant frequency is increased when the coupling effect reduces the stored magnetic flux in one resonator. This happens when the resonance mode of both cavities are in phase with each other such that there is an effective electric wall between the two. This is called an even mode resonance, and it reduces the overall inductance of each resonator according to

$$f_e = \frac{1}{2\pi\sqrt{(L - L_m)C}} \tag{3.11}$$

where L and C are the original inductance and capacitance of the individual resonators, and L_m is the mutual inductance, or amount of magnetic coupling between the resonators. For the state when both cavities are 180° out of phase with each other, a perfect magnetic wall exists at the symmetry plane that increases the stored magnetic flux between the two resonators. This shifts the resonant frequency downwards and creates an odd mode resonance according to

$$f_o = \frac{1}{2\pi\sqrt{(L + L_m)C}}. \tag{3.12}$$

From this, the magnetic coupling coefficient between the two cavities can be understood as

$$k_M = \frac{{f_e}^2 - {f_m}^2}{{f_e}^2 + {f_m}^2} = \frac{L_m}{L}. \tag{3.13}$$

The magnetic coupling coefficient then is understood as the ratio of the coupled magnetic energy to the stored energy of the individual uncoupled resonators.

A similar analysis can be done for capacitive coupling. When the two resonators are in phase with each other creating an even mode resonance, the capacitive effects at the coupling interface increases the stored electric energy in each individual resonator. This increased capacitance results in a decreased even mode resonant

frequency

$$f_e = \frac{1}{2\pi\sqrt{(L(C + C_m)}} \tag{3.14}$$

where C_m is the mutual capacitance, or increased stored electrical flux between the resonators. The opposite effect occurs when the resonators are 180° out of phase with each other such that the electric fields from the two sides cancel out at the coupling interface. This decreases the stored electrical energy in both resonators resulting in a frequency increase for odd mode resonances

$$f_o = \frac{1}{2\pi\sqrt{(L(C - C_m)}}. \tag{3.15}$$

Similar to magnetic coupling, the electric coupling coefficient is defined as

$$k_E = \frac{{f_o}^2 - {f_e}^2}{{f_o}^2 + {f_e}^2} = \frac{C_m}{C} \tag{3.16}$$

which is the ratio of the coupled electric energy to the stored energy of the uncoupled resonators.

When there is mixed electric and magnetic coupling, the two coupling mechanisms exist in parallel to each other such that the even and odd mode resonances become

$$f_e = \frac{1}{2\pi\sqrt{(L - L_m)(C - C_m)}} \tag{3.17}$$

$$f_m = \frac{1}{2\pi\sqrt{(L + L_m)(C + C_m)}}. \tag{3.18}$$

In the case of mixed electric and magnetic coupling, the effect on the resonant shift direction will be the same between the two couplings such that the two add together

increasing the overall coupling. The mixed coupling can then be found as

$$k_X = \frac{{f_e}^2 - {f_m}^2}{{f_e}^2 + {f_m}^2} = \frac{CL_m + LC_m}{LC + L_mC_m}. \tag{3.19}$$

Since the $L_mC_m << LC$, the mixed coupling k_X can be simplified further as

$$k_X \cong \frac{L_m}{L} + \frac{C_m}{C} = k_M + k_E \tag{3.20}$$

which is the superposition of the magnetic coupling and electric coupling mechanisms. The sign of the coupling coefficient is not important for simple filter synthesis designs that do not employ cross-coupling so only the magnitude of the coupling coefficient is extracted in this work as

$$k = \frac{f_{p2}^2 - f_{p1}^2}{f_{p2}^2 + f_{p1}^2} \tag{3.21}$$

where f_{p2} is the higher resonant frequency and f_{p1} is the lower resonant frequency without attention to the mode type of the resonators. More detailed analysis and circuit models for the derivation of these coupling coefficients can be found in Chapter 8 from [60].

When the resonators are weakly externally coupled, the even and odd mode resonances of the filter can be seen as two split peaks, which can be used to calculate the coupling coefficient k from Eq. 3.21. For accurate extraction, it recommended that the amplitude of the two peaks is kept below $-20\,\mathrm{dB}$ and the null between the two peaks should be at least $-30\,\mathrm{dB}$ down. This method is illustrated in Fig. 3.11(a). The weaker the external coupling, the deeper this null between the two peaks will become but also decreasing the overall height of the two peaks such that measurement or simulation convergence may become difficult. For simulation,

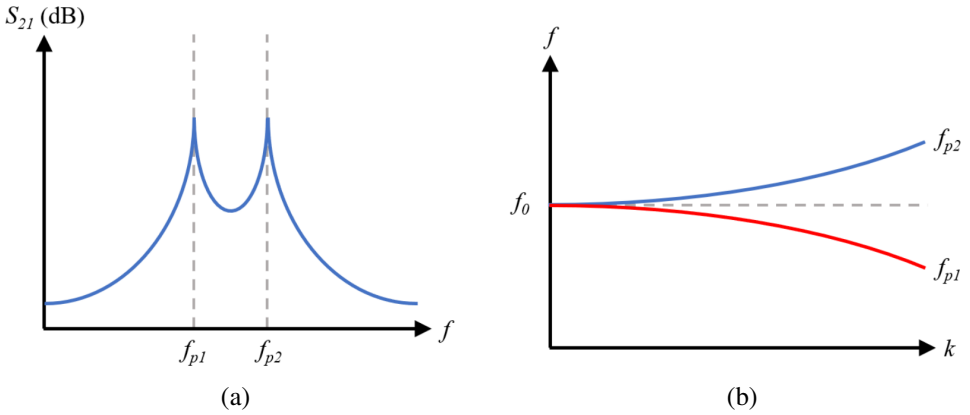

Figure 3.11: Coupling coefficient extraction method from a) the S_{21} response of two resonators with weak external coupling and b) the splitting of the even and odd poles as a function of coupling which can be found through an Eigenmode simulation (from [54]).

a Driven Modal analysis can be done with weak external coupling, but while more accurate this method is slow since it requires solving the full EM effects of the structure over a range of frequencies. A faster Eigenmode simulation can be done which will solve for the resonant even and odd modes of two coupled resonators such that the coupling coefficient can be directly analyzed as illustrated by Fig. 3.11(b).

The Eigenmode HFSS model used to extract the coupling coefficient from the inductive iris is shown in Fig. 3.12. The coupling coefficient k as a function of the coupling iris width W_I for different spacings between the resonators S_R (as defined by Fig. 3.5) is simulated and plotted in Fig. 3.13. The wider iris width causes more magnetic coupling between the resonators while increased resonator spacing decreases the magnetic coupling. Optimizing for the necessary design k_{12}, the final dimensions arrived at are shown in Table 3.2.

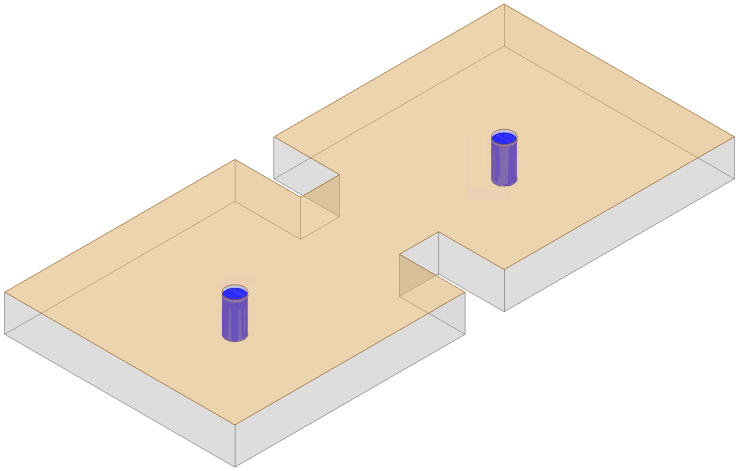

Figure 3.12: Eigenmode HFSS model of the two evanescent-mode resonators inductively coupled together with an open rectangular iris.

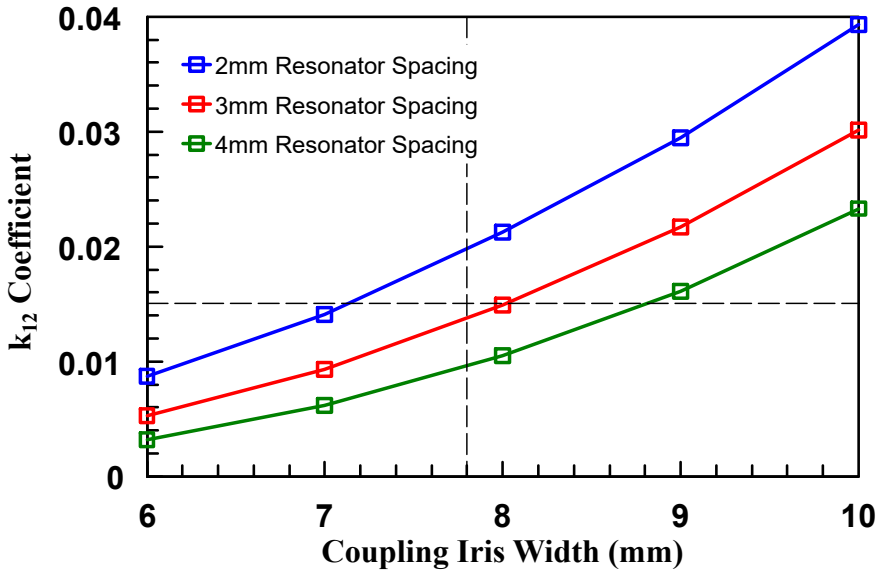

Figure 3.13: k_{12} as a function of different coupling iris width W_I for different spacings between the resonators S_R. Vertical and horizontal dotted lines are included on the figure to indicate the final k_{12} and W_I of the filter design.

Table 3.2: Inter-resonator coupling design parameters for the tunable second-order filter.

Design parameters	**Value**
Resonator spacing (S_R)	$3.4\,\mathrm{mm}$
Iris width (W_I)	$7.8\,\mathrm{mm}$

3.5 Fabrication

Since there were no major fabrication issues with the resonator design, the process from Section 2.5 was used to fabricate this second-order filter design. Plated vias were drilled with the LPKF ProtoMat S103, electroless copper plated, and then copper electroplated. Air gaps were drilled with the LPKF ProtoMat S103, and the precise depth drilled tuning post below the copper diaphragm was milled with the T-Tech Quick Circuit J5. The GCPW trenches were then taken back to the LPKF ProtoMat S103 to be milled. The design was finally routed out, and Plexiglass interfaces with epoxied Teflon tubes at the liquid metal tuning via locations were clamped to the top and bottom of the device. The resulting device can be seen in Fig. 3.14, and the dimensions of the final design is recorded in Fig. 3.15.

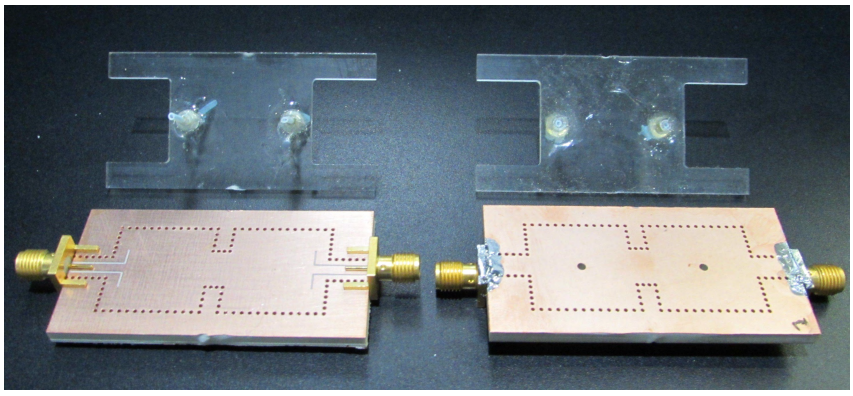

Figure 3.14: Fabricated second-order evanescent-mode liquid metal continuously tunable filter. The left device is a view of the top of the design, and the right device is a bottom view of the same design. The Plexiglass interfaces with Teflon tubes are seen sitting next to the device.

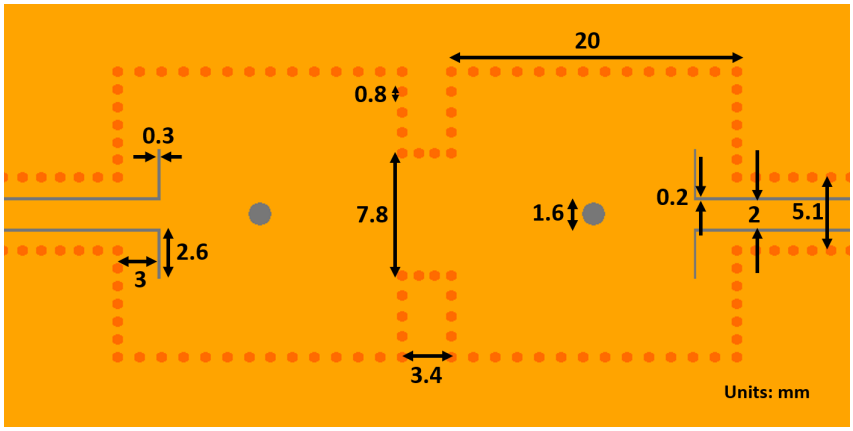

Figure 3.15: Dimensions of the final second-order evanescent-mode liquid metal continuously tunable filter design.

3.6 Measurements and Results

The two tuning vias of the fabricated design were manually injected with Galinstan to bring the poles of each resonator to the same resonant frequency. When the two poles are aligned, the second-order filter responses can be measured at different tuned center frequency states as shown in Fig. 3.16. For the lower frequency states, the bandwidth of the filter is narrower than the higher frequency states, as explained earlier in the chapter since the inter-resonator and external coupling structures are static and frequency-dependent so constant bandwidth and response cannot be realized. A 0.1-dB ripple Chebyshev response with a fractional bandwidth of 2% can still be observed at $4.8\,\mathrm{GHz}$ which indicates that the coupling structures are behaving as designed. Second-order responses were measured from $3.4\,\mathrm{GHz}$ to $5.7\,\mathrm{GHz}$, which measures lower in frequency than the safe designed lower bound of $3.8\,\mathrm{GHz}$. The highest frequency of $5.7\,\mathrm{GHz}$ is the unloaded state of both liquid metal posts, and it is lower than the original unloaded frequency of $5.9\,\mathrm{GHz}$ for the unloaded single resonator design. This is caused by the coupling structures increasing the effective size of each resonator, which shifts the resonant frequency down.

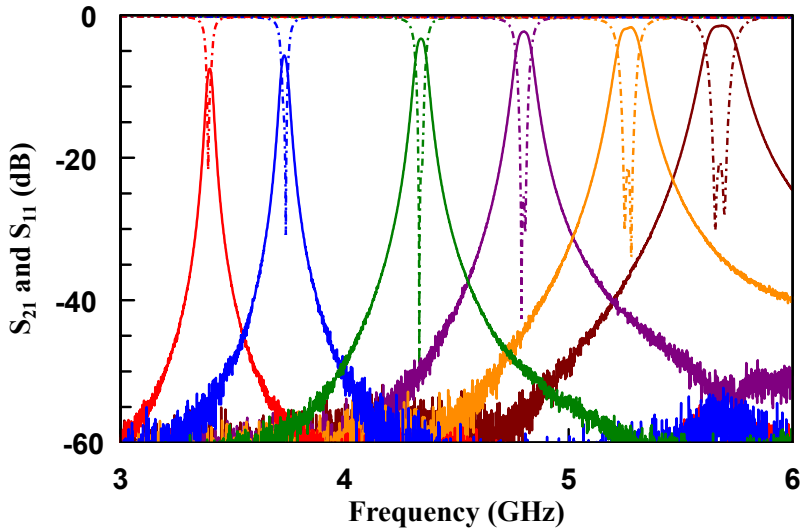

Figure 3.16: Measured S_{21} (solid trace) and S_{11} (dotted trace) of the fabricated second-order filter design at six different tuning states indicated by the different trace colors.

Three of the measured results at $3.7\,\mathrm{GHz}$, $4.8\,\mathrm{GHz}$, and $5.7\,\mathrm{GHz}$ are plotted against the simulated results in Fig. 3.17 and show strong agreement between simulation and measurement across the tuning range of the filter. This is further demonstrated in Fig. 3.18 which compares simulated and measured results of the insertion loss and bandwidth of the second-order filter response at different resonant frequencies. The bandwidth traces closely follow the same trend indicating that the external and inter-resonator coupling structures behave as expected through different tuning states of the filter. The measured insertion loss results are higher at lower frequencies, but this is expected due to the increased losses of the filter at strongly capacitively loaded states. This agrees with the lower quality factors observed from the resonator design of Chapter 2 from the oxidation of the Galinstan post.

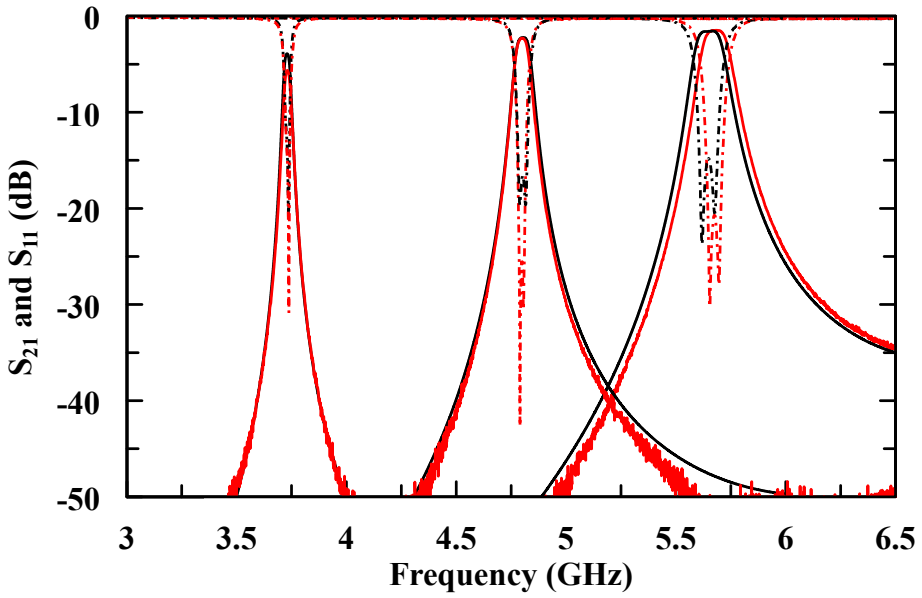

Figure 3.17: Measured S_{21} (solid trace) and S_{11} (dotted trace) of the fabricated second-order filter design are displayed in red. The simulated response of the design is overlaid in black.

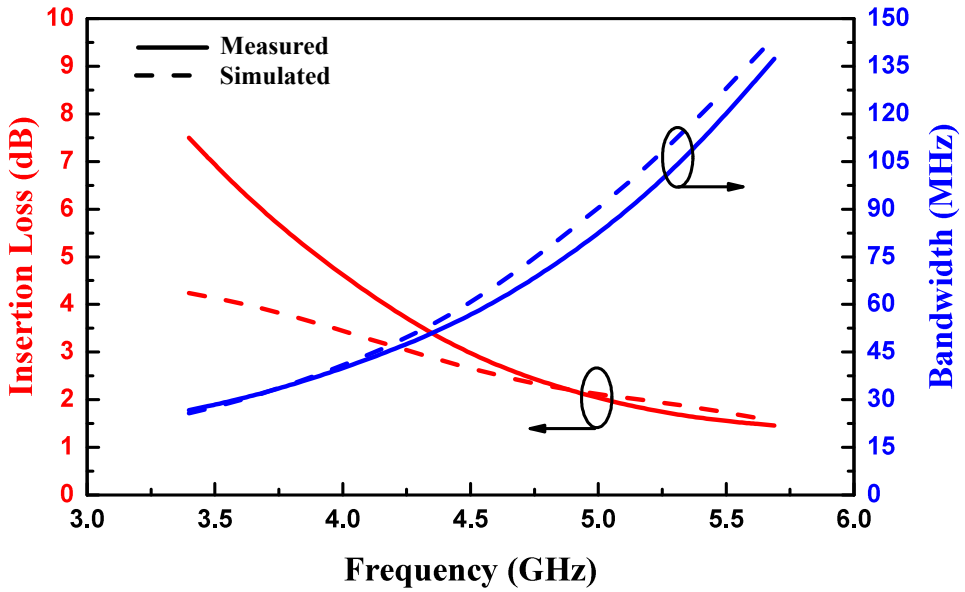

Figure 3.18: Comparison of simulated and measured results of the filter insertion loss and bandwidth over frequency.

3.7 Summary

The evanescent-mode SIW resonators from Chapter 2 were successfully integrated into a second-order bandpass filter design that employed the same Galinstan continuous tuning mechanism. The resonators coupled together the second-order bandpass filter design with external coupling slots at the end of the GCPW feed lines and with an open square inductive iris for the inter-resonator coupling. Second-order responses were recorded from $3.4\,\mathrm{GHz}$ to $5.7\,\mathrm{GHz}$ with varying bandwidth across the tuning range due to the static inter-resonator coupling and external coupling. The designed $0.1\,\mathrm{dB}$-ripple Chebyshev 2% fractional-bandwidth second-order response was realized at $4.8\,\mathrm{GHz}$. The measured response bandwidth closely matches simulation with additional insertion loss at highly loaded capacitive frequency compared to simulation due to oxidation effects. The continuous liquid metal tuning design was demonstrated to be effective in a complete filter design, and is a promising mechanism for future advanced reconfigurability applications. After proving the frequency tunability of liquid metal tuning, Chapter 4 will develop mechanisms for variable external and inter-resonator coupling for full reconfigurability of the filter response.

Chapter 4

Fully Reconfigurable Filter Design

In order to meet the stringent filter demands of future systems, filter bandwidth and shape tunability is desirable. The frequency-tunable design of Chapter 3 will be expanded to included liquid metal tunable coupling structures that allow for a fully reconfigurable filter design. The proposed tunable coupling structures will be studied and characterized to design a reconfigurable filter with a wide tuning range of filter responses. This fully reconfigurable design will be simulated, and the fabrication and measurement procedure for the device will be explained. The measured results will experimentally validate this fully reconfigurable design and the promising advanced reconfigurability of liquid metal tuning.

4.1 Fully Reconfigurable Filter Theory

It was discussed in Chapter 3 that from coupled resonator theory, the resonant frequency of synchronously-tuned resonators controls the center frequency of the filter passband, and the inter-resonator and external coupling control the bandwidth and shape of the filter response. Coupling theory was presented in Chapter 3, and Eq. 3.20 stated that the magnetic and electric coupling coefficients will add together for the overall mixed coupling, provided that the two couplings are in phase with

each other. In other words, the two coupling mechanisms acting in parallel results in a summation of the two coupling coefficients. This same concept can be extended to multiple parallel mechanisms being added together and a similar analysis as that from Chapter 8 of [60] can be done to conclude that

$$k_X \cong k_{M1} + k_{M2} + \ldots + k_{E1} + k_{E2} + \ldots \tag{4.1}$$

when multiple magnetic or electric coupling mechanisms are acting together.

In this chapter, the continuously tunable capacitive-loading post using liquid metal design will be incorporated into a device that provides control of the external coupling and inter-resonator coupling. For the external coupling, this is done with capacitive-loading posts below the GCPW feed lines that will act in addition to the GCPW slots from Chapter 3. For the inter-resonator coupling, five vias in the iris that can be shorted provide discrete control over the effect iris size while also being capable of continuous capacitive loading that forms a resonant iris that can increase the magnetic coupling between the cavities. These two mechanisms provide continuous tuning of both coupling mechanisms and allows for the realization of a wide range of possible filter responses with varying bandwidth, ripple, and center frequency.

The resulting equivalent circuit of the fully reconfigurable filter is illustrated in Fig. 4.1 with all variable components being implemented using Galinstan-actuated capacitive posts. By using the same mechanism, it allows for future automation and control circuitry around the design to be simpler since it does not need to incorporate multiple different types of tuning mechanisms as in [6] where both piezoelectric and varactor tuning mechanisms are used. In addition, this mixed inductive and tunable capacitive loading mechanisms has the potential for higher power handling and

lower losses than other fully reconfigurable designs. This mechanism is unique and has not been used in the past since other tuning technologies are not able to create practical capacitive loading posts that can go from a fully unloaded to loaded state, which provides a wider range to tune these coupling mechanisms over compared to piezoelectric actuator designs.

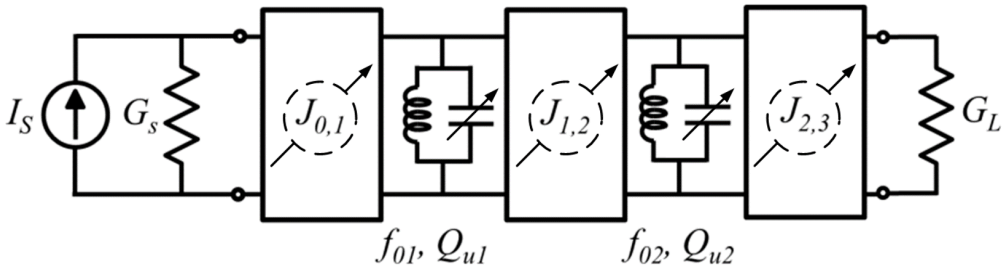

Figure 4.1: Equivalent circuit representation of the fully reconfigurable filter design with variable J-inverters for the external and inter-resonator coupling tuning as well as variable shunt capacitors for resonator tuning.

4.2 External Coupling Tuning Mechanism

The external coupling mechanism of angled slots at the end of the GCPW line from Chapter 3 provides inductive coupling into the cavities. Changing the length and location of these slots through liquid metal channels in a Plexiglass interface has been presented before in [21] to control the amount of inductive external coupling into the resonator. This requires the design of multiple planar slots on the top of the filter and only allowed for discrete state configurations. A modified continuous design where the slot lengths are continuously controlled would add significant complexity to the design since two different tuning mechanisms would be needed: 1) vertical control the liquid metal in each tunable post 2) horizontal control of the liquid metal in planar channels.

Instead, static GCPW feed slots are designed that couple magnetically into the cavity as in Chapter 3, and a tunable capacitive loading post is placed at the end of the resonator below the GCPW signal line. The capacitive loading post, which is connected to ground, provides a current return path for part of the current from the GCPW signal line. This current path generates a magnetic field around the loading post that couples into the fields of the cavity resonator. When the capacitive air gap is decreased, the impedance of this current path decreases, allowing for more current to flow along the post. This results in a stronger magnetic field strength near the edge of the cavity for the heavily loaded via which can be seen in Fig. 4.2. Both the inductive slot and the loading post mechanism provide magnetic field coupling that add together in phase as described by Eq. 4.1. The static inductive slots dictate a minimum amount of external coupling which can then be increased by more heavily loading the external tuning post.

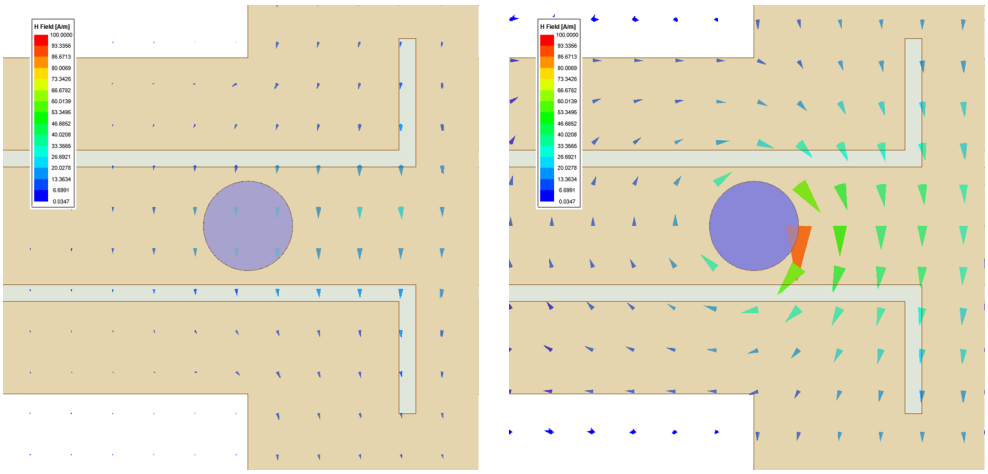

(a) (b)

Figure 4.2: Magnetic field vector plots of the external coupling mechanism when a) the via is empty of liquid metal and b) when the via is loaded to an air gap of 4 mil. The H-field plots have the same magnitude scales for direct comparison of the field strengths. The H-field can be seen to be stronger in the cavity for the heavily loaded via.

Driven Modal analysis simulations in HFSS were done on the design shown in Fig. 4.3. The same phase response and group delay Q_{ext} extraction technique used in Chapter 3 were used for this new design to optimize the dimensions of the inductive slots and the location and size of the external coupling tuning via. The final design resulted in the placement of a single $1.6\,\mathrm{mm}$ via at the interface between the GCPW and the edge of the resonator, and the extracted Q_{ext} tuning for different air gaps of the external Q via is plotted in Fig. 4.4. It can be seen that the external quality factor decreases for smaller external tuning via air gaps since the reduced impedance of the return current path leads to stronger magnetic coupling into the cavity as explained.

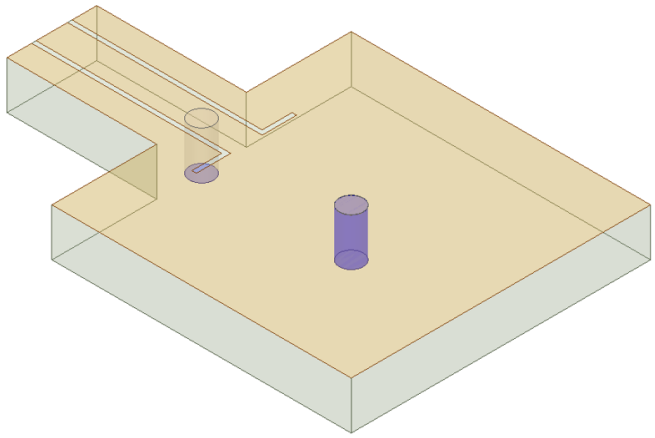

Figure 4.3: Driven Modal HFSS model of a singly loaded resonator with a resonator capacitive-tuning via and an external-coupling capacitive-tuning via.

The inductive slots from the GCPW dictates then the minimum amount of external coupling from the cavity, thereby the maximum Q_{ext} value. From Eq. 3.2, it can be seen that the maximum achievable value of Q_{ext} dictates the minimum achievable fractional bandwidth of the design. Because the coupling structures are

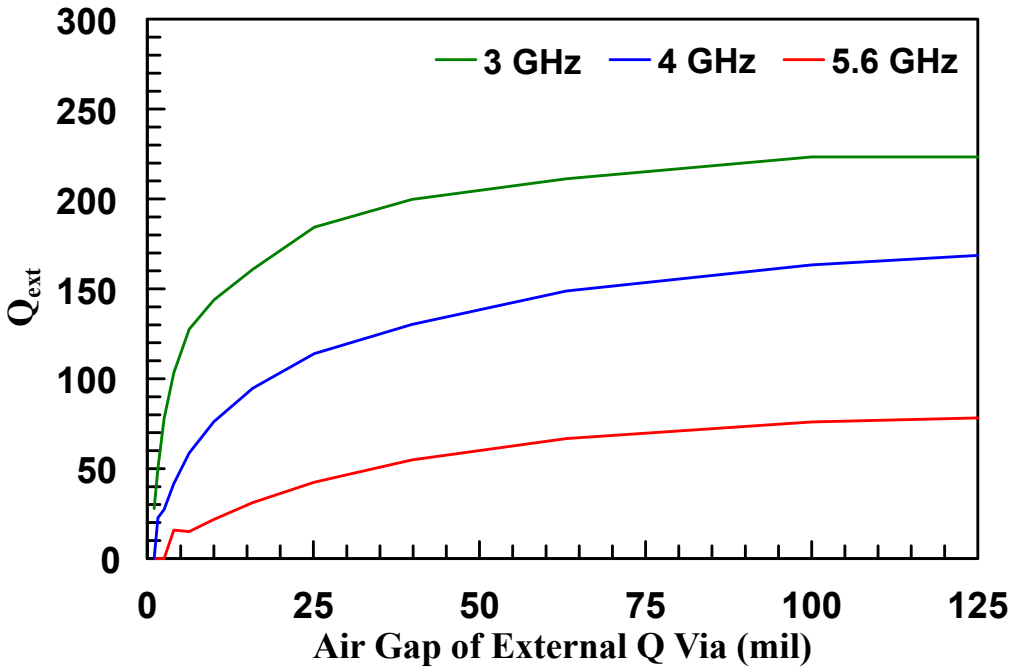

Figure 4.4: External quality factor Q_{ext} as a function of the capacitive air gap for the external coupling via. Three curves for different center frequencies are plotted.

frequency-dependent such that there is more coupling at higher frequencies, when the center frequency is at the highest end of the frequency band, it will have the lowest untuned Q_{ext} value. This can be seen by observing the $5.6\,\mathrm{GHz}$ trace in Fig. 4.4 which is the highest frequency when the resonator tuning vias are unloaded (this is lower than the $5.8\,\mathrm{GHz}$ seen in earlier chapters since the different coupling structures shifted the center frequency of the resonators downward slightly). The minimum achievable bandwidth when the resonators are unloaded needs to be designed and set at $5.6\,\mathrm{GHz}$. The lower bound was selected then to be a 2% fractional bandwidth Butterworth response, which corresponds to a Q_{ext} value of 70.71. The inductive slot dimensions of W_s, L_s, and D were then redesigned to meet this Q_{ext} at $5.6\,\mathrm{GHz}$. The resulting dimensions are listed in Table 4.1.

Table 4.1: External coupling design parameters for the fully reconfigurable second-order filter.

Design parameters	**Value**
Slot length (L_s)	$2\,\mathrm{mm}$
Slot width (W_s)	$0.3\,\mathrm{mm}$
Feed line depth (D)	$3\,\mathrm{mm}$

4.3 Inter-resonator Coupling Tuning Mechanism

For the inter-resonator coupling control, five tuning vias are placed in a large inductive iris that connects the two resonators. An Eigenmode HFSS model of the proposed design is shown in Fig. 4.5. Each iris tuning via can be used as either one of two mechanisms: 1) a shorted inductive post or 2) a capacitive loading post. If a via is completely filled with liquid metal, it reduces the effective size of the inductive iris and thereby reduces the magnetic coupling between the two resonators by discrete state changes. If a via is partially filled with liquid metal, it creates capacitive loading within the iris which causes the iris to exist in a resonant state that shifts the odd mode resonance of the two cavities to shift down in frequency. These two mechanisms can be used together to allow for tuning of the inter-resonator coupling by using shorted inductive posts for large coupling changes and capacitive loading posts for finer coupling control. These two mechanisms together can realize a continuous range of k_{12} values, but this tuning is discontinuous since different shorted inductive posts are used for large discrete coupling changes and the capacitive loading of partial posts provides a limited narrow range of continuous tuning.

The shorted inductive posts allow for large discrete changes in the inter-resonator coupling, and the order and configuration of these posts as well as the number of inductive post has an effect on the inter-resonator coupling. Fig. 4.6 plots the change

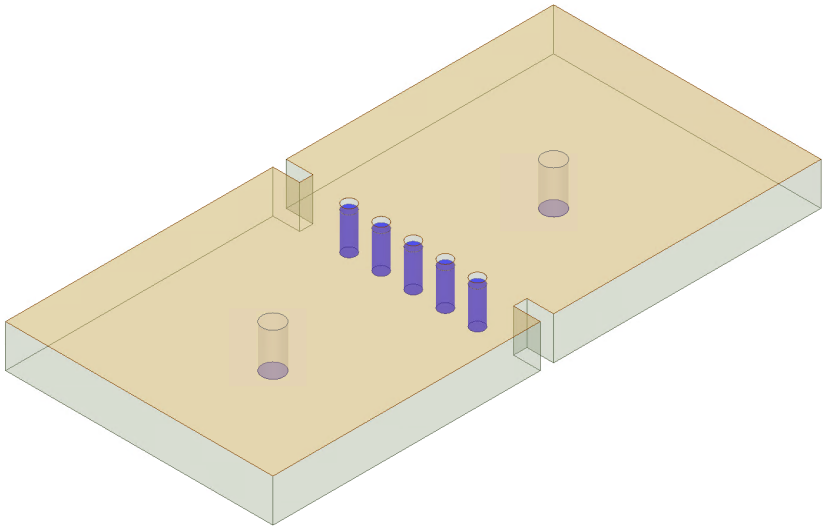

Figure 4.5: Eigenmode HFSS model of the five via iris design that is able to meet the desired inter-resonator coupling tunability.

in the coupling coefficient k_{12} between the two resonators for some of the different configurations of the inductive posts as a function of the resonant frequency. For simplicity, each state can be thought of as different binary configurations where 0 indicates the via is shorted and 1 indicates the via is unfilled. This convention is used since the full coupling structure state of the iris vias can be thought of as an array of the air gap heights. For example, $[0 \quad 0 \quad 50 \quad 50 \quad 50]$ indicates that posts 1 and 2 have an air gap of 0 mil (shorted) and that posts 3, 4, and 5 have an air gap of 50 mil. Because the same configuration flipped about the center of the iris provides the same magnetic coupling, horizontally flipping the configuration state results in an equivalent configuration. In other words, state 01111 is equivalent to state 11110. It should be noted that the maximum resonant frequency of the entire structure decreases for wider k_{12} values because larger effective irises increase the effective resonator sizes and shift the resonant frequency down.

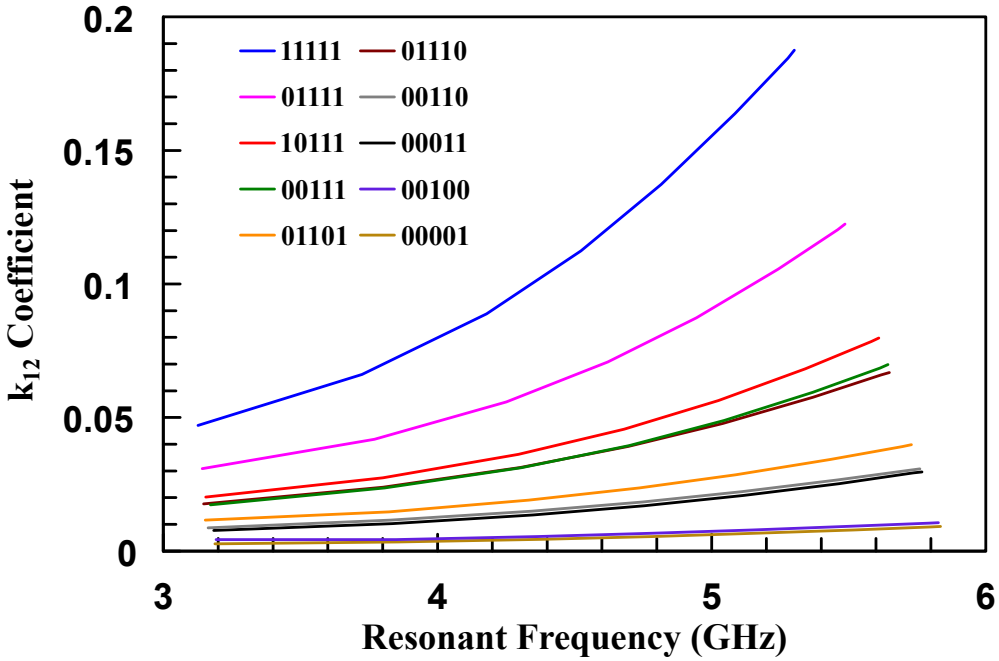

Figure 4.6: k_{12} of the inductive iris as a function of the resonant frequency of the individual resonators for different shorted inductive post configurations. For each configuration, 0 indicates the via is shorted and 1 indicates the via is unfilled.

The coupling coefficient is less at lower frequencies since an inductive iris is electrically smaller at these lower frequencies, which has been discussed in Chapter 3. The largest coupling is realized when no inductive posts exist in the iris (state 11111) to obstruct the magnetic coupling. Note that the configuration of the inductive posts is important since the same number of shorted posts located at different locations does not provide the same amount of coupling. This can be seen by the fact that the second strongest coupling configuration is when the outermost via is shorted for state 01111. The third strongest coupling configuration is when the second outermost via is shorted for state 10111. This is because more magnetic coupling occurs near the center of the iris so placing inductive plots near the center more heavily affects this coupling.

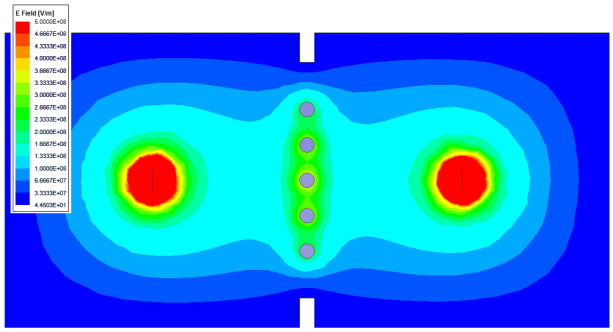

(a)

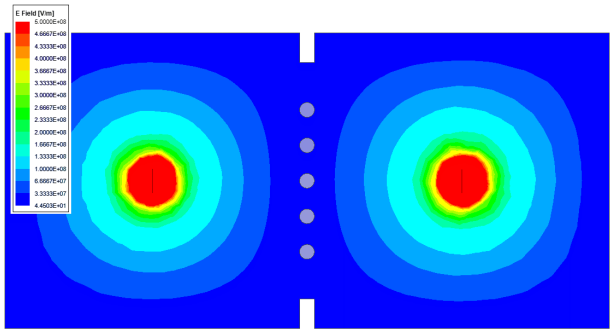

(b)

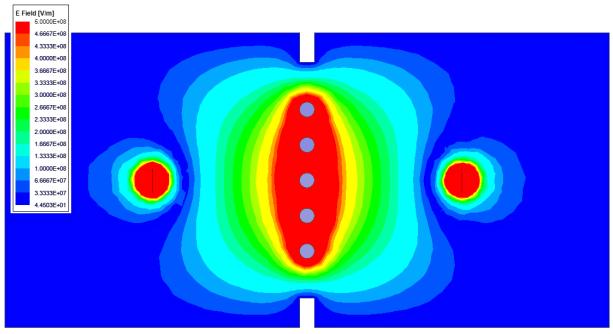

(c)

Figure 4.7: Electric field distributions of the a) lower even mode, b) middle odd mode, and c) iris resonant mode. All five iris tuning posts are capacitively loaded to an air gap of 10 mil, and the two resonators are capacitively loaded to an air gap of 1 mil.

The capacitively loaded posts allow for finer continuous coupling control by allowing for an additional electric coupling mechanism between the two resonators. When the iris contains capacitively loaded posts, it creates a resonant iris which shifts the even mode down in frequency. This is because when the two resonators are in-phase the additional electrical energy from the capacitive loaded posts couples the two resonators more. This does not occur for the odd order mode when the two resonators are out-of-phase and the two are primarily coupled by just magnetic coupling. The distribution of the E-fields can be seen in Fig. 4.7, which show that for the even mode the capacitive loading of the irises allows for more electrical coupling between the two resonators while there is minimal electrical energy in the iris for the odd mode plot. This capacitive loading of the iris also creates an additional third unwanted resonance within the iris which is shifted far down in frequency when the iris is heavily loaded.

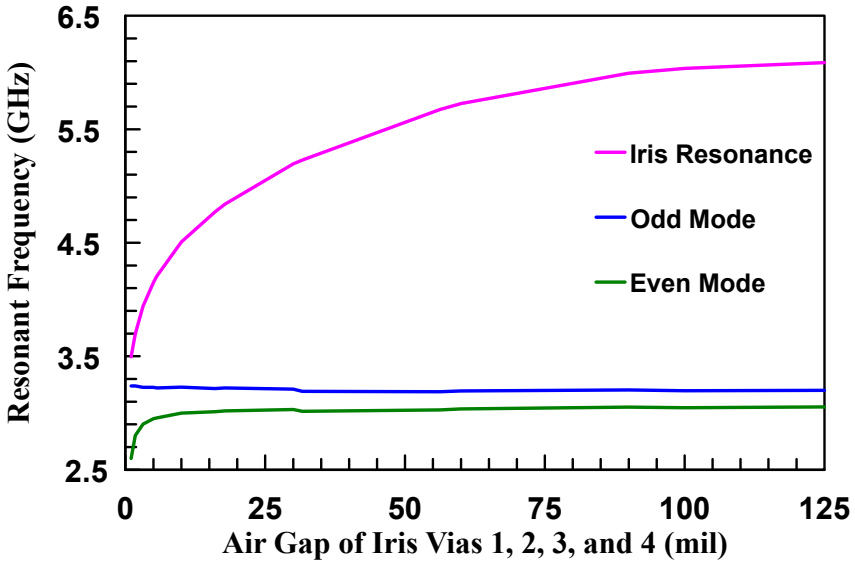

Figure 4.8: Eigenmode solved frequency of each one of the different resonant-iris-coupled modes as a function of different air gaps when all five iris tuning vias are capacitively loaded to the same amount.

Fig. 4.8 shows the resonant frequency of each one of these modes as a function of capacitive air gaps when all five tuning vias are partially filled to the same amount. It can be seen that both the highest frequency and lowest frequency resonances are shifted down in frequency while the middle resonance remains mostly constant in frequency across different capacitive loading states of the iris.

The mechanism of continuous capacitive loading of the iris allows for a range over which continuous bandwidth tuning can be done on the filter response. Full Driven Modal analysis was done using this mechanism to tune a $10\,\mathrm{dB}$ Chebyshev responses at $4.5\,\mathrm{GHz}$ over a continuous range of bandwidths, which is shown in Fig. 4.9. The shorted inductive post configuration was set to be 01111 while the remaining four partially filled vias are capacitively tuned to the same air gap. It can be seen that the bandwidth of the filter response is broadened as this air gap decreases, but with the side effect of the higher-order spurious mode being shifted down in frequency toward the passband.

For the best filter performance the separation between the center passband and this spurious mode should be maximized while achieving the correct k_{12} value necessary to realize the desired bandwidth. Because there are numerous via shorting and capacitive height permutations possible, it is difficult to directly display the data representing the effect of these five inductive vias since there are 5 independent variables. Instead, the trade-off space of possible realizable coupling coefficients k_{12} is plotted against the frequency separation of the spur for different frequencies in Figs. 4.10.

Each scatter plot point represents one of these different permutation of inductive posts as well as allowing all the different capacitive air gaps to individual range from 10 mil to the completely unloaded state of 125 mil. Clusters in the plot correspond to differences in the number of vias being shorted since the shorting of one of the

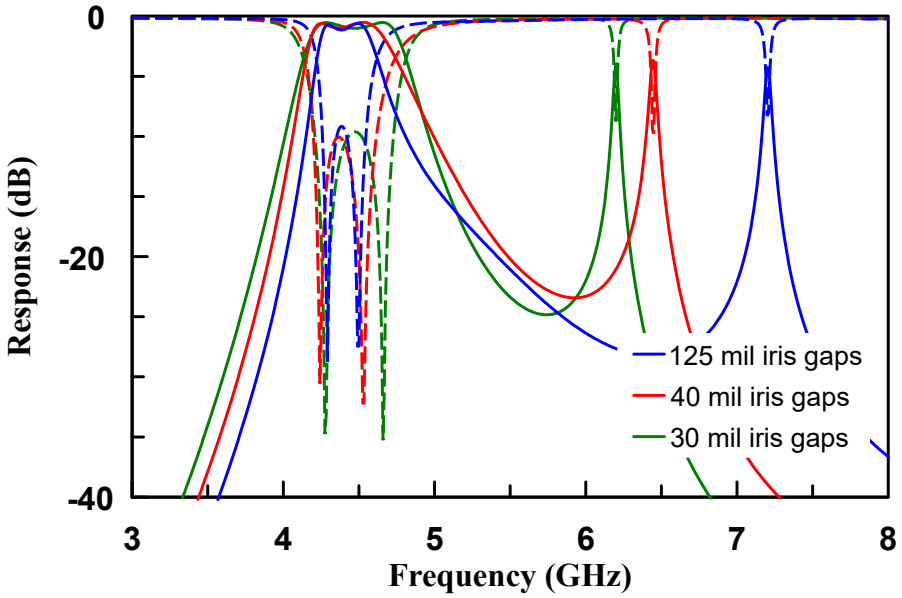

Figure 4.9: Multiple simulated $10\,\mathrm{dB}$ Chebyshev responses at $4.5\,\mathrm{GHz}$ to demonstrate the continuous bandwidth tuning of the capacitive posts and an inductive post configuration of 01111. Each different iris air gap state is plotted in different colors and the solid line represents S_{21} and the dotted line is S_{11}.

vias creates a large change in the amount of inductive coupling between the two resonators. The highest cluster of points for all three plots are all the permutations of the tuning vias only being capacitively loaded with no shorting of the vias, which will always provide the most amount of magnetic coupling. Moving across the x-axis to lower spur separations, the cluster slopes upwards to higher k_{12}. This trend is due to the loading of the iris vias that increases the capacitive coupling but also shifts the spurious mode lower in frequency. The second lower cluster of coupling points below the uppermost cluster corresponds to all the tuning states in which any one of the tuning vias may be shorted. Each decreasing cluster below that consists of all the states where 2, 3, or 4 of the vias are shorted.

It should be noted that for any given k_{12} value there may be multiple different states that realize the same coupling but may have different spur separations. In

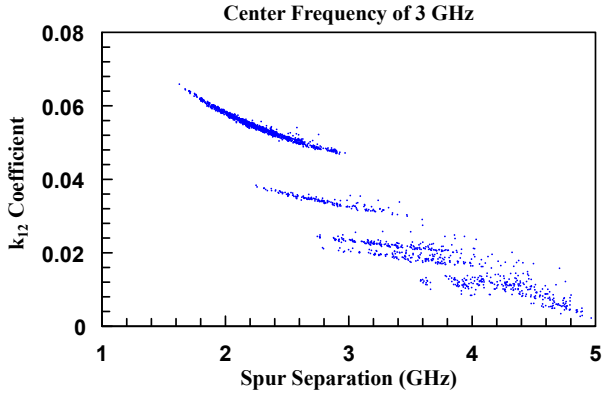

(a)

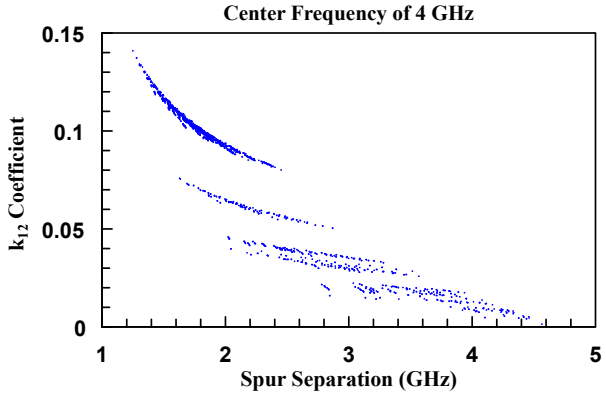

(b)

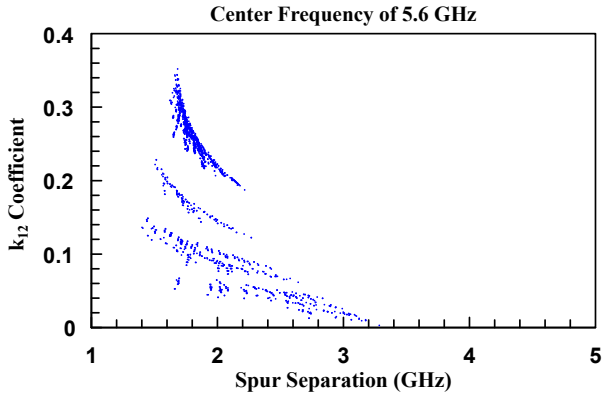

(c)

Figure 4.10: Tradeoff space between k_{12} and the distance of the spurious resonance from the center filter passband at a) $3\,\mathrm{GHz}$, b) $4\,\mathrm{GHz}$, and c) $5.6\,\mathrm{GHz}$.

the tuning of the filter response, the closest k_{12} below the desired amount should be selected through analysis of the shorted inductive post configuration from Fig. 4.6, and then the remaining vias should be partially filled for fine-tuning of the necessary k_{12} value.

The inductive coupling from the size of the iris limits the range of k_{12} values that can be tuned to, and it is lowest at the low end of the center frequency tuning band since the inductive iris is electrically small for large wavelengths. This means that the tuning state at $3\,\mathrm{GHz}$ will be the most limited in the widest bandwidth that can be achieved because it has the least inter-resonator coupling. The maximum achievable bandwidth of the filter was designed such that a Butterworth response with a fractional bandwidth of 7% is realizable throughout the frequency tuning range while maintaining at least $2\,\mathrm{GHz}$ of spur separation. Using

$$\Delta = k_{12}\sqrt{g_1 g_2}, \tag{4.2}$$

it is found that a k_{12} value of 0.05 must be achieved at all frequencies. The dimensions of the iris W_I and S_R from Chapter 3 were tuned to meet this requirement, and the size of the five tuning vias was optimized. The final diameter of the tuning vias ended up being $1\,\mathrm{mm}$ with a pitch spacing of $2.4\,\mathrm{mm}$. All the dimensions of the inter-resonator coupling tuning iris are recorded in Table 4.2.

Table 4.2: Inter-resonator coupling design parameters for the tunable second-order filter.

Design parameters	**Value**
Resonator spacing (S_R)	$3.4\,\mathrm{mm}$
Iris width (W_I)	$7.8\,\mathrm{mm}$
Iris tuning via diameter	$1.0\,\mathrm{mm}$
Iris tuning via pitch spacing	$2.4\,\mathrm{mm}$
Iris edge to outer iris tuning via	$3.2\,\mathrm{mm}$

4.3.1 Wideband Third-Order Responses Using the Iris Resonance

The spurious effect of the iris resonance can be mitigated by tuning it down in frequency near the two primary cavity modes to create a wideband third-order filter response. This response is difficult to physically realize since it requires strong capacitive loading from multiple iris tuning vias and strong external coupling. One simulated example of this tuning state is shown in Fig. 4.11, but it has a large passband ripple of $5\,\mathrm{dB}$ since the current design is not able to provide enough external coupling to reduce the ripple further. The response is realized by putting the iris vias into state 01110, capacitive tuning vias 2, 3, and 4 to a gap of 2.7 mil, and external coupling air gaps of 2.9 mil. Asymmetric permutation states do not provide a clean third-order responses because the iris resonance cannot be brought down low enough in frequency for these states, limiting this method to states 11111, 01110, and 00100. Because capacitively loading the iris vias shifts both the even mode and iris resonance down in frequency, the lack of independent control means that the bandwidth of the third-order response cannot be continuously tuned.

It is possible to realize a third-order response with less passband ripple by modifying the design to have less inter-resonator coupling, thereby reducing the bandwidth and the required external coupling. Fig. 4.12 demonstrates a modified design with a smaller inductive iris and only three iris tuning vias. A third-order response with $15\,\mathrm{dB}$ of return loss ripple is realized by loading the three tuning vias to a gap of 5.5 mil and the external tuning via to a gap of 6 mil. In this case, a new spurious resonance occurs at $9.5\,\mathrm{GHz}$ so further design modifications would be necessary to suppress this mode, but it has been shown that the iris resonance can be used to create a higher-order filter response.

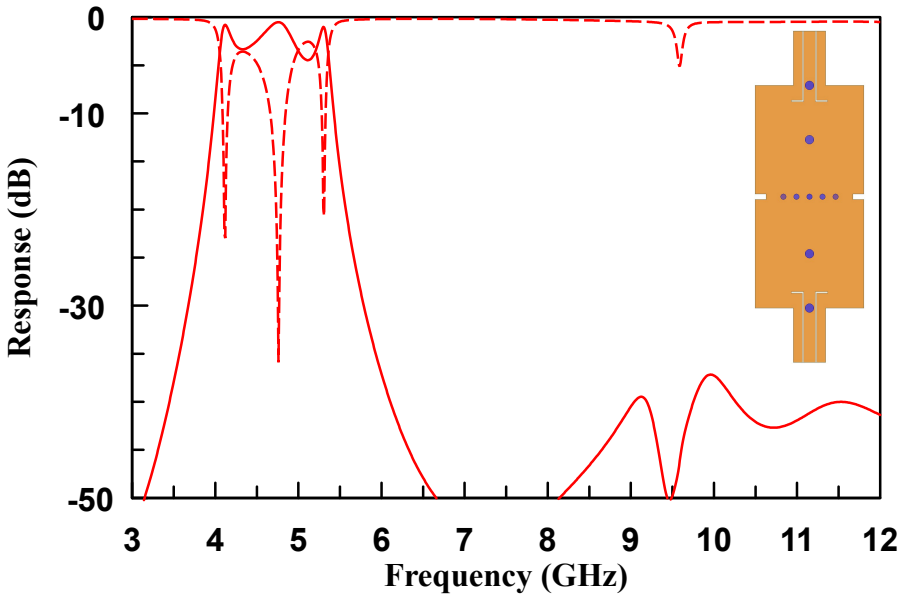

Figure 4.11: Third-order filter response realized by shorting iris vias 1 and 5 and heavily capacitively loading iris vias 2, 3, and 4 to bring the iris resonance into the passband.

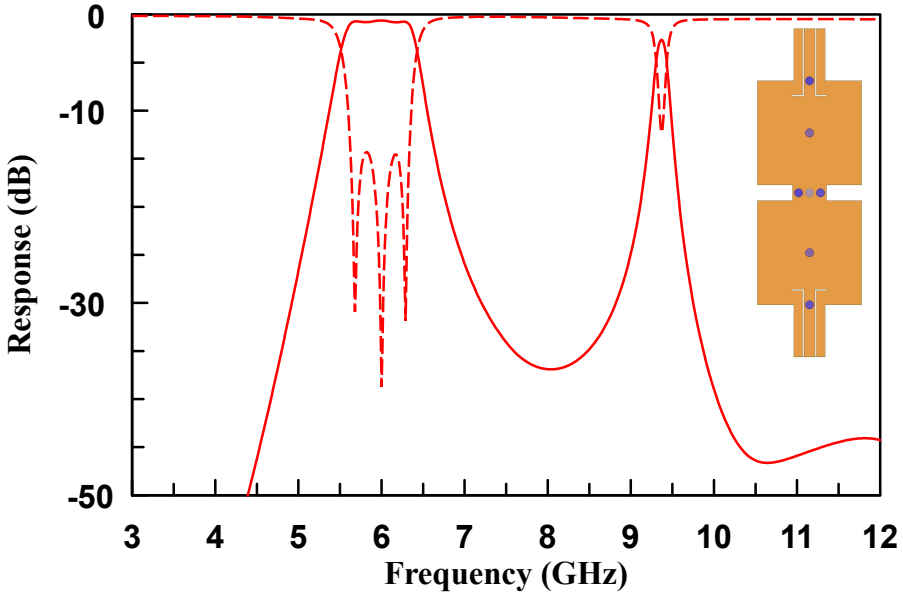

Figure 4.12: Third-order filter response realized with a modified design with a narrower inductive iris and only three iris vias. These three iris vias are heavily capacitively loaded to bring the iris resonance into the passband.

4.4 Fully Reconfigurable Design

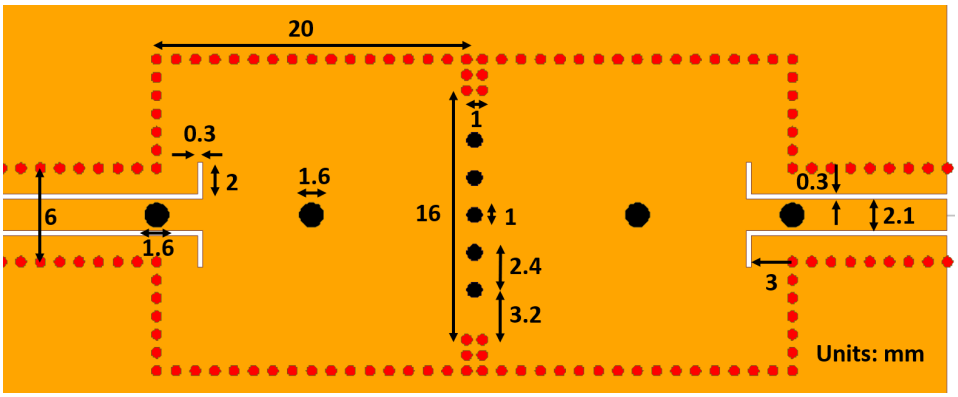

Figure 4.13: Physical dimensions of the fabricated filter design.

The final filter model with the tunable external and inter-resonator coupling via and all other design dimensions is illustrated in Fig. 4.13. With the tuning capabilities of both the external and inter-resonator coupling mechanisms extracted, the full space of possible filter responses can be studied. From Eqs. 3.2 and 3.3, the maximum and minimum realizable fractional bandwidths and constant bandwidths across the frequency band can be calculated. Since the k_{12} has a maximum achievable value and is directly related to the realizable fractional bandwidth, it can be used to calculate the maximum realizable fractional bandwidth across the frequency band. Q_{ext} likewise has a maximum achievable value across frequency and due to its inverse relationship to the fractional bandwidth, it forms the lower bound across frequency. Using the g-coeffcients for a Butterworth response, these limits on the realizable fractional bandwidth can be plotted in Fig. 4.14 along with constant absolute bandwidth traces of $200\,\mathrm{MHz}$ and $100\,\mathrm{MHz}$. With this design, the filter can achieve a constant FBW from 2% to 7% throughout the frequency tuning range.

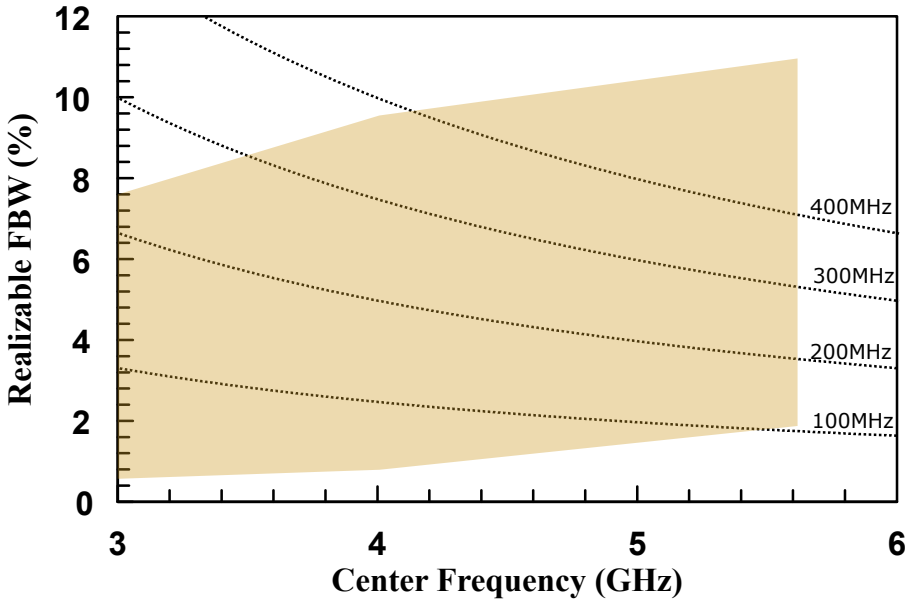

Figure 4.14: Butterworth-response FBW tuning space of the filter as a function of frequency due to the limiting values of Q_{ext} and k_{12}. Constant absolute bandwidth curves are also plotted inside the FBW space of the filter.

With full coupling structure characterization, a range of bandwidths or response shapes can be realized with this design. Through Driven Modal HFSS analysis of the full model shown in Fig. 4.15, both Butterworth responses (Fig. 4.16) and $-20\,\mathrm{dB}$ equi-ripple Chebyshev responses (Fig. 4.17) are simulated from the design to demonstrate its tuning capabilities. Narrowband Butterworth responses are also simulated across the frequency band in Fig. 4.18. All the tuning states of the resonator via, external via, and iris vias for the different displayed responses are shown in Table. 4.3. The fractional bandwidth for the Chebyshev response is again calculated from the 3-dB bandwidth to allow for easier direct comparison to the Butterworth response.

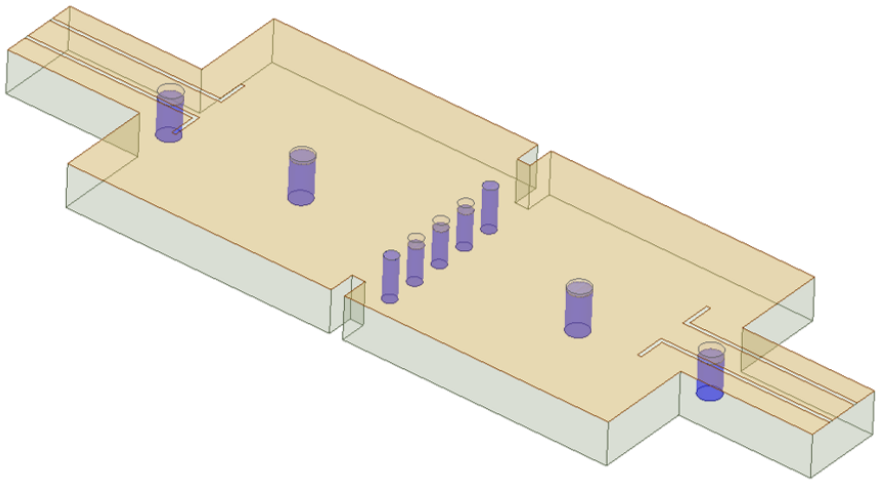

Figure 4.15: Driven Modal HFSS model of the fully reconfigurable filter design employing capacitive loading posts for the resonator, external coupling, and inter-resonator coupling tuning.

Table 4.3: Tuning state of all the liquid metal tuning vias to realize several simulated filter responses.

Filter response characteristics			**Tuning via air gaps (mil)**						
Type	f_0 **(GHz)**	**FBW (%)**	**Res**	**Ext**	**Iris 1**	**Iris 2**	**Iris 3**	**Iris 4**	**Iris 5**
Butterworth	3.2	1.5	1	2.75	0	125	0	125	125
Butterworth	3.2	11.5	1	0.85	20	20	20	20	20
Chebyshev	3.2	11.4	1	0.775	20	20	20	20	20
Butterworth	4.1	1.6	3.5	11	125	0	125	0	125
Butterworth	4.2	11.9	3.5	1.75	0	30	30	30	60
Chebyshev	4.0	14.2	3.5	1.9	125	125	125	125	125
Butterworth	5.9	1.5	125	1.7	0	0	125	0	0
Butterworth	5.8	11.7	125	5.3	0	125	125	125	0
Chebyshev	5.8	11.1	125	5	0	125	125	125	0

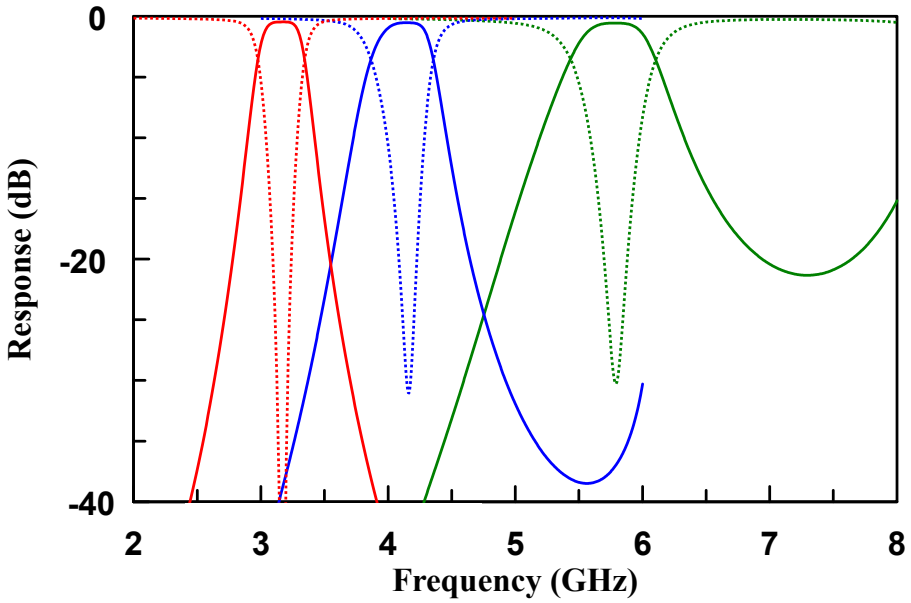

Figure 4.16: Wide bandwidth Butterworth responses from the fully reconfigurable filter design.

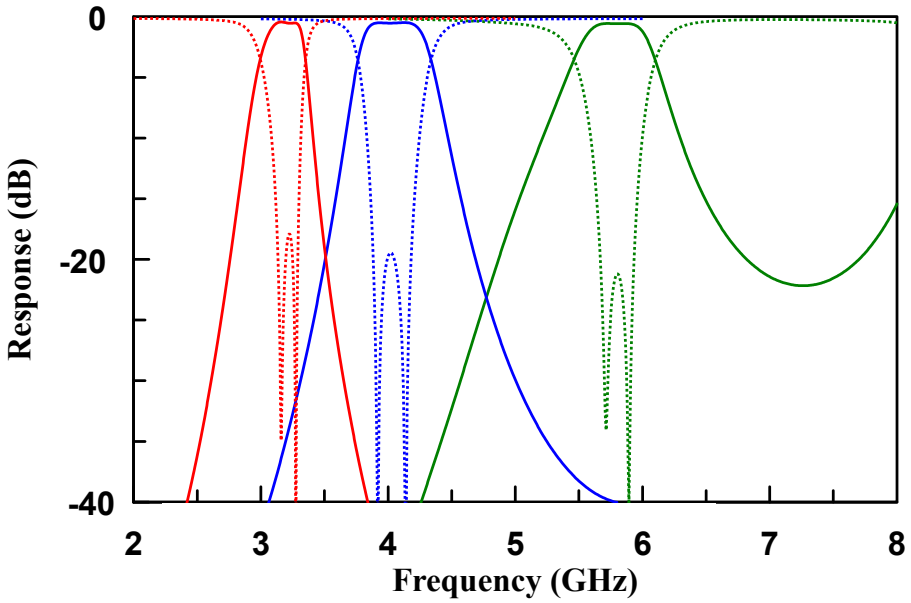

Figure 4.17: Wide bandwidth $-20\,\mathrm{dB}$ equi-ripple Chebyshev responses from the fully reconfigurable filter design.

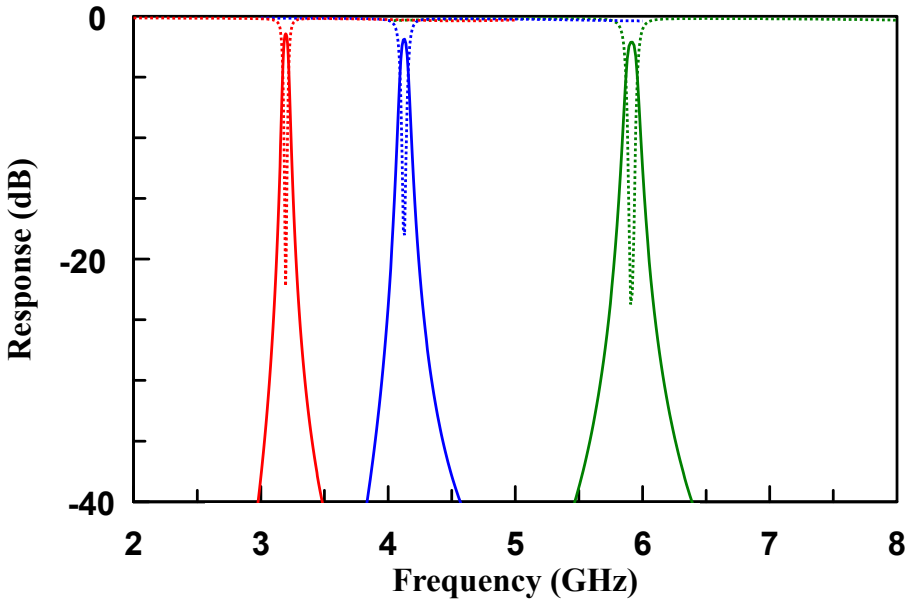

Figure 4.18: Narrow bandwidth Butterworth responses from the fully reconfigurable filter design.

4.5 Fabrication and Measurement Setup

Due to the increase in the number of liquid metal tuning vias, the availability of new fabrication methods, and sensitivity issues from the previous design, modifications were made to the fabrication process and tuning structure. Rather than the original tuning mechanism design in Fig. 2.3, a modified mechanism using PCB rivets and heat shrink Teflon tubing was designed as shown in Fig. 4.19. In this design, the Plexiglass interfaces were removed from the design and instead a partial brass PCB rivet was soldered to the bottom of each tuning via. Heat shrink FEP Teflon tubing from Electro Insulation was then placed on the outside of the PCB rivet and heated to form around the PCB rivet to form a strong grip. This allows Galinstan to be injected in through the Teflon tubes and then pass through a brass PCB rivet which allows for the Galinstan to make a strong electrical connection with the outer walls of the cavity before it enters into the tuning post via.

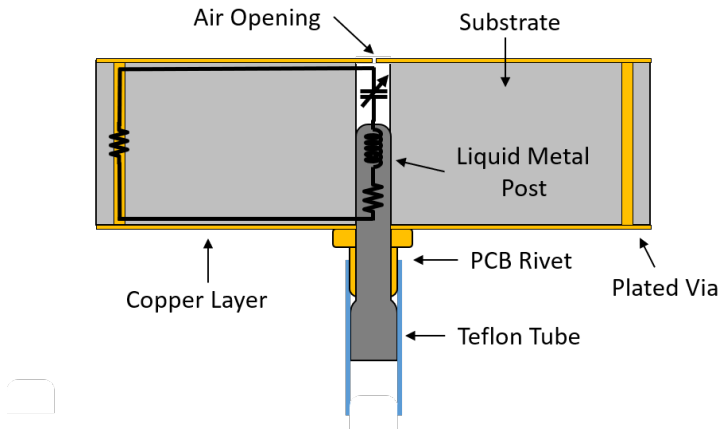

Figure 4.19: Modified tuning mechanism with PCB rivet and heat shrink Teflon tube.

From Chapter 2, it was discussed that top air opening holes were created through the precise tapping of a $0.2\,\mathrm{mm}$ microcutter onto the top area of each tuning via before partially drilling the substrate away from the bottom to form the diaphragm. This method had inconsistent results since the tapping of the microcutter can be imprecise and may create air openings that are larger than intended. With the availability of an LPKF ProtoLaser U4 during this design, the air via holes were instead created through a laser milling process. With the increased precision of the laser, each air opening can be consistently made to be the same size. The single microcutter air opening were then replaced with five $25\,\mu\mathrm{m}$ laser milled air openings, which were photographed with a digital microscope in Fig. 4.20 for both the external coupling tuning via and the resonator tuning via.

The five inter-resonator coupling tuning vias need to be designed so that they can be shorted to the top of the cavity. Instead of having the copper diaphragm with air openings, the entire via is drilled after the plating process to create an unplated via hole through the entire substrate and copper layers. In order to allow for a strong electrical connection then between the top and bottom of the substrate when

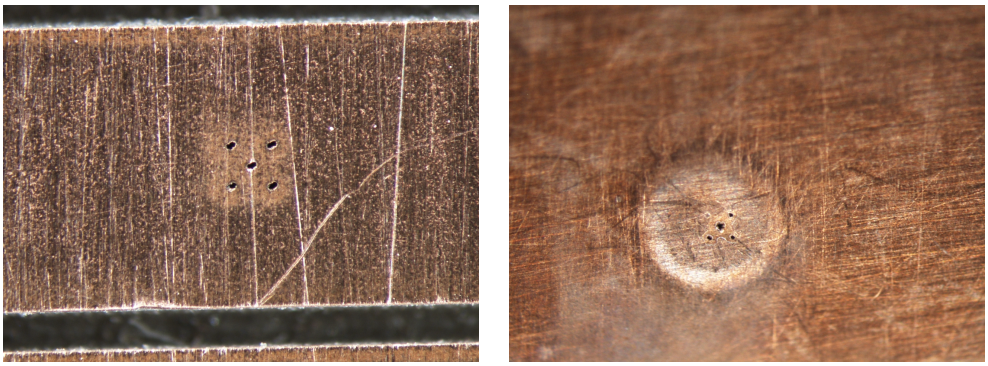

(a) (b)

Figure 4.20: Top air openings of the fabricated fully reconfigurable filter design for the a) Q_{ext} tuning via along the GCPW line and b) the center resonator tuning via.

a via is shorted, the same PCB rivet with heat shrink design for the other tuning mechanisms is soldered to both the bottom and top of the device.

The entire fabricated design with the brass PCB rivets soldered to the top and bottom of the device is shown in Fig. 4.21 with photographs from the top, bottom, and side of the device. Note that on the top side of the device in Fig. 4.21(a) there are only five PCB rivets soldered to the location of the iris tuning vias. Small copper deformations can be seen at the areas of the resonator and external coupling tuning vias created by the same T-Tech Quick Circuit J5 precise depth milling from Chapter 2. Depicted in Fig. 4.21(b), nine brass PCB rivets were soldered on the backside of the device at the locations of the iris, resonator, and external coupling tuning vias. A side view of the device along the longer edge is seen in Fig. 4.21(c). Since the resonator and external coupling tuning vias are both $1.6\,\mathrm{mm}$ in diameter, the PCB rivets soldered at those locations were selected to be $1.7\,\mathrm{mm}$ in diameter to allow for alignment tolerances. The larger PCB rivet diameter means that the Galinstan will make contact with more of the copper on the bottom of the device, which only improves the electrical connection between the Galinstan and the filter.

The iris tuning vias are only $1\,\mathrm{mm}$ in diameter, so the PCB rivets soldered to the top and bottom of these vias were selected to have a diameter of $1.3\,\mathrm{mm}$.

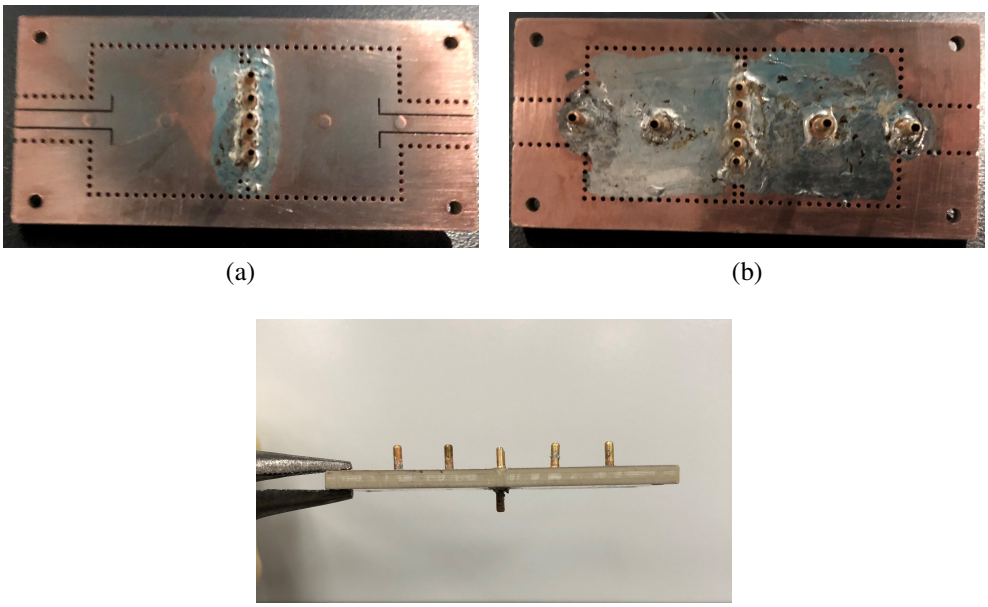

(a) (b)

(c)

Figure 4.21: Fabricated fully reconfigurable filter design with PCB rivets soldered onto each of the tuning holes from different angles. Photographs of the a) top view, b) bottom view, and c) side view of the design are shown.

In order to supply Galinstan to each of the resonator and external coupling tuning vias, 16-gauge heat shrink FEP tubing with an initial diameter of $1.9\,\mathrm{mm}$ is placed over the $1.7\,\mathrm{mm}$ PCB rivets. This tubing has a minimum retracted diameter of $1.55\,\mathrm{mm}$, which means that it will make a strong airtight connection to the outside of the PCB rivets when it is heated. At the opposite end of a length of this tubing are syringe needle heads with luer locks that will be used to inject the Galinstan in through syringes. For the iris tuning vias, 18-gauge heat shrink FEP tubing with an initial diameter of $1.52\,\mathrm{mm}$ and a retracted diameter of $1.24\,\mathrm{mm}$ is likewise placed over the $1.3\,\mathrm{mm}$ PCB rivets. Syringes needle heads are also placed at the end of these tubings. A photograph of the connected tubing and syringe tips

is seen in Fig. 4.22. Since the five iris tuning vias have PCB rivets on both the top and bottom of the device, the same tubing and syringes are also connected on the opposite side as is seen in the photograph in Fig. 4.23. In the same figure, the 3D printed mount, that aligns and holds the syringes in place, is also shown with the nine syringes connected to the bottom side of the filter.

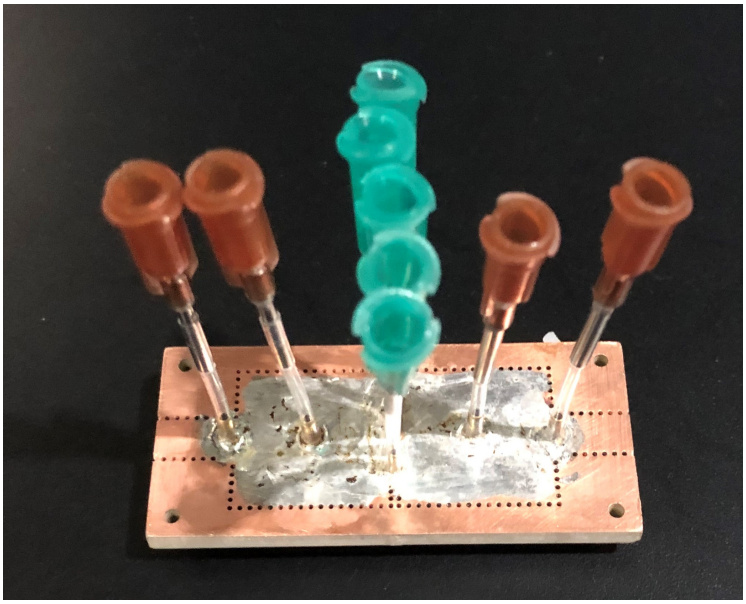

Figure 4.22: Filter with Teflon heat shrink tubing connecting syringe tips to the PCB rivets.

From the original resonator and filter design, it is best to mount the filter so that the Galinstan moves vertically so avoid angling of the top of the Galinstan post inside the via. Although the capillary effects of Galinstan in the narrow tuning via channels minimize this movement, it is still best to have a vertical mounting structure for the tuning of the filter. The entire filter with attached tubing and syringes is seen in Fig. 4.24 along with the mounting structure.

For the previous designs and measurements, the Galinstan was exposed to regular atmospheric air which led to oxidation. Even with the oxidation, the resonator of Chapter 2 and filter of Chapter 3 were able to properly tune. With the increased

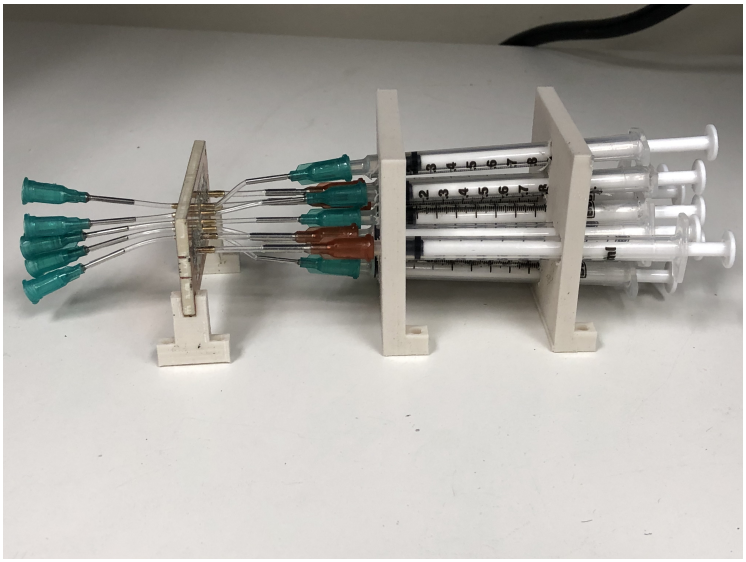

Figure 4.23: Side view of the entire device assembled with syringes attached to each tuning via for manual injection of Galinstan.

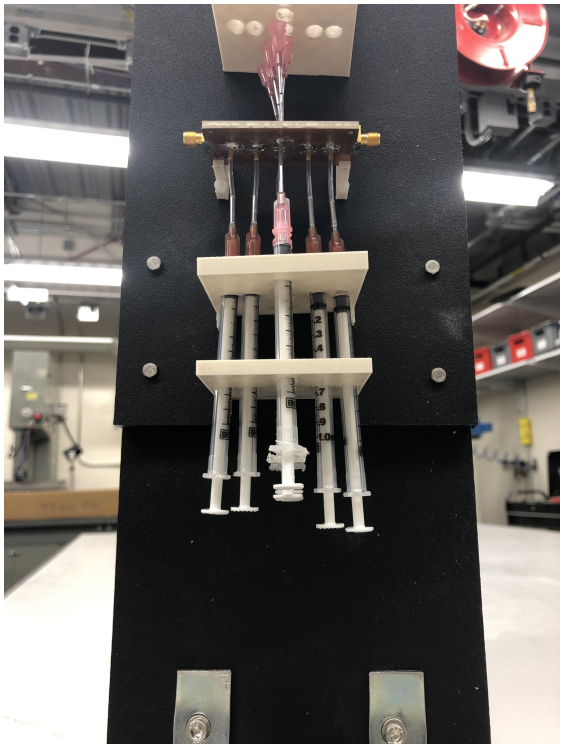

Figure 4.24: View of the entire device with attached syringes assembled into a vertical mounting structure.

number of tuning vias in this design, it became important to minimize the oxidation of the Galinstan since it becomes more gel-like and will be difficult to control for a design with so many tuning mechanisms. To prevent this oxidation, the entire design and mounting structure were placed in a sealed glove bag purged with nitrogen. This allows for better tunability and performance of the fully reconfigurable filter design. An image of the final testing setup inside the nitrogen-filled glove bag is shown in Fig. 4.25. An Agilent Technologies N9917A FieldFox is placed outside the glove bag, and coaxial cables are routed into the bag and air sealed to allow for measurement of the filter within the nitrogen environment. This measurement setup is shown in Fig. 4.26.

Figure 4.25: Entire mounting structure, Galinstan-filled syringes, and filter placed within a Nitrogen-filled sealed glove bag.

When the Galinstan is placed in the nitrogen environment of the glove bag, it has a lower viscosity that makes manual control of the syringes impractical. Because the substrate is only $3.125\,\mathrm{mm}$ thick and the diameter of the external tuning vias and resonator vias is $1.6\,\mathrm{mm}$, the volume of these vias is only $6.38\,\mu\mathrm{L}$. Unfor-

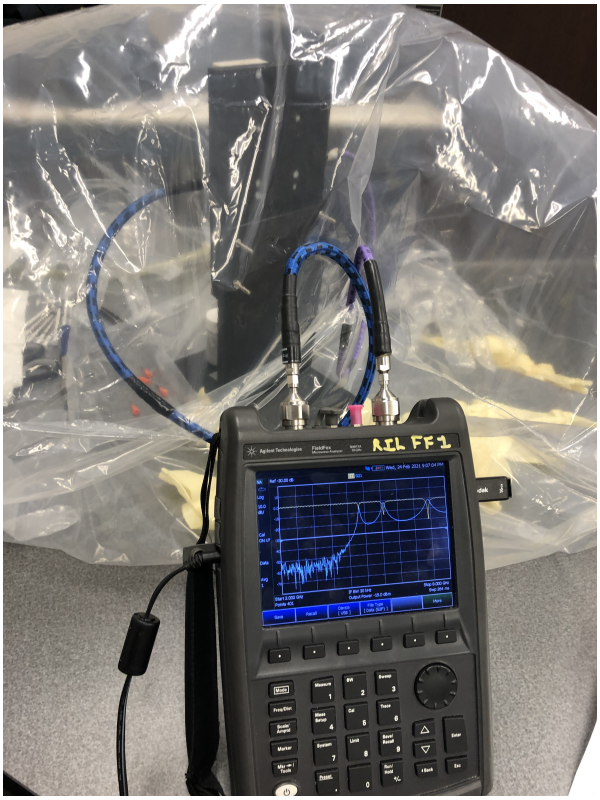

Figure 4.26: Connected Agilent Technologies N9917A FieldFox with coaxial cables routed into the glove bag to allow for measurement of the filter within a nitrogen environment.

tunately, microfluidic systems with the volumetric precision necessary to actuate all of these tuning vias are expensive and large at the time of this writing and would not be suitable for tuning this number of liquid metal channels. Such systems can not dry-pump so a co-fluid would need to be used with the Galinstan, which is avoided at this time. For this proof-of-concept design, the same syringes are used from the earlier chapters, but now an SM-13 Vernier Micrometer from Newport is placed below the syringes in a vise to provide tuning control. Because the micrometer has a resolution of $1.0\,\mu\mathrm{m}$, it allows for fine control of the syringe injection without a complex control system needing to be placed within the glove bag. When handling the micrometer and syringes in the glove bag, care must be taken since Galinstan

will still adhere to the inside of the syringes and Teflon tubing after some time, possibly due to adherence to contamination. Isopropyl alcohol or diluted hydrochloric acid can be used for cleaning of equipment to remove Galinstan, but residual Galinstan can still remain especially if heavily oxidized.

Multiple early samples were fabricated and tested, and it was found that extra care must be taken for certain parts of the fabrication process to prevent complications in the operation of the design. One issue was that the air openings at the top of the diaphragm might be too small or get clogged with debris. This causes injection of the liquid metal to be difficult since the air gap will become pressured and prevent proper tuning. It is important during the laser milling process that several passes are done to mill the air openings deep into the substrate, and after the T-Tech milling process that all the openings are checked and cleared with pressurized air. If the air openings are still too small after the PCB fabrication steps, it is possible to use a microcutter to manually make these openings larger. This is not recommended though as it was found that doing so can sometimes cause the opening to become too large, which will cause Galinstan to leak through the large air opening and not properly form the desired capacitive air gap.

Soldering the PCB rivets to the device can be difficult so in some earlier samples flux was used to allow for better solder flow. It was found that the flux can leak underneath or coat the inside of the PCB rivets and into the channel of the tuning vias. It is difficult to clean this flux out afterwards, and when the Galinstan later is injected into the channels, this flux will interact with the Galinstan and cause tuning issues due to it adhering more to the inner walls of the via. Therefore, flux should be avoided when soldering the rivets to the device. At the same time, enough solder should be added around the rivets since it forms the air seal between the PCB and the rivets. If there are gaps or openings in the solder around the rivets, Galinstan can

leak out from the edges of the rivets during tuning. This leakage can also happen if the heat shrink Teflon tubes are not properly heated to retract tightly around the rivets.

4.6 Measurements and Results

The fully reconfigurable design was tuned to demonstrate the resonator and coupling tuning mechanisms working together to realize multiple filter responses with different bandwidths and passband ripples. Fig. 4.27 shows four different measured states where the resonators were tuned across frequency with the external coupling was adjusted to realize a Butterworth response. Fig. 4.28 shows another state where the external coupling was adjusted to achieve a return loss ripple of about $10\,\mathrm{dB}$. The $3.8\,\mathrm{GHz}$ Butterworth has higher loss due to over-coupling of the external coupling and connector mismatch issues that will be discussed later, but it is still included in these graphs to demonstrate the tuning capabilities of the design. Since the external coupling dictates the passband ripple, realizing both these filter shapes at different frequencies demonstrates the wide continuous tuning of the external coupling vias.

During actual measurement, it was found that the inter-resonator tuning vias were difficult to continuously capacitively tune since unlike the resonator and external tuning vias, the iris vias have no copper diaphragm on top and instead have rivets on both side to allow for easier channel shorting. Regardless, the inductive post mechanism was still fully functional and was adjusted to realize about the same relative bandwidth across the tuning range so that a 5% fractional bandwidth for the Butterworth response was realized at $5.1\,\mathrm{GHz}$ and $5.6\,\mathrm{GHz}$. In addition, responses with $12\,\mathrm{dB}$ of return loss ripple were tuned at $4.5\,\mathrm{GHz}$ and $5.1\,\mathrm{GHz}$ to

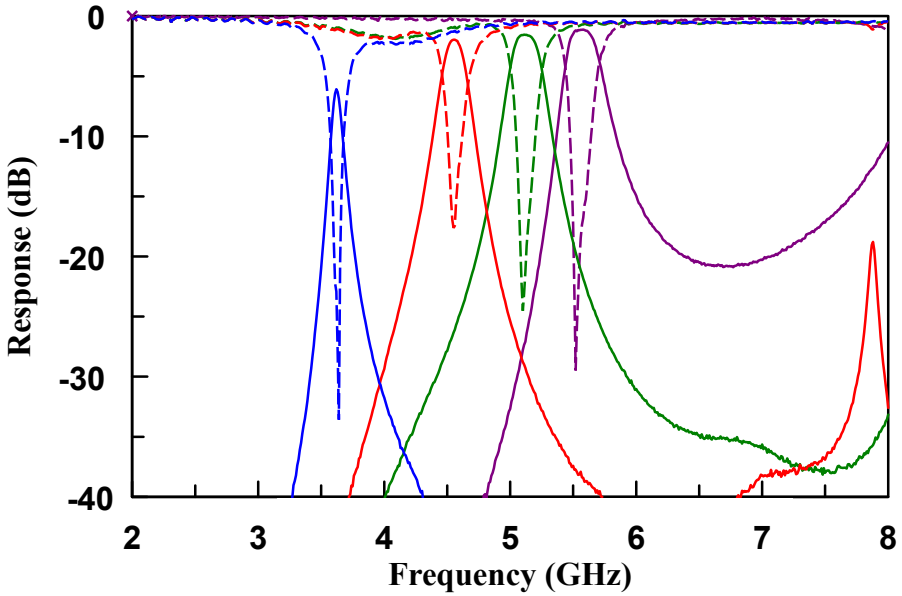

Figure 4.27: Measured results of the fully reconfigurable filter design tuned to achieve a Butterworth response at four different center frequencies.

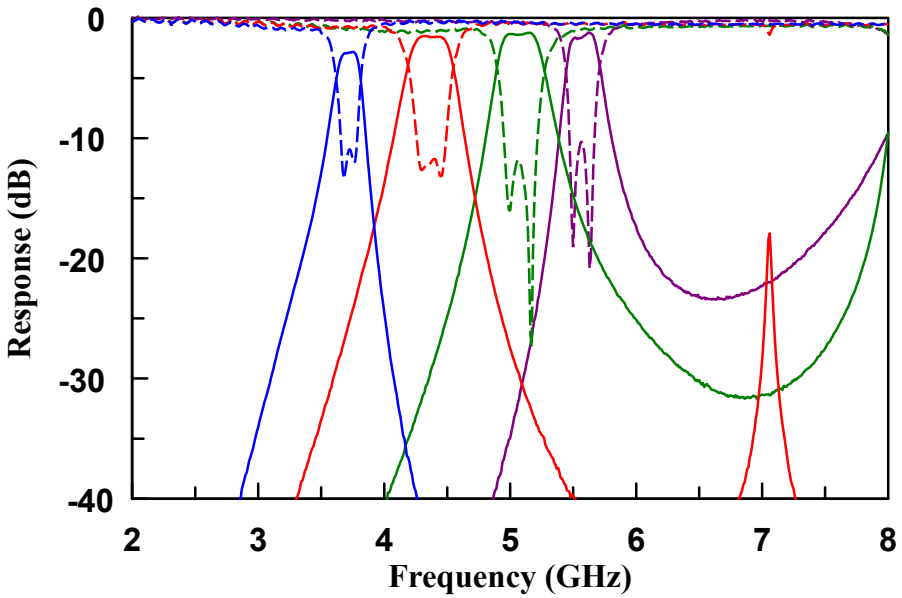

Figure 4.28: Measured results of the fully reconfigurable filter design tuned to achieve around a 10 dB ripple in the return loss at four different center frequencies.

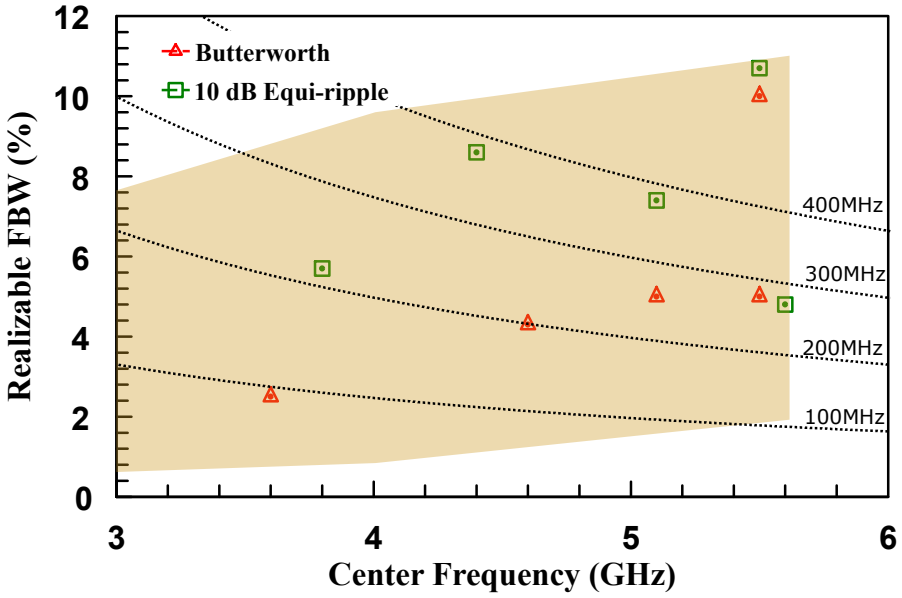

Figure 4.29: Bandwidth and center frequency points of the measured results within the tuning space for both the Butterworth and 10 dB equi-ripple response of Fig. 4.14.

both realize an absolute bandwidth of 378 MHz. A full plot of all the measured Butterworth and 10 dB equi-ripple responses within the bandwidth tuning space is plotted in Fig. 4.29. The fractional bandwidth for the Chebyshev response is again calculated from the 3-dB bandwidth to allow for easier direct comparison instead of the classical equi-ripple bandwidth definition. The distribution of the measured points within the bandwidth and center frequency tuning space for different filter shapes demonstrates part of the wide tuning capabilities of the design.

The fractional bandwidth and absolute bandwidth of all the 4.5 GHz, 5.1 GHz, and 5.6 GHz responses are reported in Table 4.4. Bandwidth tunability at a single frequency can be seen when comparing Fig. 4.30, where three iris vias were shorted to state 00110, and Fig. 4.31, where two iris vias were shorted to state 01110. For the Butterworth response in both figures, a 10% and 5% fractional bandwidth was measured for the two tuning states. The two figures demonstrate that the inter-

Table 4.4: Tuning state of all the liquid metal tuning vias of the simulated responses extracted to match the measured filter responses. The abbreviation B. and Ch. are used for the Butterworth and $10\,\mathrm{dB}$ equi-ripple Chebyshev responses respectively.

Filter Specifications				**Extracted tuning via air gaps (mil)**						
Type	f_0 **(GHz)**	**BW (MHz)**	**FBW (%)**	**Res**	**Ext**	**Ir 1**	**Ir 2**	**Ir 3**	**Ir 4**	**Ir 5**
B.	4.6	198	4.3	8.3	4.9	0	125	125	125	0
Ch.	4.4	378	8.6	7.2	4.0	0	125	125	125	125
B.	5.1	255	5.0	27	16	0	0	125	125	0
Ch.	5.1	377	7.4	29	10	0	0	50	50	0
B.	5.5	275	5.0	85	20	0	0	50	125	0
Ch.	5.6	269	4.8	85	32	0	0	50	125	0
B.	5.5	550	10.0	125	11	0	125	125	125	0
Ch.	5.5	589	10.7	125	14	0	125	125	125	0

resonator coupling can be independently adjusted from the frequency tuning of the resonators and the external coupling tuning to realize different bandwidths with the same frequency and response ripple. Simulated traces are also included on these plots where HFSS simulations were done to replicate a similar tuning state since there is not a way to measure the air gap within each tuning via. Measured and simulated response traces with two different tuned filter shapes are also plotted for the $5.1\,\mathrm{GHz}$ and $4.5\,\mathrm{GHz}$ responses in Fig. 4.32 and Fig. 4.33 respectively. The extracted air gaps that match each one of the measured responses are reported in Table 4.4.

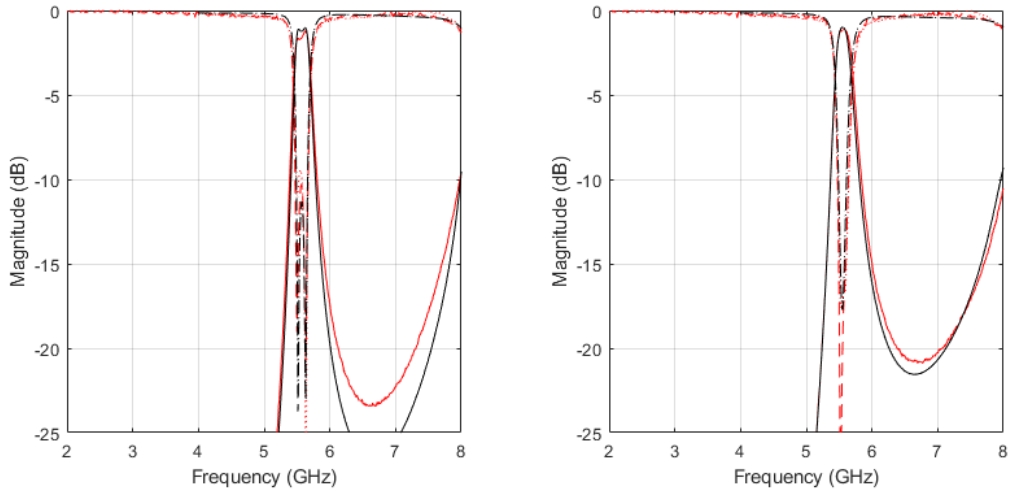

Figure 4.30: Measured and simulated results from filter sample 1 tuned to a center frequency of $5.6\,\mathrm{GHz}$ for both a narrowband $11\,\mathrm{dB}$ ripple in the return loss and a Butterworth response. The red trace is the measured results and the black trace are simulated responses to replicate the measured response.

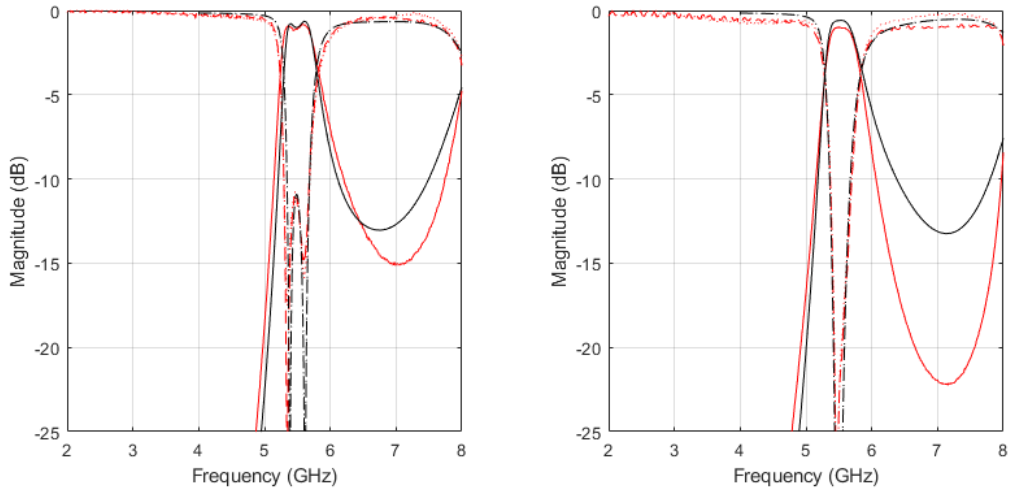

Figure 4.31: Measured and simulated results from filter tuned to a center frequency of $5.6\,\mathrm{GHz}$ for both a wideband $11\,\mathrm{dB}$ ripple in the return loss (sample 1) and a Butterworth response (sample 2). The red trace is the measured results and the black trace are simulated responses to replicate the measured response.

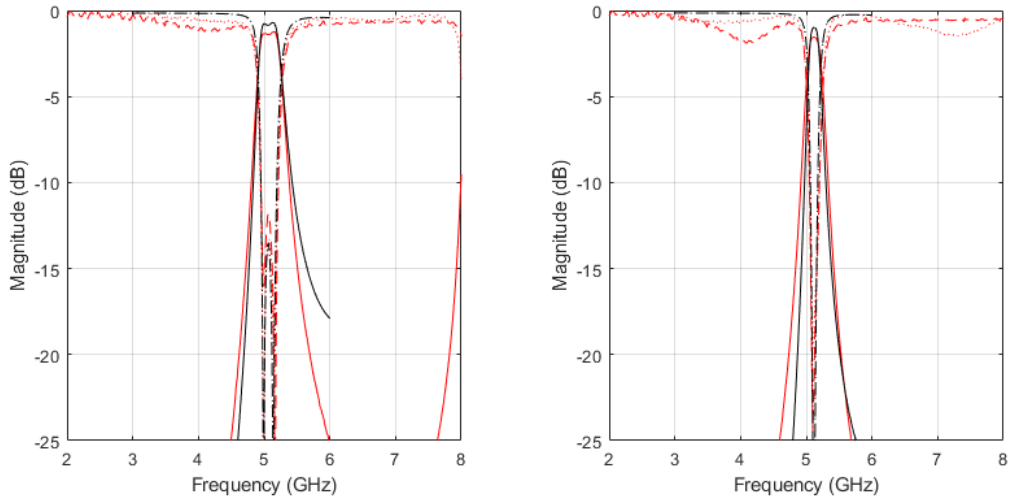

Figure 4.32: Measured results from filter sample 2 tuned to a center frequency of $5.1\,\mathrm{GHz}$ for both a $12\,\mathrm{dB}$ ripple in the return loss and a Butterworth response. The red trace is the measured results and the black trace are simulated responses to replicate the measured response.

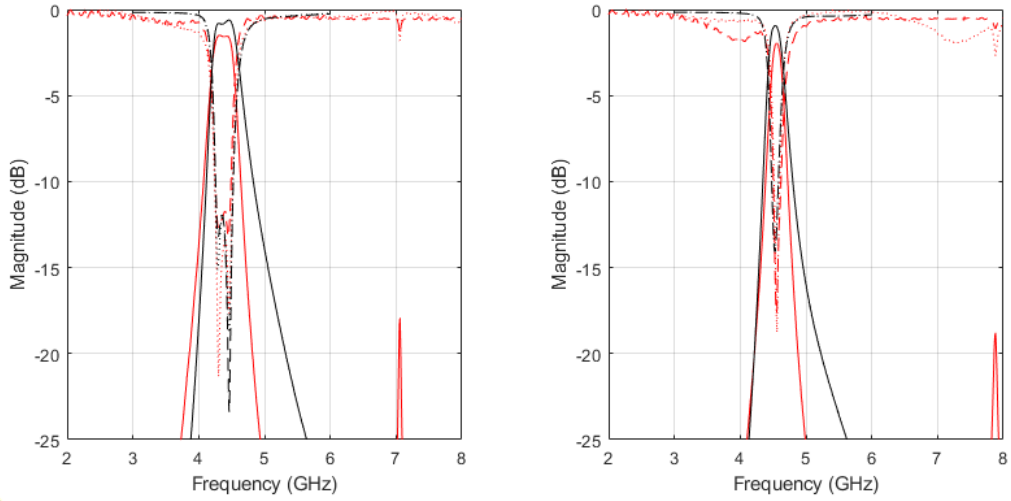

Figure 4.33: Measured and simulated results from filter sample 2 tuned to a center frequency of $4.5\,\mathrm{GHz}$ for both an $11\,\mathrm{dB}$ ripple in the return loss and a Butterworth response. The red trace is the measured results and the black trace are simulated responses to replicate the measured response.

The Galinstan used in this experiment was reused from prior experiments where it had previously been exposed to oxygen. Oxygen exposure only forms a thin oxide layer, but this oxide contamination remains in the sample and can partially explain the higher insertion loss of the measured results compared to simulation, which are recorded in Table 4.5. The measured data was also taken from two different filter samples since after some time the Galinstan would adhere to the inside of some tuning vias and stop tuning effectively, which will need to be addressed in future designs through the inclusion of a co-fluid or Teflon coating of the inside of the tuning vias. Some measured tuning states exhibit a discrepancy in the above-passband leakage compared to simulation and ripples in the out-of-band return loss. From simulation, these differences are likely the result of an additional resistive current path from the external tuning vias which might be created from small oxidized slivers of liquid metal shorting the Galinstan surface to the top of the cavity which will likely be resolved by the incorporation of a co-fluid and Teflon coating. Aside from this discrepancy, the measured results show good agreement with the simulated results and validate the high reconfigurability of the design found in simulation. The ability to tune the filter shape, center frequency, and bandwidth demonstrates that all the tuning via mechanisms work as expected and that the design has full second-order response reconfigurability over a wide tuning range.

Table 4.5: Comparison of the measured and simulated insertion loss for the different tuning states.

Butterworth			
f_0 **(GHz)**	**FBW (%)**	**Simulated IL (dB)**	**Measured IL (dB)**
3.6	2.5	1.5	6.1
4.6	4.3	0.9	2.0
5.1	5	1.0	1.5
5.5	5	1.0	1.1
5.5	10	0.6	1.0
10 dB Equi-ripple			
f_0 **(GHz)**	**FBW (%)**	**Simulated IL (dB)**	**Measured IL (dB)**
3.8	5.7	1.2	2.8
4.4	8.6	0.6	1.5
5.1	7.4	0.7	1.2
5.6	4.8	1.0	1.2
5.5	10.7	0.7	0.9

4.7 Summary

A fully reconfigurable filter controlled only by liquid metal tuning posts has been demonstrated and verified. The unique tuning via design for the external coupling and iris allowed for the realization of both a Butterworth and Chebyshev response at different frequencies and with different bandwidths. Frequency tuning of a second-order Butterworth response was measured from $3.8\,\mathrm{GHz}$ to $5.6\,\mathrm{GHz}$. Bandwidth tuning of a Butterworth response was demonstrated at $5.6\,\mathrm{GHz}$ for a fractional bandwidth of 5% and 10%. A 5% fractional bandwidth Butterworth response was measured at $5.1\,\mathrm{GHz}$, and $5.6\,\mathrm{GHz}$, and responses with $12\,\mathrm{dB}$ of return loss ripple were tuned to have an absolute bandwidth of $378\,\mathrm{MHz}$ at $4.5\,\mathrm{GHz}$ and $5.1\,\mathrm{GHz}$. At every recorded frequency and bandwidth, the external coupling was tuned to realize both a Butterworth response and around a $10\,\mathrm{dB}$ return loss ripple Chebyshev response. Together these measured results validate bandwidth tuning at a single frequency, frequency tuning with constant absolute bandwidth, frequency

tuning with constant fractional bandwidth, and filter shape tuning at different frequencies and bandwidths. At the current stage of the design, there are still challenges with precise and repeatable control of all the liquid metal tuning vias, and a future automated control mechanism and a co-fluid will need to be incorporated to prevent internal via coating and oxidation. Nevertheless, the work presented in this chapter still has proven that the concept of these variable liquid metal tuning mechanisms for control of the external and inter-resonator coupling is highly promising for advanced full reconfigurability.

Chapter 5

Future Work and Conclusion

5.1 Conclusion

The increasing demands of modern wireless communication and radar systems call for RF hardware with advanced reconfigurability to realize future systems with dynamic spectrum access. The development of small, light, low-cost, and high-power handling tunable filters plays a crucial role in future spectral efficiency and system flexibility. Substrate integrated waveguide filters lay in middle the space between large, expensive waveguide filters and lossy, radiative microstrip filters.

The development of tunable liquid metal filter designs allow for new possibilities of linearity, repeatability, flexibility, and high-power handling over traditional tuning methods. The work of this thesis develops this area through the development of a continuously tunable capacitive loading mechanism using liquid metal actuation. The tuning mechanism provides potential higher power handling and linearity than previous varactor designs while having more repeatability and reversibility than mechanical tuning designs. The liquid metal tuning also has the advantage of being able to tune from a completely unloaded state to a highly capacitively loaded resonator state, something which piezoelectric actuator SIW filter designs are not capable of. With the demonstration of an SIW resonator design in Chapter 2, a

frequency-tunable second-order bandpass filter in Chapter 3, the liquid metal tuning mechanism is capable of realizing the same level of frequency tunability as competing mechanisms.

Finally, Chapter 4 presents a novel liquid metal tuning mechanism for external and inter-resonator coupling to realize a fully reconfigurable filter design. Most prior work in fully reconfigurable filter designs relied on varactor-based tuning of the coupling mechanisms which have higher losses and lower power handling capabilities. The mixed inductive and capacitive coupling tuning mechanism through shortable capacitive loading posts has not been used in prior works to the author's knowledge due to the limitations of other tuning mechanisms. This makes this tunable coupling mechanism a unique design that benefits specifically advantages of liquid metal tuning.

Through this work, a simulated and measured resonator design demonstrated tuning capabilities from $3.3\,\mathrm{GHz}$ to $5.7\,\mathrm{GHz}$ as well as a second-order bandpass filter design with the same frequency tuning capabilities. Finally, a fully reconfigurable bandpass filter design capable of bandwidth tuning a Butterworth response from 2% to 10% FBW tuning at $5.6\,\mathrm{GHz}$ and a 1% to 7% FBW tuning at $3\,\mathrm{GHz}$ was simulated and measured. Constant-absolute-bandwidth frequency tuning, constant-fractional-bandwidth frequency tuning, constant-frequency bandwidth tuning, and arbitrary filter shape tuning have been experimentally validated. Coupling tuning to realize a fully reconfigurable design has not been demonstrated before with liquid metal, and such a highly reconfigurable liquid metal filters that is widely tunable in frequency, bandwidth, and shape is a considerable developmental step in the field of tunable microwave filter designs.

5.2 Future work

While this design used five inter-resonator tuning vias, different topologies that simplify the number of vias and thereby reduce the complexity of the design should be explored. Changing the shape of the iris through different mechanisms or milling different plated trenches in the center of the iris to create in-built capacitive coupling may increase the tunable range of each via as well as mitigate the effects of the higher order iris resonance. These types of investigations into this coupling tuning mechanism is open for study since prior tuning mechanism have not allowed for full loading and unloading of capacitive posts while maintaining repeatability and size like liquid metal has.

A closed loop system will also need to be developed to seal the Galinstan in the system and prevent the effects of oxidation, and a dielectric co-fluid should be incorporated. Such an automated control system will also need to develop different mechanisms to sense the current state of the filter. The field of automatic filter tuning has been well studied and many prior techniques could be used again for this design [61]. Monitoring of the resonators [62], sensing of the differential modes [63], or capacitive sensing [64,65] techniques are all possible options for automated sensing of this design since it does not behave fundamentally differently from other SIW evanescent-mode filter designs. In addition, possible new sensing techniques from the realm of microfluidics may present new paths for automated sensing of the level and volume of the Galinstan in each tuning post through volumetric dispensing or pressure sensing techniques. Likely, the most promising avenue will be some sort of capacitive sensing rod that can be placed partially into the substrate that can measure the capacitance between the sensor and the liquid metal post to extract the amount of liquid metal already in the cavity.

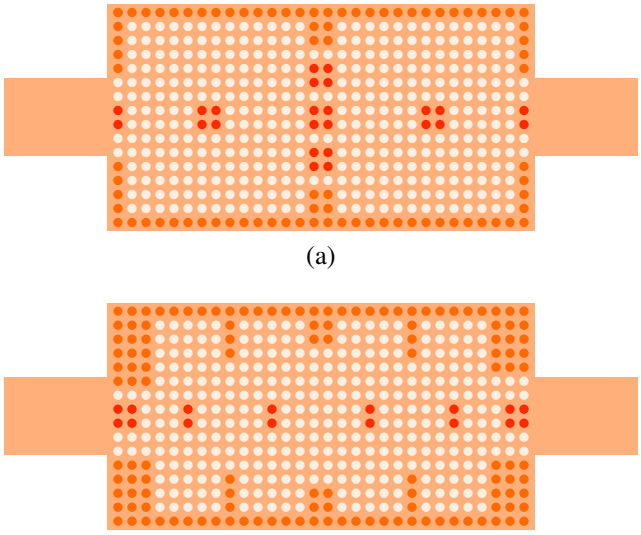

Figure 5.1: A fully programmable liquid-metal-via array configured to a) a second-order tunable filter and b) a fourth-order tunable filter.

Further, in the future with improvements in the continuous tuning mechanism and a method for automated sensing and control of the liquid metal, the design of a fully programmable liquid-metal-via array could be achieved. By creating an array of empty vias which are either capacitively tunable or shortable, a wide range of topologies can be realized such as order-reconfigurable filters, diplexers, power splitters, phase shifters, and more to realize a wide range of microwave SIW designs. An example of a second-order and fourth-order state of such a liquid-metal-via array is shown in Fig. 5.1 with white for empty vias, red for capacitively tunable vias, and dark orange for vias shorted with liquid metal. Such a highly reconfigurable design would allow for the linearity, high-power handling, and wide tunability of liquid metal to be rapidly designed and deployed to numerous applications. The liquid metal tuning work of this thesis, then, lays the groundwork for numerous potential liquid metal RF devices with high performance and advanced reconfigurability beyond filters.

Bibliography

[1] T. S. Rappaport, S. Sun, R. Mayzus, H. Zhao, Y. Azar, K. Wang, G. N. Wong, J. K. Schulz, M. Samimi, and F. Gutierrez, "Millimeter wave mobile communications for 5g cellular: It will work!" *IEEE Access*, vol. 1, pp. 335–349, 2013.

[2] H. Song and T. Nagatsuma, "Present and future of terahertz communications," *IEEE Transactions on Terahertz Science and Technology*, vol. 1, no. 1, pp. 256–263, 2011.

[3] U.S. Department of Commerce, National Telecommunications and Information Administration, Office of Spectrum Management, "United states frequency allocations: The radio spectrum," ntia.doc.gov, https://www.ntia.doc.gov/files/ntia/publications/january_2016_spectrum_wall_chart.pdf (accessed 1 March 2021).

[4] L. Pei, J. Liu, Y. Chen, R. Chen, and L. Chen, "Evaluation of fingerprinting-based wifi indoor localization coexisted with bluetooth," *The Journal of Global Positioning Systems*, vol. 15, 12 2017.

[5] D. Lu, M. Yu, N. S. Barker, Z. Li, W. Li, and X. Tang, "Advanced synthesis of wide-tuning-range frequency-adaptive bandpass filter with constant absolute bandwidth," *IEEE Transactions on Microwave Theory and Techniques*, vol. 67, no. 11, pp. 4362–4375, Nov 2019.

[6] J. Lee, E. J. Naglich, H. H. Sigmarsson, D. Peroulis, and W. J. Chappell, "Frequency-agile field-programmable filter array (fpfa) with multiple functionalities," in *2011 IEEE MTT-S International Microwave Symposium*, 2011, pp. 1–4.

[7] H. H. Sigmarsson, E. Naglich, J. Lee, D. Peroulis, and W. Chappell, "Tunable bandpass and bandstop filter cascade for dynamic pole allocation," in *Proceedings of the 2012 IEEE International Symposium on Antennas and Propagation*, 2012, pp. 1–2.

[8] T. Lee, J. Lee, and D. Peroulis, "Dynamic bandpass filter shape and interference cancellation control utilizing bandpass–bandstop filter cascade," *IEEE*

Transactions on Microwave Theory and Techniques, vol. 63, no. 8, pp. 2526–2539, 2015.

[9] S. Saeedi, J. Lee, and H. H. Sigmarsson, "Tunable, high-q, substrate-integrated, evanescent-mode cavity bandpass-bandstop filter cascade," *IEEE Microwave and Wireless Components Letters*, vol. 26, no. 4, pp. 240–242, 2016.

[10] S. Jeong, T. Lee, and J. Lee, "Frequency- and bandwidth-tunable absorptive bandpass filter," *IEEE Transactions on Microwave Theory and Techniques*, vol. 67, no. 6, pp. 2172–2180, 2019.

[11] X. P. Chen and K. Wu, "Substrate integrated waveguide filter: basic design rules and fundamental structure features," *IEEE Microwave Magazine*, vol. 15, no. 5, pp. 108–116, 2014.

[12] R. Zhang, J. zhou, B. Yang, and Y. Ding, "Low phase noise integrated mechanically tunable oscillator based on multi-layer siw bandpass filter," in *2018 Asia-Pacific Microwave Conference (APMC)*, 2018, pp. 1127–1129.

[13] G. Li, Y. Zhao, and Y. Gao, "A novel multilayer siw filter using silicon based mems technology," in *2019 International Conference on Microwave and Millimeter Wave Technology (ICMMT)*, 2019, pp. 1–3.

[14] S. Sirci, J. D. Martínez, M. Taroncher, and V. E. Boria, "Varactor-loaded continuously tunable siw resonator for reconfigurable filter design," in *2011 41st European Microwave Conference*, 2011, pp. 436–439.

[15] W. Y. Sam, Z. Zakaria, and M. A. Mutalib, "The investigation of reconfigurable siw filter using varactor diodes," in *2016 IEEE 5th Asia-Pacific Conference on Antennas and Propagation (APCAP)*, 2016, pp. 167–168.

[16] S. Sirci, J. D. Martínez, and V. E. Boria, "Low-loss 3-bit tunable siw filter with pin diodes and integrated bias network," in *2013 European Microwave Conference*, 2013, pp. 1211–1214.

[17] D. Psychogiou and K. Sadasivan, "Tunable coaxial cavity resonator-based filters using actuated liquid metal posts," *IEEE Microwave and Wireless Components Letters*, vol. 29, no. 12, pp. 763–766, Dec 2019.

[18] J. H. Dang, R. C. Gough, A. M. Morishita, A. T. Ohta, and W. A. Shiroma, "A tunable X-band substrate integrated waveguide cavity filter using reconfigurable liquid-metal perturbing posts," in *2015 IEEE MTT-S International Microwave Symposium (IMS)*. IEEE, 2015, pp. 1–4.

[19] G. Mumcu, A. Dey, and T. Palomo, "Frequency-agile bandpass filters using liquid metal tunable broadside coupled split ring resonators," *IEEE Microwave and Wireless Components Letters*, vol. 23, no. 4, pp. 187–189, 2013.

[20] W. Irshad and D. Peroulis, "A 12–18 GHz electrostatically tunable liquid metal RF MEMS resonator with quality factor of 1400–1840," in *2011 IEEE MTT-S International Microwave Symposium (IMS)*, June 2011, pp. 1–4.

[21] S. N. McClung, S. Saeedi, and H. H. Sigmarsson, "Band-reconfigurable filter with liquid metal actuation," *IEEE Transactions on Microwave Theory and Techniques*, vol. 66, no. 6, pp. 3073–3080, 2018.

[22] T. Palomo and G. Mumcu, "Microfluidically reconfigurable metallized plate loaded frequency-agile rf bandpass filters," *IEEE Transactions on Microwave Theory and Techniques*, vol. 64, no. 1, pp. 158–165, 2016.

[23] A. Pourghorban Saghati, J. S. Batra, J. Kameoka, and K. Entesari, "A miniaturized microfluidically reconfigurable coplanar waveguide bandpass filter with maximum power handling of 10 watts," *IEEE Transactions on Microwave Theory and Techniques*, vol. 63, no. 8, pp. 2515–2525, 2015.

[24] A. M. Watson, K. Elassy, T. Leary, M. A. Rahman, A. Ohta, W. Shiroma, and C. E. Tabor, "Enabling reconfigurable all-liquid microcircuits via laplace barriers to control liquid metal," in *2019 IEEE MTT-S International Microwave Symposium (IMS)*, 2019, pp. 188–191.

[25] N. Vahabisani, S. Khan, and M. Daneshmand, "A k-band reflective waveguide switch using liquid metal," *IEEE Antennas and Wireless Propagation Letters*, vol. 16, pp. 1788–1791, 2017.

[26] S. Alkaraki, J. Kelly, A. L. Borja, R. Mittra, and Y. Wang, "Gallium-based liquid metal substrate integrated waveguide switches," *IEEE Microwave and Wireless Components Letters*, vol. 31, no. 3, pp. 257–260, 2021.

[27] G. J. Hayes, J. So, A. Qusba, M. D. Dickey, and G. Lazzi, "Flexible liquid metal alloy (EGaIn) microstrip patch antenna," *IEEE Transactions on Antennas and Propagation*, vol. 60, no. 5, pp. 2151–2156, 2012.

[28] K. Zhang, J. Zhang, S. Zhang, Z. Cao, and Y. He, "A frequency reconfigurable microstrip patch antenna based on liquid metal and pdms," in *2019 11th International Conference on Wireless Communications and Signal Processing (WCSP)*, 2019, pp. 1–5.

[29] G. B. Zhang, R. C. Gough, M. R. Moorefield, K. J. Cho, A. T. Ohta, and W. A. Shiroma, "A liquid-metal polarization-pattern-reconfigurable dipole antenna,"

IEEE Antennas and Wireless Propagation Letters, vol. 17, no. 1, pp. 50–53, 2018.

[30] Z. He, Z. Hua, L. Hongmei, S. Fan, L. Shu, and A. Denisov, "A reconfigurable yagi-uda antenna using egain liquid metal," in *2017 International Symposium on Antennas and Propagation (ISAP)*, 2017, pp. 1–2.

[31] M. Wang, I. M. Kilgore, M. B. Steer, and J. J. Adams, "Characterization of intermodulation distortion in reconfigurable liquid metal antennas," *IEEE Antennas and Wireless Propagation Letters*, vol. 17, no. 2, pp. 279–282, 2018.

[32] M. Kubo, X. Li, C. Kim, M. Hashimoto, B. J. Wiley, D. Ham, and G. M. Whitesides, "Stretchable microfluidic electric circuit applied for radio frequency antenna," in *2011 IEEE 61st Electronic Components and Technology Conference (ECTC)*, 2011, pp. 1582–1587.

[33] J. H. Dang, R. C. Gough, A. M. Morishita, A. T. Ohta, and W. A. Shiroma, "Liquid-metal-based phase shifter with reconfigurable ebg filling factor," in *2015 IEEE MTT-S International Microwave Symposium*, 2015, pp. 1–4.

[34] B. J. Lei, Wenqi Hu, A. T. Ohta, and W. A. Shiroma, "A liquid-metal reconfigurable double-stub tuner," in *2012 IEEE/MTT-S International Microwave Symposium Digest*, 2012, pp. 1–3.

[35] A. M. Morishita, J. H. Dang, R. C. Gough, A. T. Ohta, and W. A. Shiroma, "A tunable amplifier using reconfigurable liquid-metal double-stub tuners," in *2015 Texas Symposium on Wireless and Microwave Circuits and Systems (WMCS)*, 2015, pp. 1–4.

[36] M. D. Dickey, "Stretchable and soft electronics using liquid metals," *Advanced Materials*, vol. 29, no. 27, p. 1606425, 2017.

[37] W. Chen, Y. Li, R. Li, A. V. Thean, and Y. Guo, "Bendable and stretchable microfluidic liquid metal-based filter," *IEEE Microwave and Wireless Components Letters*, vol. 28, no. 3, pp. 203–205, 2018.

[38] K. Entesari and A. P. Saghati, "Fluidics in microwave components," *IEEE Microwave Magazine*, vol. 17, no. 6, pp. 50–75, 2016.

[39] L. Majidi, D. Gritsenko, and J. Xu, "Gallium-based room-temperature liquid metals: Actuation and manipulation of droplets and flows," *Frontiers in Mechanical Engineering*, vol. 3, p. 9, 2017. [Online]. Available: https://www.frontiersin.org/article/10.3389/fmech.2017.00009

[40] T. Liu, P. Sen, and C. Kim, "Characterization of nontoxic liquid-metal alloy galinstan for applications in microdevices," *Journal of Microelectromechanical Systems*, vol. 21, no. 2, pp. 443–450, 2012.

[41] S. McClung, "Mode-reconfigurable bandpass filters with liquid metal enablement," Master's Thesis, University of Oklahoma, 2017.

[42] T. Hutter, W.-A. C. Bauer, S. R. Elliott, and W. T. S. Huck, "Formation of spherical and non-spherical eutectic gallium-indium liquid-metal microdroplets in microfluidic channels at room temperature," *Advanced Functional Materials*, vol. 22, no. 12, pp. 2624–2631, 2012. [Online]. Available: https://onlinelibrary.wiley.com/doi/abs/10.1002/adfm.201200324

[43] D. Kim, P. Thissen, G. Viner, D. W. Lee, W. Choi, Y. J. Chabal, and J. B. Lee, "Recovery of nonwetting characteristics by surface modification of gallium-based liquid metal droplets using hydrochloric acid vapor," *ACS Appl Mater Interfaces*, vol. 5, no. 1, pp. 179–185, Jan 2013.

[44] L. C. Cadwallader, "Gallium safety in the laboratory," 5 2003. [Online]. Available: https://www.osti.gov/biblio/811932

[45] A. H. Pham, S. Saeedi, and H. H. Sigmarsson, "Continuously-tunable substrate integrated waveguide bandpass filter actuated by liquid metal," in *2019 IEEE MTT-S International Microwave Symposium (IMS)*, 2019, pp. 21–23.

[46] D. M. Pozar, *Microwave engineering*, 3rd ed. Hoboken, NJ: Wiley, 2005.

[47] G. Ariturk and H. H. Sigmarsson, "Lossy microwave filters with active shape correction," *IEEE Access*, pp. 1–1, 2021.

[48] Y. Gao, J. Powell, X. Shang, and M. J. Lancaster, "Coupling matrix-based design of waveguide filter amplifiers," *IEEE Transactions on Microwave Theory and Techniques*, vol. 66, no. 12, pp. 5300–5309, 2018.

[49] A. A. Muller, A. Moldoveanu, V. Asavei, E. Sanabria-Codesal, and J. F. Favennec, "Lossy coupling matrix filter synthesis based on hyperbolic reflections," in *2016 IEEE MTT-S International Microwave Symposium (IMS)*, 2016, pp. 1–4.

[50] S. B. Cohn, "Dissipation loss in multiple-coupled-resonator filters," *Proceedings of the IRE*, vol. 47, no. 8, pp. 1342–1348, 1959.

[51] H. Joshi, H. Sigmarsson, S. Moon, D. Peroulis, and W. Chappell, "High-Q fully reconfigurable tunable bandpass filters," *IEEE Transactions on Microwave Theory and Techniques*, vol. 57, no. 12, pp. 3525–3533, Dec. 2009. [Online]. Available: https://doi.org/10.1109/tmtt.2009.2034309

[52] T. H. Lee, *Planar Microwave Engineering: A Practical Guide to Theory, Measurement, and Circuits*. Cambridge University Press, 2004.

[53] S. Saeedi, "Frequency-agile microwave filters for radars with simultaneous transmission and reception," PhD Dissertation, University of Oklahoma, 2015.

[54] M. Thibodeau, "Theory, design, and fabrication of frequency agile filtennas," Master's Thesis, University of Oklahoma, 2020.

[55] D. Deslandes and Ke Wu, "Accurate modeling, wave mechanisms, and design considerations of a substrate integrated waveguide," *IEEE Transactions on Microwave Theory and Techniques*, vol. 54, no. 6, pp. 2516–2526, 2006.

[56] C. Deckert, "Electroless copper plating: a review." *Plating and Surface Finishing*, vol. 82, pp. 48–55, 1995.

[57] G. Matthaei, L. Young, and E. Jones, *Microwave Filters, Impedance-matching Networks, and Coupling Structures*, ser. Artech House microwave library. Artech House Books, 1980.

[58] M. Dishal, "Alignment and adjustment of synchronously tuned multiple-resonant-circuit filters," *Proceedings of the IRE*, vol. 39, no. 11, pp. 1448–1455, 1951.

[59] J. B. Ness, "A unified approach to the design, measurement, and tuning of coupled-resonator filters," *IEEE Transactions on Microwave Theory and Techniques*, vol. 46, no. 4, pp. 343–351, 1998.

[60] J.-S. Hong, *Microstrip Filters for RF/Microwave Applications*, 2nd ed. Wiley, Jan. 2011.

[61] N. Zahirovic and R. R. Mansour, "Automatic integrated filter tuning techniques," in *2012 IEEE/MTT-S International Microwave Symposium Digest*, 2012, pp. 1–3.

[62] Yu-Chen Wu, M. Abu Khater, and D. Peroulis, "Real-time temperature compensation control system for tunable cavity-based high-q filters," in *2015 IEEE MTT-S International Microwave Symposium*, 2015, pp. 1–4.

[63] H. H. Sigmarsson, A. Christianson, H. Joshi, Sungwook Moon, D. Peroulis, and W. J. Chappell, "In-situ control of tunable evanescent-mode cavity filters using differential mode monitoring," in *2009 IEEE MTT-S International Microwave Symposium Digest*, 2009, pp. 633–636.

[64] S. Saeedi, S. Atash-Bahar, J. Lee, and H. Sigmarsson, "Control system for piezoelectric-actuator-based tunable evanescent-mode cavity microwave filters," *IEEE Transactions on Components, Packaging and Manufacturing Technology*, vol. 8, no. 11, pp. 1979–1989, 2018.

[65] X. Liu, A. Fruehling, L. P. B. Katehi, W. J. Chappell, and D. Peroulis, "Capacitive monitoring of electrostatic mems tunable evanescent-mode cavity resonators," in *2011 6th European Microwave Integrated Circuit Conference*, 2011, pp. 466–469.

Appendix A

Fully Reconfigurable Filter Fabrication Process

The step-by-step fabrication process for the fully reconfigurable filter of Chapter 4 is presented in this appendix. This process requires multiple milling steps using the LPKF ProtoMat S103, LPKF ProtoLaser U4, and T-Tech Quick Circuit J5. The fabrication of the resonator and frequency-tunable filter is similar to this process only Step 4 is done with the LPKF ProtoMat S103 rather than the LPKF ProtoLaser U4.

There are 10 Gerber files generated that are needed to fabricate the design. The required Gerber files are as follows:

1. Plated_Drill_Via - plated vias to create the via cage of the device.

2. Laser_Milling_Via - 0.1 mm diameter laser drill holes to create the diaphragm air openings on the top metal layer 1 (M1).

3. Top_Metal_Layer - M1 pattern featuring the GCPW lines of the design.

4. Lineup_Via - eight unplated vias arrange in a square to be drilled using the LPKF Protomat S103 to allow for proper design alignment to the T-Tech Quick Circuit J5.

5. Ttech_Set_Pin_Holes - two 130 mil diameter unplated vias spaced with 4 in

pitch used to both align and anchor the board to the base of the T-Tech machine.

6. Center_Lineup_Via - unplated vias located at the center of the square of the Lineup_Via layer to be drilled using the T-Tech Quick Circuit J5 to align the design.

7. Ttech_Partial_Drill_Via - partially drilled vias for the capacitive tuning posts using the T-Tech Quick Circuit J5 to keep the M1 metal diaphragm intact.

8. Unplated_Drill_Via - unplated through vias for the iris tuning vias and any additional mounting holes.

9. Fiducial_Via - fiducial vias for alignment between all the LPKF milling or drilling steps.

10. Device_Outline - device outline for cutout of each device from the board.

11. Board_Outline - outline of the 6 in x 6 in board that contains the entire component array.

A.1 Detailed Fabrication Process

The fabrication process is broken down into the 8 steps as follows:

1. Board preparation

2. Plated via drilling

3. Board plating

4. Laser drilling and milling

5. Alignment holes and set pin hole drilling

6. T-Tech alignment

7. T-Tech partial via drilling

8. LPKF unplated via drilling and contour routing

A.1.1 Board preparation

The 6 in x 6 in board is aligned onto the LPKF S103 using Board_Outline and fiducial holes are drilled using Fiducial_Via to ensure proper registration is achieved throughout the fabrication process. For proper placement of the Fiducial_Via layer onto the board, the material locations settings in the LPKF software must be properly set. When the board is smaller than the LPKF machine bed, before the fiducial holes are drilled the material size and location must be changed using the following procedure:

1. Place the board onto the machine bed and tape the four corners with masking tape.

2. Mark the bottom left and top right corners with dark markings using a marker.

3. Under Processing $>$ Select head, change the head alignment to Camera.

4. In the LPKF CircuitPro PM software, navigate to Edit $>$ Material Settings $>$ Location.

5. Position the head of the camera to the bottom left corner dark marking and under Location press the Bottom Left Corner icon button.

6. Repeat for the top right corner marking.

After this board alignment step, the fiducial holes can be drilled.

A.1.2 Plated Via Drilling

Using Plated_Drill_Via, the via cage of the design and any other plated via holes are drilled using the LPKF S103. Carefully note whether this layer is being milled onto the bottom metal layer (M2) or onto the top metal layer (M1). For hard ceramic materials like TMM3, it is recommended to use a drill speed of 30,000 to 40,000 RPM. Sanding is done on the bottom side of the milled board to remove any metal burrs or residue that may detach during the plating process. If metal burrs remain, then the board can be flipped over onto its back, and the Plated_Drill_Via can be reassigned to the opposite side metal layer and redrilled (be sure to note the orientation and alignment is correct before redrilling).

A.1.3 Board Plating

The board is electroless plated and electroplated to metal plate the insides of all the plated vias. Titration should be done on the electroless plating tank before every plating process. All standard procedures of both the electroless plating and electroplating process should be readily available and followed.

A.1.4 Laser Drilling and Milling

The board is placed onto the LPKF U4 with M1 facing upward, and the design is aligned to the Board_Outline and Fiducial_Via layers from before. After metal plating, polishing and sanding of the metal surface around the fiducials holes may be necessary for proper camera detection by the LPKF U4. The air opening holes are drilled using Laser_Milling_Via and done for a recommended 5-10 iterations to

thoroughly laser drill through M1 and deep into the substrate. Top_Metal_Layer and Device_Outline are used to generate to the laser milling toolpath for the CPW trenches and patterned onto M1. Editing of the laser speed parameters may be necessary to thoroughly remove residual metal as well as manual cleaning using a precision blade.

A.1.5 Alignment Holes and Set Pin Hole Drilling

The camera fiducial alignment of the T-Tech Quick Circuit J5 is not operational at the time of this writing, so a workaround was developed using the set pins on the machining bed of the T-Tech J5. There are two set pins with a 125 mil diameter and a center-to-center distance of 4 in which are used to align the vacuum array backup material. These can be used as a reference to align the board between the T-Tech and the LPKF S103. These set pin holes and alignment holes are milled in this step using the LPKF S103 to created a common reference between the two machines.

The board is brought back to the LPKF S103 and Ttech_Set_Pin_Holes and Lineup_Via are drilled into the board as well as eight alignment holes as depicted in Fig. A.1 in dark orange. The LPKF S103 does NOT drill the center red hole of the alignment holes, which is reserved for the next T-Tech alignment step.

A.1.6 T-Tech Alignment

The T-Tech J5 is designed so that it cannot drill into the metal body of the machine. It checks for this by doing an electrical continuity test between the drill bit and the milling foot. This means that the T-Tech cannot drill into the board if it is electrically connected to the body of the machine. To prevent this, masking tape must be placed over the entire machine bed and over the set pins to prevent this

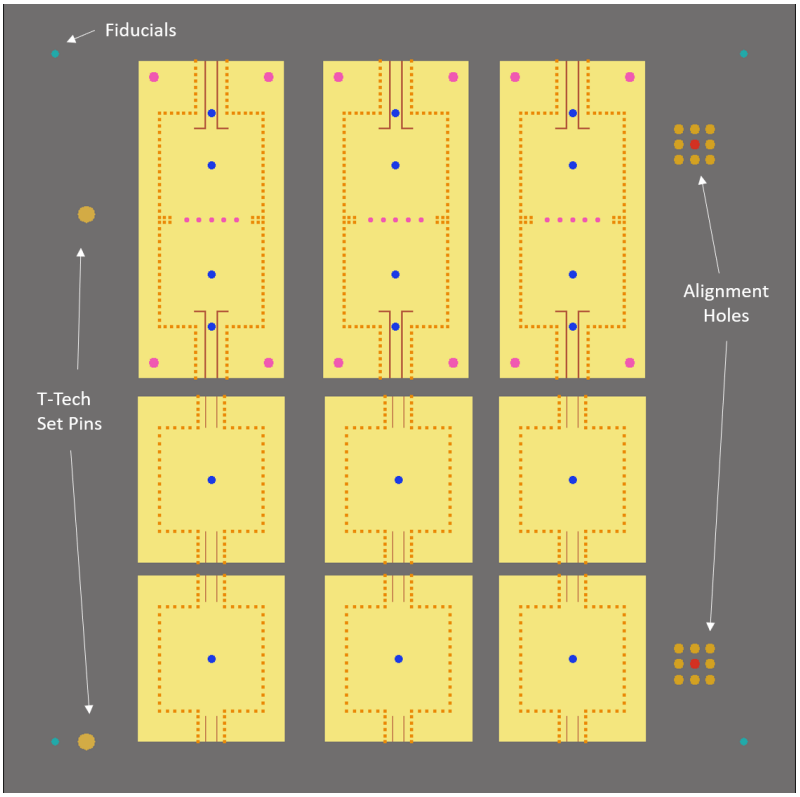

Figure A.1: Example of board layout with an array of resonators and fully reconfigurable filter designs with labels pointing to the fiducial vias, set pin holes, and alignment holes

electrical connection. If the drill bit stops at the start of the process before drilling into the board, this means the T-Tech has detected an electrical connection and more tape must be placed to isolate the board somewhere.

After prepping the board and machine bed, the board is placed onto the build surface with M2 facing upward and with the set pin holes pushed firmly around the set pins of the machine bed. All the Gerber files are imported into the T-Tech Quick Circuit program and aligned so that Ttech_Set_Pin_Holes match with the location of the set pin holes in the program. To check for any misalignment, the Center_Lineup_Via is drilled into the substrate and checked to see if it is correctly centered within the squares of the drilled holes of Lineup_Via. If it is not correctly

centered, the entire design is shifted in the T-Tech Quick Circuit program, and Center_Lineup_Via is redrilled until it is correctly centered.

A.1.7 T-Tech Partial Via Drilling

This is the step that Ttech_Partial_Drill_Via is partially drilled into the substrate to create the top metal diaphragm. It is best to drill each of these holes one-by-one and to place the T-Tech depth reference test as close to the location of the location of the drill hole as possible. Before each machine pass of the T-Tech J5, if the drill bit is not already defined a prompt will appear asking for different drill parameters. The drill parameters are set to a speed of 50,000 RPM, 4 pecks, and a drill depth about the thickness of the substrate. After drilling each hole, check inside each hole with a light to look for reflections from M1. If there is not a light, then there is still substrate that needs to be removed and another pass should be done over the same via with a deeper drill depth. It has been found that iterative steps of 2 mil allow for best results with gradual removal of the substrate without puncturing the metal diaphragm.

A.1.8 LPKF Unplated Via Drilling and Contour Routing

The board is now taken back to the LPKF S103 to do drilling of any remaining unplated via holes for the design with Unplated_Drill_Via. For the case of the fully reconfigurable design, this included the five iris tuning vias and four mounting holes at the corners of each device. The device is then contour routed using Device_Outline as the cutout layer. When contour routing a hard material such as TMM3, it is recommended to only route half or a third of the material thickness on each pass.